University of Sussex

Measuring Muon Neutrino Disappearance With The NOvA Experiment

Luke Vinton

Submitted for the degree of Doctor of Philosophy

University of Sussex

21st March 2017

Chapter 1

Introduction

The neutrino was discovered a little over 60 years ago and during the last two decades the ability of neutrinos to change flavour in flight has been established beyond doubt. The Standard Model of particle physics defines neutrinos to be massless. However, neutrino oscillations in vacuum requires that at least one of the neutrinos has a mass. This means that the current the model is incomplete and neutrino oscillations are beyond the Standard Model.

Neutrino oscillation experiments such as NOvA aim to measure the probability of a neutrino oscillating from one flavour to another and the rate of the oscillation. Such measurements probe the neutrino mixing angles and the difference between the squared neutrino masses.

the neutrino mixing parameters and the difference between

Chapter 2

Neutrino Physics

Let us start in 1914, when Chadwick presented experimental evidence [1] that the energy spectrum of electrons emitted in β decay was continuous instead of being discrete as expected. This meant either β decay was not a two-body process or conservation of energy was violated. The solution arrived in 1930, when neutrinos were postulated by Wolfgang Pauli [2] as a "desperate remedy" to the apparent non-conservation of energy in nuclear β decay. He suggested that an additional neutral and extremely light particle was produced in β decay which carried away the undetected energy. Pauli referred to this aditional particle as a "neutron". In 1934 Fermi [3] formulated a theory of β decay and re-named the additional particle as the "neutrino".

In 1956, Cowan and Reines [4] incredibly overcame the hurdle of actually detecting neutrinos [1] and provided the first direct evidence for their existence. The pair setup an experiment to measure the flux of neutrinos emitted from a nuclear reactor. The neutrinos from the reactor were produced via β decay and were detected via inverse β decay ($p+\bar{\nu} \rightarrow n+e^+$). If a neutrino interacted within the detector it would produce a characteristic signal of a pair of photons from electron-positron annihilation and a delayed photon from neutron capture.

At first it was thought that neutrinos only come in one flavour. This view changed with the subsequent discovery of muon and tau neutrinos. Muon and tau neutrinos were discovered several decades apart. In 1962 neutrinos which produce muons but not electrons when interacting with matter were observed [5]. In the paper it was suggested that neutrinos produced in association with a muon are muon neutrinos which are distinct from

[1] They expressed the double edged sword of the validity of Pauli's neutrino proposal and the difficulty of neutrino detection as "the very characteristic of the particle which makes the proposal plausible - it's ability to carry off energy and momemtum without detection".

the electron neutrinos previously observed in β decay. In 1989, The ALEPH collaboration published measurements of the mass and width of the Z boson [6]. Consequently they were able to constrain the number of active light neutrinos to be three at 98% confidence level. Final results from the ALEPH experiment provided conclusive proof that the number of light active neutrinos is indeed three [7]. In 2000, the DONUT experiment reported an observation of four tau neutrino neutrinos with a background estimation of 0.34 events [8]. This third neutrino completed the set of the three standard model neutrinos associated with the three charged leptons.

The first hints of neutrino oscillations came from experiments measuring the flux of solar neutrinos. The Fusion reactions by which energy is produced in the sun are modelled by the Standard Solar Model. The model predicts three major neutrino emissions: pp neutrinos ($p + p \rightarrow d + e^+ + \nu_e$, $E_{max.} = 420$ keV), ^{7}Be neutrinos ($^7\text{Be} + e^- \rightarrow ^7\text{Li} + \nu_e$, $E_{max.} = 860$ keV) and ^{8}B neutrinos ($^8\text{B}+e^- \rightarrow ^8\text{Be}+e^+ + \nu_e$, $E_{max.} = 14$ MeV). [9] In 1968 Ray Davis et. al. published the "Search For Neutrinos From the Sun" paper [10]. In the same year Bahcall et. al. published a prediction for the solar neutrino flux experienced by Ray Davis's experiment based on the standard solar model [11]. Davis used the interaction $Cl^{37} + \nu \rightarrow e^- + Ar^{37}$ to measure the flux of ^{8}B and ^{7}Be solar electron neutrinos. The measured rate of neutrinos was found to be only one third of the rate predicted by Bahcall. At the time of publication this discrepency was generally attributed to errors in either the measurement technique or the standard solar model at high neutrino energies and became known as the "solar neutrino puzzle". In 1989, the Kamiokande-II experiment confirmed the deficit of ^{8}B solar electron neutrinos relative to the standard solar model [12]. In 1991 and 1992, the deficit was further confirmed by two experiments, SAGE [13] and GALLEX [9], which both measured the rate of the less energetic pp solar neutrinos. These experiments showed that the flux deficit occured for low energy pp neutrinos as well as the higher energy ^{8}B and ^{7}Be neutrinos measured previously.

Either the standard solar model was incorrect or electron neutrinos produced in the Sun do not all survive the journey to the Earth. Neutrino oscillation due to massive neutrinos became accepted as a realistic possibility. Previously, in the years 1962-1968, Pontecorvo, Maki, Nakagawa, and Sakata had formulated a theory including electron and muon neutrinos which were able to change from one to the other [14, 15, 16].

In 1998, Super Kamiokande reported evidence for the oscillation of atmospheric neutrinos [17]. They measured the rate of muon and electron neutrinos originating from collisions of cosmic rays with nuclei in the upper atmosphere. The detector allowed the reconstruc-

tion of the direction of the incoming neutrino, this revealed the baseline from production to detection and whether the neutrino travelled through the Earth. Electron and muon neutrinos are produced in the upper atmosphere in the ratio 1:2 (electron:muon). The assymetry of upward and downward going events was measured for both electron and muon neutrinos. The electron neutrino assymetry was consistent with zero but a momentum dependant assymetry was observed for muon neutrinos at more than 6 standard deviations. The data was concluded to show evidence for neutrino oscillations.

In 2005, SNO published measurements of the flux of solar ^{8}B neutrinos [18]. They measured the rate of charged current electron neutrino events and were also able to measure the rate of neutral current events due to all three active neutrinos. The measured neutral current flux was consistent with the flux expected from the standard solar model but the measured flux of electron neutrinos was significantly lower than the measured total flux of active neutrinos. Neutrino oscillations were reconfirmed solving the solar neutrino puzzle.

Since the confirmation of neutrino oscillations the spotlight has moved on to the unknown neutrino properties, such as: the parameters which govern oscillations, the nature of neutrinos (whether they are Dirac or Majorana particles), strength of interaction with matter, the mass, origin of mass and the number of neutrinos. Experimental and theoretical advances have made progress on the above questions during the last ≈ 60 years [19] and the observation of neutrino oscillations has opened new fundamental questions regarding the origin of fermion masses and the relationship between quarks and leptons [20].

2.0.1 Recent results

The Kamioka Liquid Scintillator Anti-Neutrino Detectro (KamLAND) was designed as search for the oscillation of electron antineutrinos emitted from nuclear power stations. Typical baseline of 180 km intended to adress the oscillation solution to the "solar neutrino problem". Use inverse β -decay to detect electron antineutrinos. 1 kton ultrapure LS detector. 2003, first evidence of electron antineutrino disappearance. Ratio of observed inverse $\beta-$ decay events to expected events without electron neutrino disappearance was $0.611 \pm 0.085(\text{stat.}) \pm 0.041(\text{syst.})$. Fewer events than expected at the 99.95% confidence level. [21] 2005, direct evidence for neutrino oscillations via observation of distortion in rector electron antineutrino energy spectrum. [22] More rectently in 2008. Exposure of 2.44×10^{32}proton yr Measured values: $\Delta m^2_{21} = 7.58^{+0.14}_{-0.13}(\text{stat.})^{+0.10}_{-0.06}(\text{syst.})$ and $\tan^2\theta_{12} = 0.56^{+0.10}_{-0.07}(\text{stat.})^{+0.10}_{-0.06}(\text{syst.})$. [23]

The Sudbury Neutrino Observatory (SNO) was created to measure the flux of neutrinos

produced in the Sun, by ^{8}B decays in particular. 1 kton detector. Imaging Cherenkov detector using heavy water(^2H_2O. 1.783 km below sea level and an overburden of 5.890 km water equivalent. SNO detected neutrinos via three processes: elastic scattering, charged current and neutral current interactions. Measuring the rates of these three processes gave insight on the overall flux of neutrinos from the sun and also the flux of electron neutrinos that reach the detector. By comparing these fluxes SNO was able to test the neutrino oscillation hypothesis. [24] In 2013. Combined result of SNO and all other solar and reactor neutrino experiments gave $\Delta m^2_{21} = (7.46^{+0.20}_{-0.19}) \times 10^{-5}$ eV^2, $\tan^2\theta_{12} = 0.443^{+0.030}_{-0.025}$ and $\sin^2\theta_{13} = (2.49^{+0.20}_{-0.32}) \times 10^{-2}$. [25]

The Super Kamiokande (SK) is an imaging water Cherenkov detector designed to detect neutrinos produced by ^{8}B decays in the Sun. 2011 paper. Solar neutrino experiment measuring flux of electron neutrinos from the sun from the stellar production of nuetrinos from the ^{8}B reaction chain. Via neutrino electron scattering. Located 1 km underground. 50 ktons of ultrapure water. signals read out ny photomulilyer tubes. Three flavour fit produces $\sin^2\theta_{12} = 0.30^{+0.02}_{-0.01}$ and $\Delta m^2_{21} = 6.2^{+1.1}_{-1.9} \times 10^{-5}$ eV^2. In combination with other solar experiments and KamLand found $\sin^2\theta_{13} = 0.025^{+0.018}_{-0.016}$. [26] [27]

Measurement of electron antineutrino disappearance with the Daya Bay experiment. Non zero value of θ_{13} measured with precision by Daya Bay, which measured $\sin^2 2\theta_{13} = 0.084 \pm 0.005$. Total exposure of 6.9×10^5 GW$_{th}$ ton days. Opening the door to the measurement of electron neutrino apearance in a muon neutrino beam and hence measurements of the mass hierarchy and the cp violating phase δ_{CP}. Fully constructed experiment consists of 8 detectors and 6 nuclear reactor cores. [28] Large value of $\sin^2\theta_{13}$ measured by Daya Bay [29].

RENO is a reactor antineutrino disappearance experiment. Reactor electron antineutrinos are detected via inverse β decay. Conincidence of prompt positron signal and a delayed photon signal from neutron capture is the signature for inverse β decay. Two identical detectors located 294 m and 1383 m from the centre of six reactor cores. Each detector consists of a main inner detector and an outer veto detector.$\sin^2 2\theta_{13} = 0.082 \pm 0.009(\text{stat.}) \pm 0.006(\text{syst.})$. [30] [31]

The Double Chooz experiment measures reactor antineutrino disappearance. Far detector is located at an average distance of 1050 m from the two reactor cores at the Chooz nuclear power plant. Measured: $\sin^2 2\theta_{13} = 0.090^{+0.032}_{-0.029}$. [32]

The Main Injector Neutrino Oscillation Search (MINOS) experiment was designed to measure the flavour composition of a muon neutrino beam at two locations using a near

and far detector located 1 km and 735 km from the target respectively. In 2006 the first muon neutrino disappearance results observed 215 events compared to an expectation of 336 ± 14 events and were consistent with disappearance via oscillations. [33] Most recently, in 2015 a joint analysis of accelerator and atmospheric neutrinos combining muon neutrino disappearance, electron neutrino apearance further improved the precision of parameter measurements with the results $|\Delta m^2_{32} = |2.28 - 2.46| \times 10^{-3}$ eV^2 [34]

2.0.2 The Weak Force

Neutrinos interact with matter through the weak force in one of three flavour eigenstates (electron, muon or tau). The weak force is mediated by the electrically charged W$^{\pm}$ and electrically neutral Z bosons.

Include feynam diagrams of the neutrino interactions.

A neutrino interacting with matter through the W boson will produce a charged lepton corresponding to the weak flavour of the incoming neutrino. This process can happen in reverse, with a charged lepton producing a neutrino with the same flavour and a W boson. Such processes involving a W boson are known as charged current interactions (CC interactions).

2.1 Neutrino Eigenstates

As current understanding has it, neutrinos come in three eigenstates of the weak force (electron, muon and tau) and three mass eigenstates (m_1, m_2 or m_3).

Neutrinos interact with matter through the weak force in eigenstates of lepton flavour (ν_e, ν_μ and ν_τ). They propagate through vacuum in eigenstates of mass (ν_1, ν_2 and ν_3). The eigenstates of mass and flavour are not equivalent, instead the flavour states are a superposition of the mass states. A neutrino of definite weak flavour α can be written as a linear combination of the mass states as follows,

$$|\nu_\alpha >= \sum_{i=1}^{3} U^*_{\alpha i} |\nu_i >, \tag{2.1}$$

where $U^*_{\alpha i}$ is the element of the unitary PMNS (Pontecorvo, Maki, Nakagawa, and Sakata) matrix describing the coupling strength between the mass state i and the flavour state α.

The standard parametrisation of the PMNS matrix is in terms of a phase δ and three mixing angles, θ_{12}, θ_{13} and θ_{23}. The PMNS matrix is conventionally written as:

$$U = \begin{pmatrix} U_{e1} & U_{e2} & U_{e3} \\ U_{\mu 1} & U_{\mu 2} & U_{\mu 3} \\ U_{\tau 1} & U_{\tau 2} & U_{\tau 3} \end{pmatrix} \tag{2.2}$$

$$= \begin{pmatrix} c_{13}c_{12} & c_{13}s_{12} & s_{13}e^{-i\delta} \\ -c_{23}s_{12} - s_{13}s_{23}c_{12}e^{i\delta} & c_{23}c_{12} - s_{13}s_{23}s_{12}e^{i\delta} & c_{13}s_{23} \\ s_{23}s_{12} - s_{13}c_{23}c_{12}e^{i\delta} & -s_{23}c_{12} - s_{13}c_{23}s_{12}e^{i\delta} & c_{13}c_{23} \end{pmatrix} \tag{2.3}$$

$$= \begin{pmatrix} 1 & 0 & 0 \\ 0 & c_{23} & s_{23} \\ 0 & -s_{23} & c_{23} \end{pmatrix} \begin{pmatrix} c_{13} & 0 & s_{13}e^{-i\delta} \\ 0 & 1 & 0 \\ -s_{13}e^{i\delta} & 0 & c_{13} \end{pmatrix} \begin{pmatrix} c_{12} & s_{12} & 0 \\ -s_{12} & c_{12} & 0 \\ 0 & 0 & 1 \end{pmatrix} \tag{2.4}$$

where $s_{ij} \equiv \sin\theta_{ij}$, $c_{ij} \equiv \cos\theta_{ij}$ and δ is the CP violating phase. A non-zero value of δ would indicate charge-parity violation.

2.2 Neutrino Oscillation Probability in Vacuum

The following derivation of the neutrino oscillation probability follows [19] and [35].

A neutrino is produced via a weak interaction as a flavour eigenstate. At time $t = 0$ the flavour state, α, can be written as $|\nu_\alpha\,(t=0)>$ and is the sum of the mass states $|\nu_i>$:

$$|\nu_\alpha\,(t=0)>= \sum_{i=1}^{3} U^*_{\alpha i}|\nu_i> . \tag{2.5}$$

As the neutrino propagates the mass states evolve. At time t we have:

$$|\nu_\alpha\,(t)>= \sum_{i=1}^{3} U^*_{\alpha i} e^{-ip_i.x}|\nu_i>, \tag{2.6}$$

where p_i is the four-momentum and x the four-position of mass state ν_i.

At time t the neutrino weakly interacts with matter in flavour state β:

$$\begin{aligned} <\nu_\beta|\nu_\alpha> &= \sum_{j=1}^{3}\sum_{i=1}^{3} U_{\beta j}U^*_{\alpha i}e^{-ip_i.x} <\nu_j|\nu_i> \\ &= \sum_{j=1}^{3} U_{\beta j}U^*_{\alpha j}e^{-ip_j.x}. \end{aligned} \tag{2.7}$$

Assuming all mass states have the same three-momentum $\mathbf{p}$,

$$\begin{aligned} p_j.x &= E_j t - \mathbf{p}\cdot\mathbf{x} \\ &= t\sqrt{|\mathbf{p}|^2 + m_j^2} - \mathbf{p}\cdot\mathbf{x} \end{aligned} \tag{2.8}$$

Since neutrinos are extremely light ($m_\nu < 2\ eV$ [19]) and, in the case of accelerator experiments, travel at close to the speed of light we can make the approximations, $m_j << E_j$, $t = L$ and $\mathbf{p}\cdot\mathbf{x} = |\mathbf{p}|L$. Using a binomial expansion we find,

$$p_j \cdot x = |\mathbf{p}|L\left(1 + \frac{m_i^2}{2|\mathbf{p}|^2}\right) - |\mathbf{p}|L = \frac{m_j L}{2E} \tag{2.9}$$

Combining Equations 2.7 and 2.9 we get $< \nu_\beta|\nu_\alpha >= \sum_{j=1}^{3} U_{\beta j}U^*_{\alpha j}e^{-i\frac{m_j L}{2E}}$.

The probability of observing the neutrino in flavour state β after travelling distance L and given initial flavour state α is given by:

$$\begin{aligned} P_{\alpha\to\beta} &= |< \nu_\beta(t)|\nu_\alpha(t) >|^2 \\ &= \left(\sum_{j=1}^{3} U_{\beta j}U^*_{\alpha j}e^{-i\frac{m_j L}{2E}}\right)\left(\sum_{i=1}^{3} U^*_{\beta i}U_{\alpha i}e^{i\frac{m_j L}{2E}}\right). \end{aligned} \tag{2.10}$$

Finally, we find:

$$\begin{aligned} P_{\alpha\to\beta} = \delta_{\alpha\beta} &- 4\sum_{i>j}\Re[U^*_{\alpha i}U_{\alpha j}U_{\beta i}U^*_{\beta j}]\sin^2\left(\frac{\Delta m_{ij}^2}{4E}L\right) \\ &+ 2\sum_{i>j}\Im[U^*_{\alpha i}U_{\alpha j}U_{\beta i}U^*_{\beta j}]\sin^2\left(\frac{\Delta m_{ij}^2}{2E}L\right), \end{aligned} \tag{2.11}$$

where $\Delta m_{ij}^2 \equiv m_i^2 - m_j^2$ and $\delta_{\alpha\beta}$ is the Kronecker delta. The equation shows that the neutrino oscillation probability depends on the parameters of the PMNS matrix and the value of the two sinusoidal arguments. The probability depends on the mass splittings Δm_{12}^2, Δm_{13}^2, Δm_{23}^2, and alters with the length of the baseline, L, and the energy of the neutrino beam, E.

2.3 Neutrino Oscillation Paremeter Measurements

The experimentally measured values of the neutrino oscillation parameters are given in Table 2.1. The measurements of the oscillation parameters have been made using reactor, solar, accelerator and atmospheric neutrino experiments.

Parameter	Average of measurements
$\sin^2\theta_{12}$	0.304 ± 0.014
Δm^2_{21} [10^{-5} eV^2]	7.53 ± 0.18
$\sin^2\theta_{23}$	0.51 ± 0.05 (0.50 ± 0.05)
Δm^2_{32} [10^{-3} eV^2]	2.44 ± 0.06 (-2.51 ± 0.06)
$\sin^2\theta_{13}$ [10^{-2}]	2.19 ± 0.12

Table 2.1: The average value of measurements and 1σ error of the neutrino oscillation parameters from [19]. Measurements that differ under the assumption of inverted ordering (rather than normal ordering) are provided within parenthesis.

The two mass differences and three mixing angles have all been measured. The sign of the mass difference has been determined for Δm^2_{12} (ν_1 is less massive than ν_2) but not for Δm^2_{23}. This means that it is not known whether ν_3 is more or less massive than the two other mass states, the former and later cases are known as Normal Ordering or Inverted Ordering respectively. A schematic showing the Normal and Inverted Ordering is shown in Figure

Tentative measurements of the CP violating phase δ_{CP} have been made [36] but the value remains relatively unknown.

Current measurements suggest that $\sin^2\theta_{23} = 0.5$ which would mean $\cos^2\theta_{23} = 0.5$. In this case, $U_{\mu 2} = U_{\tau 3} = \frac{1}{2}c_{13}$ (see Equation 2.4). These two PMNS matrix elements define the mixing of ν_μ and ν_τ with ν_3. Therefore, if $\sin^2\theta_{23} = 0.5$ then the third mass state is composed of equal parts ν_μ and ν_τ, this is known as maximal mixing. If nature has chosen non-maximal mixing then discovering the octant (whether $\sin^2\theta_{23}$ is less or more than 0.5) will determine whether the third mass state is composed of more ν_μ or more ν_τ.

2.4 Two-Flavour Approximation

In many experimental cases the neutrino oscillation probability can be approximated as the result of two-flavour mixing. This two flavour oscillation probability and the necessary approximation will be outlined in this section.

For long baseline neutrino oscillation experiments it is useful to write the phase $\frac{\Delta m^2_{ij}}{4E}L$ in units of the same scale as the experiment. This is done using units of eV^2 for Δm^2_i, GeV for E and km for L. Restoring factors of $\hbar$ and c and applying the appropriate unit

conversions we find:

$$\frac{\Delta m_{ij}^2 c^3}{4E\hbar} L \approx 1.27 \frac{\Delta m_{ij}^2 [\mathrm{eV}^2]}{E[\mathrm{GeV}]} L[\mathrm{km}]. \tag{2.12}$$

Let us use the oscillation channel relevant to this thesis as the example. In the three flavour case (Equation 2.11), the muon neutrino survival probability is:

$$P_{\mu\to\mu} = 1 - 4\sum_{i>j} |U_{\mu i}|^2 |U_{\mu j}|^2 \sin^2\left(\frac{\Delta m_{ij}^2}{4E} L\right), \tag{2.13}$$

where the imaginary component of Equation 2.11 is zero because in this case $\Im[U_{\mu i}^* U_{\mu i}] = 0$.

The elements of the PMNS matrix, $U_{\mu i}$, can be simplified considering the current measured values. Table 2.1 shows that the value of $\sin^2\theta_{13}$ is very small relative to the two other mixing parameters. Using the approximations $\sin\theta_{13} \approx 0$ and $\cos\theta_{13} \approx 1$ the relevant PMNS elements (see Equation 2.4 can be approximated as:

$$\begin{aligned} |U_{\mu 1}|^2 &\approx s_{12}^2 c_{23}^2 \\ |U_{\mu 2}|^2 &\approx c_{12}^2 c_{23}^2 \\ |U_{\mu 3}|^2 &\approx s_{23}^2 \end{aligned} \tag{2.14}$$

Experimental results have shown that the mass splitting Δm_{12}^2 is very small relative to Δm_{13}^2 and Δm_{23}^2 (see Table 2.1) [19], which allows the approximation: $\Delta m_{13}^2 \simeq \Delta m_{23}^2$. For long baseline neutrino oscillation experiments the oscillations associated with the atmospheric and solar mass splittings can be approximated to be de-coupled. This is because the atmospheric mass splitting is ∼30 times larger than the solar mass splitting. As an example, let us take the NOvA experiment with $L = 810$ km and $E \sim 2$ GeV. For the NOvA experiment the we have:

$$\sin^2\left(\frac{1.27\Delta m_{12}^2}{E} L\right) = \sin^2\left(\frac{1.27 \times 7.53 \times 10^{-5}}{2} \times 810\right) \approx \sin^2 0.04 \approx 0. \tag{2.15}$$

With the above simplifications, the muon neutrino survival probability can be expressed as:

$$\begin{aligned} P_{\mu\to\mu} &\simeq 1 - 4 s_{23}^2 c_{23}^2 (s_{12}^2 + c_{12}^2) \sin^2\left(\frac{1.27\Delta m_{atm.}^2}{E} L\right) \\ &\simeq 1 - \sin^2 2\theta_{23} \sin^2\left(\frac{1.27\Delta m_{atm.}^2}{E} L\right), \end{aligned} \tag{2.16}$$

where $\Delta m_{atm.}^2 \equiv \Delta m_{32}^2 \simeq \Delta m_{13}^2$. From this equation it can be seen that the disappearance probability has an oscillatory form. The overall magnitude of the oscillation is governed by $\sin^2 2\theta_{23}$ and the period of the oscillation is defined by $\frac{\Delta m_{atm.}^2 L}{E}$.

2.5 Matter Effects

Neutrinos propagating through matter experience the weak force through NC interactions and coherent forward scattering. Ordinary matter is composed, in part, of electrons but not muons or taus. For this reason coherent forward scattering (shown in Figure 2.1) is only experienced by electron neutrinos. In addition, NC interactions with matter are flavour independant and so do not affect neutrino oscillations. This additional scattering amplitude causes oscillations involving ν_e or $\bar{\nu}_e$ to have different probabilities relative to oscillation in vacuum.

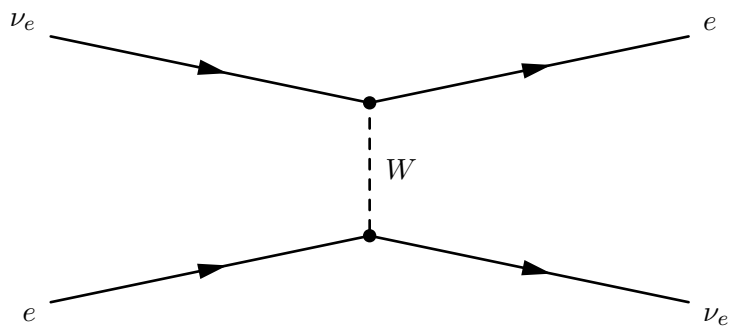

Figure 2.1: Feynman diagram of coherent forward scattering of ν_e on e.

The evolution of the neutrino flavour states is given by

$$i\frac{d}{dx}\begin{pmatrix}\nu_e\\ \nu_\mu\\ \nu_\tau\end{pmatrix} = H\begin{pmatrix}\nu_e\\ \nu_\mu\\ \nu_\tau\end{pmatrix}, \tag{2.17}$$

where H is the Hamiltonian. In matter H is given by

$$H = U\begin{pmatrix}\frac{m_1^2}{2E} & 0 & 0\\ 0 & \frac{m_2^2}{2E} & 0\\ 0 & 0 & \frac{m_3^2}{2E}\end{pmatrix}U^\dagger + \begin{pmatrix}\sqrt{2}G_F N_e & 0 & 0\\ 0 & 0 & 0\\ 0 & 0 & 0\end{pmatrix}, \tag{2.18}$$

where G_F is the Fermi constant and N_e is the electron number density of the medium.

Matter effects modify the terms $\sin(\Delta_{31})$ and $\sin(\Delta_{21})$ (where $\Delta_{ij} \equiv \frac{\Delta m_{ij}^2}{4E}L$)in Equation 2.11 by substituting:

$$\sin(\Delta_{ij}) \rightarrow \frac{\Delta_{ij}}{\Delta_{ij} \mp aL}\sin(\Delta_{ij} \mp aL), \tag{2.19}$$

where $a = \frac{G_F \rho_e}{\sqrt{2}}$, the top sign refers to neutrinos and the bottom sign to antineutrinos. [37]

For the Normal Ordering, matter effects enhance the apearance probability $\nu_\mu \to \nu_e$ but suppress the apearance probability $\bar{\nu}_\mu \to \bar{\nu}_e$. Conversely, for the Inverted Ordering matter effects suppress the ν_e apearance probability and enhance the $\bar{\nu}_e$ probability.

Matter effects have the opposite consequence for neutrinos and antineutrinos and so can be confused with the effect of true CP violation. Figure 2.2 illustrates the ambiguity between CP and matter effects when measuring the neutrino and antineutrino apearance. The figure shows regions of bi-probability where it is possible to disentangle the contributions of matter effects and CP violation. In particular, for the inverted hierarchy and $\delta_{CP} = 3\pi/2$ (the starred point) NOvA would be able to measure the mass ordering to be Normal with some confidence. This point would correspond to measured probabilities of $P(\bar{\nu}_e) = 0.025$ and $P(\nu_e) = 0.06$. Conversely, if NOvA measures $P(\bar{\nu}_e) = 0.04$ and $P(\nu_e) = 0.04$ then it will not be possible to distinguish between two possible scenarios: either the ordering is normal and $\delta_{CP} \approx \pi$ 2 or the ordering is inverted and $\delta_{CP} \approx 3\pi$ 2. The two elipses shown are for fixed values of $\sin^2(2\theta_{13})$, $\sin^2(2\theta_{23})$ and Δm^2_{32}. The effect of increasing (decreasing) θ_{23} is to increase (decrease) both apearance probabilities and make the ellipses less (more) ambiguous.

2.6 Latest Results

About 5 pages

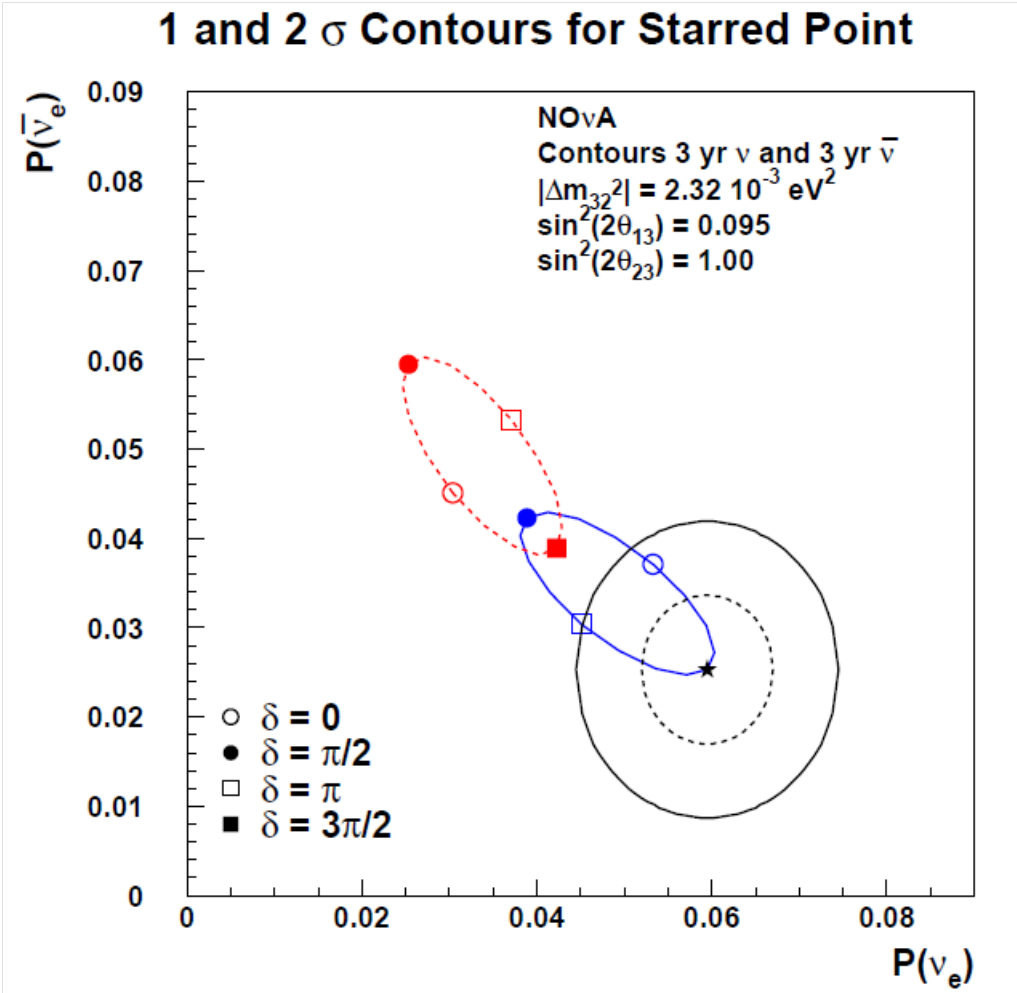

Figure 2.2: Bi-probability plot of ν_e apearance for the NOvA experiment. The solid blue and dotted red elipses show the possible probability measurements for the Normal and Inverted Ordering respectively. The effect of altering δ_{CP} is to trace out the ellipse. Selected values of δ_{CP} are shown by the square and circle markers. Taken from [38].

Chapter 3

The NOvA Experiment

The NuMI Off-axis ν_e Appearance (NOvA) experiment is designed to make precise measurements of muon neutrino disappearance and electron neutrino appearance in a muon neutrino beam. The experiment consists of two functionally equivalent detectors which measure the neutrino energy and flavour composition of the Neutrinos at the Main Injector (NuMI) beam. The detectors are constructed from PVC tubes filled with liquid scintillator and are highly granular to distinguish neutrino induced signals and background. The 300 ton near detector is located on site at Fermilab 1.015 km from the NuMI target. The 14 kiloton far detector is located at a site near Ash River, Minnesota and is 810 km from the NuMI target. The baseline and mean neutrino energy are chosen such that the far detector sees the first oscillation maximum driven by Δm^2_{32}. Both detectors are placed off-axis from the centre of the NuMI beam to enhance the sensitivity to electron neutrino appearance and muon neutrino disappearance.

The original design of the NOvA experiment is laid out in the technical design report (TDR) [37] and the constructed experiment design differs only slightly. The details of the constructed experiment, including the neutrino beam source and the two detectors, are discussed in the following chapter.

3.1 The NuMI Beam

The NOvA experiment's neutrino source is the Neutrinos at the Main Injector (NuMI) beam at Fermilab. The following section briefly describes the process by which the NuMI beam is created. More details are available in Ref [39].

The NuMI beam-line extracts batches of approximately 4.8×10^{13} 120 GeV protons from the Main injector and directs them onto a 0.95 m long graphite target. Each extrac-

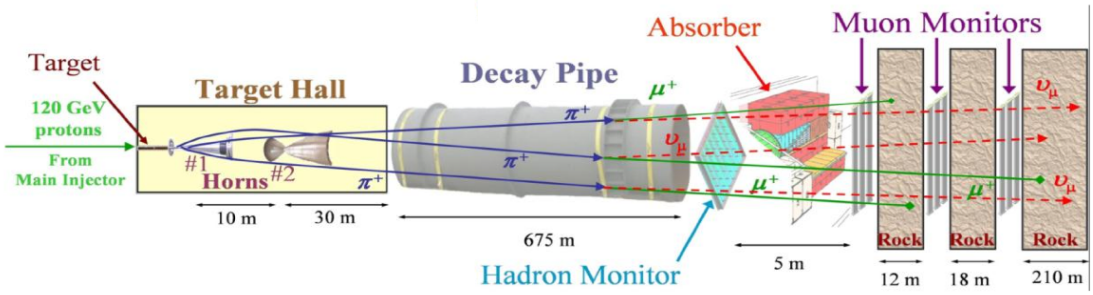

Figure 3.1: A diagram showing the layout of the NuMI beam. [39]

tion of protons is known as a beam spill. There is typically an interval of 1.33 s between beam spills.

An instructive diagram of the NuMI beam facility is presented in Figure 3.1, which shows the beam components including the Target Hall, Decay Pipe, Hadron Monitor, Absorber and Muon Monitors. Within the target hall, collisions between the accelerated protons and the carbon atoms of the target produce a plethora of secondary particles (mostly pions and kaons). The charged mesons of one sign (or the other) are focused into a beam by two magnetic focussing horns. The resulting beam of charged mesons then enters the 675 m long He filled Decay Pipe. Along this length the mesons decay predominantly to charged leptons and neutrinos. The decay pipe is followed by the Hadron Monitor, the Absorber, Muon Monitors and about 240 m of rock. The remaining muons are absorbed by the rock leaving a beam of neutrinos. After the rock the beam arrives at the NOvA near detector before continuing through the Earth's crust for 810 km where it reaches the NOvA far detector.

3.1.1 Focussing Horns

Two magnetic horns are used to focus the mesons created by collisions of protons with the NuMI target into a beam. Figure 3.2 shows the NuMI target, Horn 1, Horn 2 and example meson trajectories. The design of the focussing horns allows three potential seperations between Horn 1 and Horn 2 corresponding to a low, medium and high energy beam. In the medium energy tune the Target is placed 1.3 m upstream from the opening of Horn 1 while Horn 2 is placed 23 m downstream relative to the front face of Horn 1. The NuMI horns are setup in the medium energy configuration for the NOvA era.

The horns act as a lens where the focal length is proportional to the momentum of the mesons. Changing the current direction within the focussing horns, choosing either forward or reverse horn current, changes the direction of the magnetic field and therefore

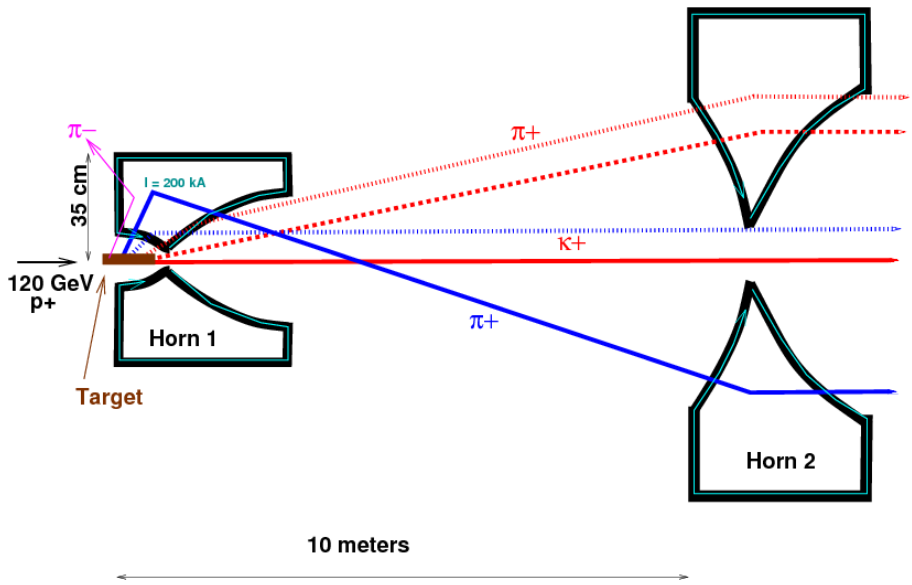

Figure 3.2: A diagram of the magnetic focussing horns operating in forward horn current mode. Positively charged mesons arriving from different directions are focussed by the combination of the two horns. The trajectory of positively charged mesons that are over or under focussed by Horn 1 can be corrected by Horn 2. Diagram taken from [39].

the sign of the mesons that are focussed. Operating the horns with forward or reverse horn current selects positively or negatively charged mesons respectively, leading to a predominantly neutrino or antineutrino beam respectively.

3.1.2 Off-axis Experiment Design

The NOvA detectors are both placed 14 mrads off the axis of the NuMI beam. The dominant decay process used to produce a neutrino beam is a two-body decay, where a pion (or kaon) decays to a neutrino and a muon. The two body decay occurs isotropically in the parent particle's rest frame. In the lab frame the parent particle is not at rest when decaying, for pion and kaon decay this boosts the neutrinos in the direction of the parent particle. For small angles, the flux per decay (Φ) and energy (E_ν) of neutrinos produced by pion decay ($\pi \to \nu_\mu + \mu$) are given by

$$\Phi = \left(\frac{2\gamma}{1+\gamma^2\theta^2}\right)^2 \frac{A}{4\pi z^2}, \tag{3.1}$$

$$E_\nu = \frac{0.43 E_\pi}{1+\gamma^2\theta^2}, \tag{3.2}$$

where E_π is the energy of the parent pion, m_π the mass of the parent pion, $\gamma = E_\pi/m_\pi$, θ the angle between the parent pion and outgoing neutrino directions, A is the cross-sectional

area and z is the distance from the pion decay vertex.

Equations 3.1 and 3.2 are shown as functions of pion energy for the Medium Energy NuMI Tune in Figure 3.3. The Figure also shows the effect of four off-axis angles (θ = 21 mrads, $\theta = 14$ mrads, $\theta = 7$ mrads and $\theta = 0$ mrads).

Figure 3.4 shows the number of neutrino events as a function of the charged current ν_μ energy for the Low (Figure 3.4a) and Medium (Figure 3.4b) Energy Tune for various off-axis angles. The plots show that as the off-axis angle is increased the mean and width of the energy distribution decreases.

For the Medium Energy Tune, figure 3.3b shows that at 14 mrad the neutrino energy does not have a strong dependence on the parent pion energy. In addition, figure 3.4b shows that at 14 mrad the Medium Energy Tune produces a narrow energy neutrino beam with approximately 4 times more neutrinos at 2 GeV than the on-axis scenario. This peak at 2 GeV is well matched to the expected energy of the first oscillation maximum which is expected to occur at 1.6 GeV for NOvA's L/E (experiment baseline to mean neutrino energy ratio) and for $\Delta \mathrm{m}^2_{32} = 2.4$ meV^2.

As described above, placing the detector off-axis increases the flux at the expected oscillation maximum. In addition, the narrow energy range of the off-axis beam reduces background events. Neutral current events are an important background source whose topologies can be hard to distinguish from electron showers produced by ν_e charged current events. For neutral current events, the neutrino carries a significant amount of the energy away and the energy visible within the detector tends to "feed down" to lower energies. For a narrow band off-axis beam, this feed down tends to shift the neutral current events towards lower energies outside the ν_e appearance signal energy window. Figure 3.5 shows the number of ν_μ, ν_e and neutral current events as a function of visible energy. The bulk of the neutral current events (black histogram) are shown to shift below the signal region (red-hatched histogram).

The combination of reducing beam backgrounds and increasing the neutrino flux at the oscillation maximum means that placing the NOvA detectors at the off-axis angle of 14 mrads enhances the sensitivity to oscillations driven by Δm^2_{23}.

3.2 The NOvA Detectors

The NOvA collaboration performs measurements of both ν_μ disappearance and ν_e appearance and the NOvA detectors are designed to be able to identify the muons and electrons produced in charged-current neutrino interactions. The ν_e appearance analysis has the po-

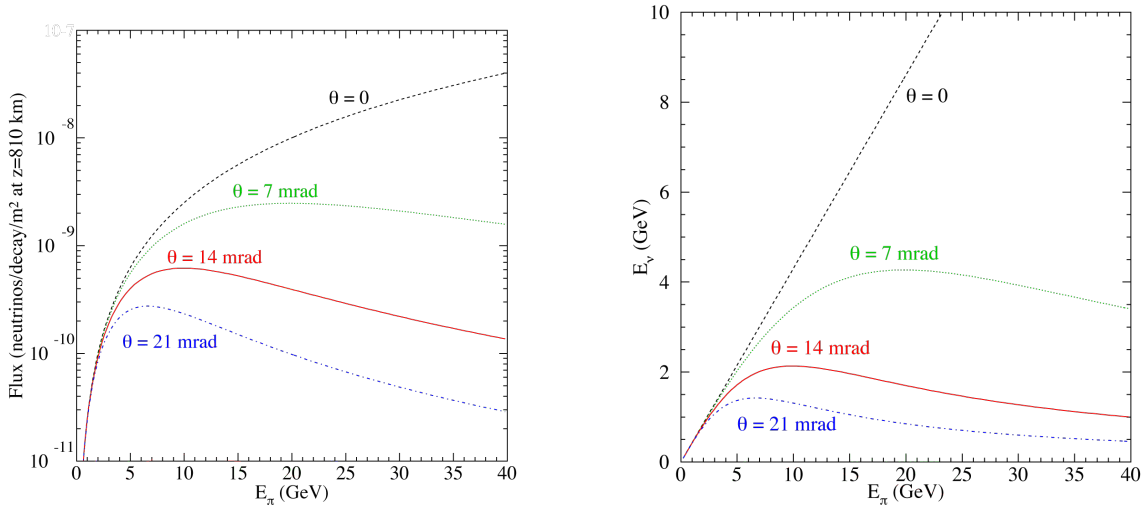

(a) Neutrino flux vs. pion energy.

(b) Neutrino vs. pion energy.

Figure 3.3: The above distributions are for the medium energy tune NuMI beam as viewed from a site located 800 km from the NuMI target and off-axis by an angle θ. The left plot shows the neutrino flux as a function of the energy of the parent pion for different off-axis angles. The right plot shows the neutrino energy as a function of the parent pion energy for different off-axis angles. Diagram taken from [37].

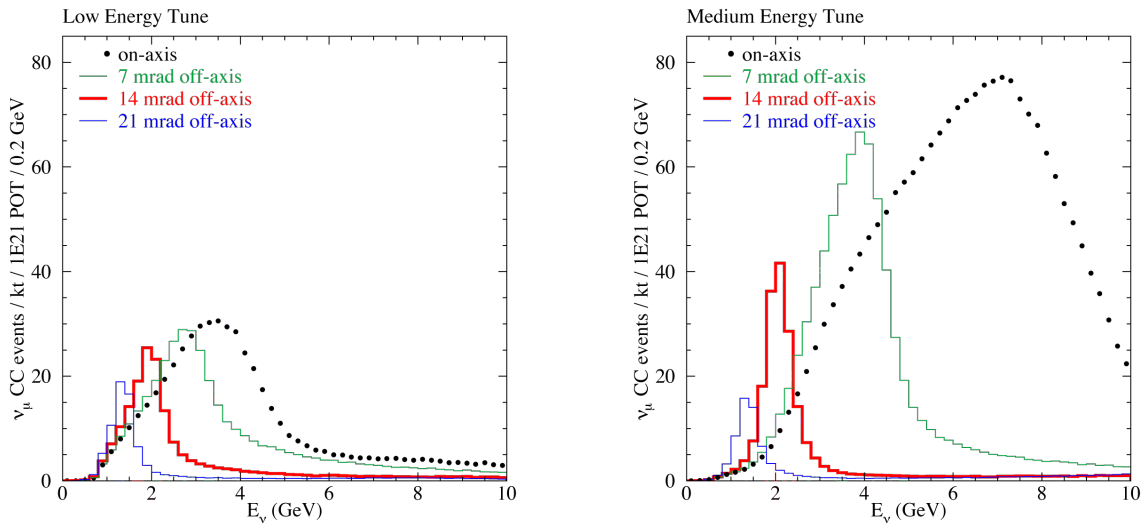

(a) Low Energy Tune neutrino energy.

(b) Medium Energy Tune neutrino energy.

Figure 3.4: Charged current ν_μ event rates vs. neutrino energy in the absence of oscillations. The distributions are found for a detector which is 800 km from the NuMI target and for various off-axis angles. Diagram taken from [37].

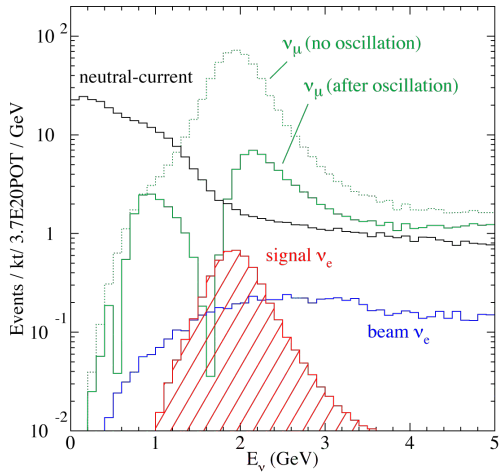

Figure 3.5: Simulated visible energy distributions for ν_μ charged current events with and without oscillations, ν_e oscillation signal events, intrinsic beam ν_e events and neutral current events. The simulation assumes an off-axis position of 12 km at 810 km, $\Delta m^2 = 2.5 \times 10^{-3}$ eV^2, $\sin^2(2\theta_{23}) = 1.0$ and $\sin^2(2\theta_{13}) = 0.1$. Diagram taken from [37].

tential to be overrun with neutral current background events, a large source of background comes from π^0s produced in neutral current events which can fake an electron shower. The NOvA detectors are constructed from low Z materials (primarily carbon) to aid in the distinction between neutrino interaction signatures and the potentially troublesome background events. The constructed detectors have a Moliere radius [19] of approximately 11 cm which is equivalent to the depth (width) of two (three) NOvA cells.

A diagram of the two detectors is shown in Figure 3.6. The near and far NOvA detectors are almost functionally identical. Besides the different masses, there are a few physical differences designed considering the proximity to the NuMI beam and the depth of the detector relative to ground level. The smaller near detector has a so called "muon catcher" and has a higher rate of readout. Whilst the far detector is constructed with an overburden to mitigate the cosmic ray background. The construction common among both detectors will be discussed in the following sub-sections. The details specific to the far and near detectors will be discussed in sub-sections 3.2.7 and 3.2.8 respectively.

3.2.1 The Basic NOvA Detector Element

The basic unit of the NOvA detectors is a rectangular rigid PVC (Polyvinyl chloride) cell which contains liquid scintillator and a wavelength-shifting fibre. Figure 3.8 shows the NOvA cell, looped wavelength-shifting fibre and an example charged particle.

The NOvA cells are made from highly reflective titanium dioxide loaded rigid PVC.

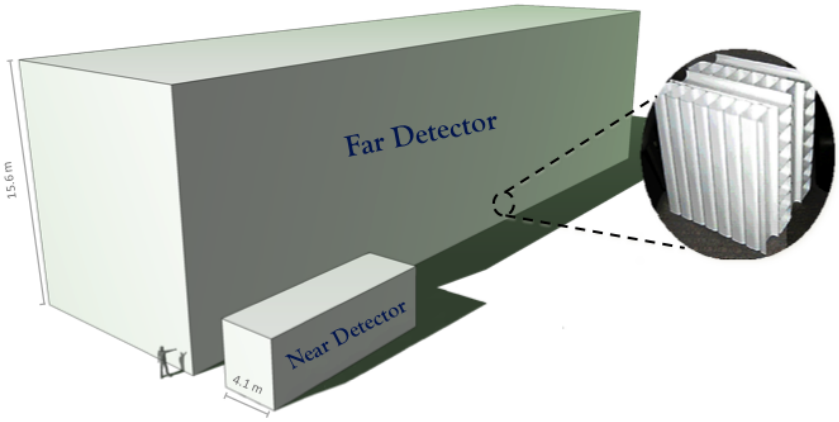

Figure 3.6: Scaled depiction of the near and far NOvA detectors with respect to the average person. The alternating alignment of the NOvA cells is shown by the inset on the right hand side.

The cells have 2 to 4.5 mm thick walls, an interior depth of 5.9 cm along the beam direction and an interior width of 3.8 cm transverse to the beam direction. The thickness of the cell walls varies due to structural considerations. The length of the cells differs between the two detectors, the far detector cells have a length of 15.5 m whilst the near detector cells are 3.6 m long.

The wavelength-shifting fibre, which is twice the length of the cell, is looped at the bottom of the cell such that the captured light travels in two directions to the instrumented top end of the cell. Both ends of the looped fibre are directed onto one pixel of an Avalanche Photo Diode (APD) array. The APD converts the light from the fibre into a digital signal.

3.2.2 Liquid Scintillator

Approximately 65% of the NOvA detector mass is composed of the liquid scintillator held within the cells. The composition of the liquid scintillator is detailed in Table 3.1, which shows that the scintillator is composed mainly of mineral oil along with 5.23% pseudocumene as the scintillant. The scintillant emits scintillation light with a spectrum peaked between 360 - 390 nm. Wavelength shifting chemical additives PPE and bis_MSB are added to shift the initial light spectrum to 400 - 450 nm to match the absorption spectra of the wavelength-shifting fibre.

Component	Purpose	Mass fraction %
mineral oil	solvent	94.63
pseudocumene	scintillant	5.23
PPO	waveshifter	0.14
bis-MSB	waveshifter	0.0016
stadis-425	anti-static agent	0.0010
tocopherol	antioxidant	0.0010

Table 3.1: Chemical composition of the NOvA liquid scintillator [40].

3.2.3 Wavelength Shifting Fibre

The wavelength-shifting fibre has a diameter of 0.7 mm and a core of polystyrene mixed with R27 dye (as the wavelength shifter) at a concentration of 300 ppm. The fibre has two coatings (contributing about 3% of the fibre diameter) of materials with a lower refractive index than the core which facilitates total internal reflection within the fibre. The fibre is first coated with a thin acrylic layer of PMMA and second with fluor-acrylic.

The 400 - 450 nm light emitted by the liquid scintillator is absorbed by the fibre and then wavelength shifted to 490 - 550 nm. As light travels down the fibre it is attenuated, by a factor of about 10 in the far detector, with light in the range 520 - 550 nm preferentially surviving.

3.2.4 Avalanche Photo Diode

The light exiting the fibre ends is detected by an Avalanche Photodiode (APD) and converted into an electronic signal pulse. Figure 3.7 shows a photograph of a NOvA APD containing an array of 32 pixels. Each APD pixel is interfaced with both ends of a single wavelength-shifting fibre. Each APD is connected to a front end board that prepares the signals from the APD for the data acquisition system.

The NOvA APD was chosen because it has an 85% quantum efficiency for the 520 - 550 nm light exiting the fibre ends. The thermal noise generated by each APD is reduced by thermo-electric coolers which cool the APDs to -15°C.

3.2.5 Data Acquisition System

NOvA's data acquisition system continuously reads out all the information from the APDs. The information is temporarily stored in a buffer farm and awaits a decision as to whether

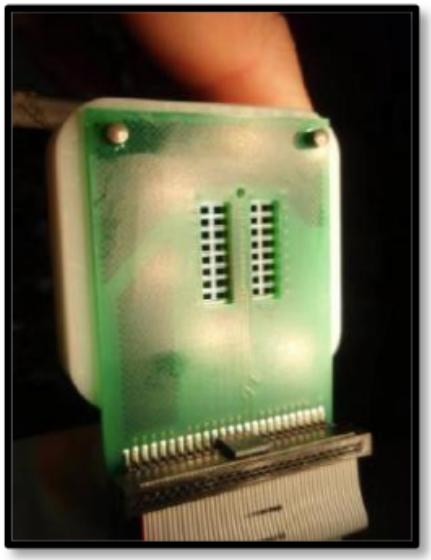

Figure 3.7: The NOvA APD containing an array of 32 pixels.

it should be permanently recorded or rejected. The decision can be made by either online triggering algorithms or by receiving a trigger signal from an external source. The NuMI beam spill signal is an example of an external source trigger.

Each APD is continuously readout by an front end board, which handles the pedestal subtraction and pulse shaping for each signal from the APD. The pedestals are determined for each APD pixel by measuring the baseline noise level. The signal pulses are shaped with a characteristic rise and fall time. When a signal is triggered the signal sample is read out along with the three immediately preceding samples in a process called "multi-point readout". Once the data is permanently recorded, the known pulse shaping parameters are used to fit the four samples and provide more precise timing resolution.

The front end board transmits the digitised data to a data concentrator module, which can take inputs from up to 64 front end boards. Each data concentrator module collects all the information from the connected front end boards during a 50 μs window ("microslice"). This data packet is then sent to and stored in the buffer farm until online trigger processes decide whether to record or reject the data.

3.2.6 Detector Assembly

The NOvA detectors are constructed from the cells described in Section 3.2.1. 16 cells are extruded together in one unit to form an extrusion. Figure 3.9 shows the end-on view of an extrusion with a width of 63.5 cm and depth of 6.6 cm. Two extrusions are placed side by side to form an extrusion module consisting of 32 cells. Figure 3.10 shows an extrusion

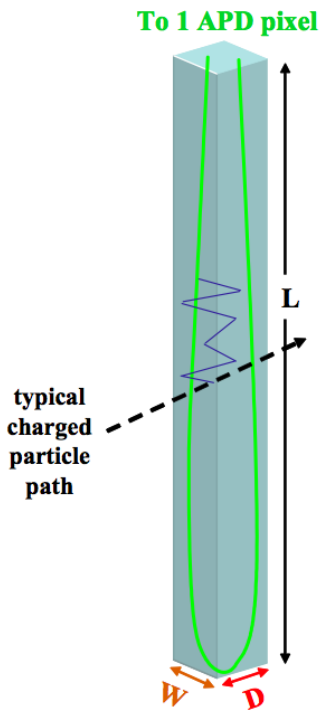

Figure 3.8: A NOvA cell consisting of an extruded PVC tube filled with liquid scintillator and a looped wavelength-shifting fibre. Taken from [37].

Figure 3.9: An end on view of an extrusion constructed from 16 NOvA cells. Taken from [37].

module consisting of 32 cells, end plate, side seal, manifold cover, snout and electronics box. The module ends are capped by the end plate so that the modules can contain the liquid scintillator. The other end is capped by a manifold cover which contains the liquid scintillator in the horizontal cells and directs the 32 fibre end pairs to the 32 APD pixels in the NOvA APD.

Flat planes of cells are constructed from multiple modules glued together side by side. Figure 3.11 shows a cross-section of multiple plane layers and the alternating orthogonal cell orientation. The planes are layered with alternating orthogonal orientations, such that the orientation of the cells making up the plain alternate between horizontal and vertical from plane to plane. The orthogonal orientation of the planes allows for three dimensional reconstruction of tracks passing through multiple planes. Planes are glued together in the orthogonal arrangement described above to form one solid detector piece called a block, consisting of 32 or 24 planes in the far detector or near detector respectively.

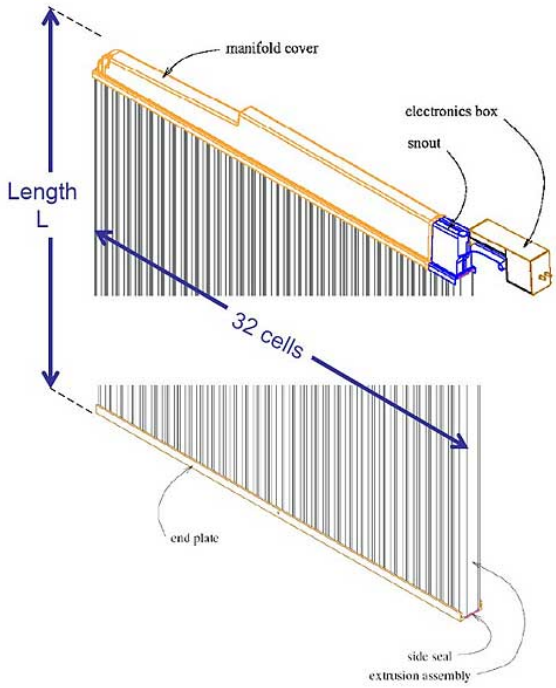

Figure 3.10: A side on view of an extrusion module constructed from two extrusions of 16 cells, an end plate, a side seal, a manifold cover, a snout and an electronics box. Taken from [37].

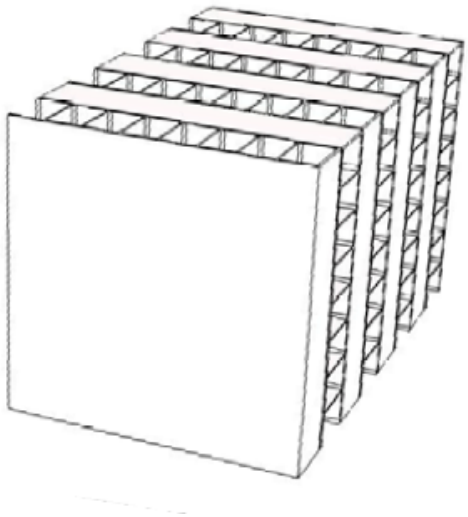

Figure 3.11: Cut out of the NOvA detector showing the alternating orientation of the cells within the stacked planes. Taken from [37].

3.2.7 The Far Detector

The 14 kiloton far detector is located 810 km from the NuMI target, approximately 10 m below ground level and at an elevation of 372 m above sea-level. The neutrino beam enters the detector travelling at an angle of 3° upwards. The detector is constructed, as described in Section 3.2.6, from 344,064 15.5 m long cells which form 896 planes normal to the beam direction. The detector mass is approximately 65% liquid scintillator and 35% PVC.

As described above, the far detector is built on the surface above sea level so cosmic rays will be a major source of background events. The background due to cosmic rays is mitigated using selection cuts and a shielding overburden above the detector. For the ν_μ disappearance analysis the background is primarily due to cosmic ray muons which are almost entirely removed using cuts. For the ν_e appearance analysis, the background is primary cosmic ray photons whose interactions within the detector can be mistaken for an electron shower. During a six year run the far detector without overburden shielding will see approximately 1600 background events due to cosmic ray photons. In order to reduce this background source to less than one event requires approximately 9 radiation lengths of material above the detector surface. Additional radiation lengths will then help to contain any showers caused by interactions within the overburden. With this in mind, the far detector building was constructed with a 122 cm thick concrete enclosure which supports a 15 cm thick overburden of barite. Together, the concrete enclosure and barite overburden provide 12 radiation lengths of shielding.

3.2.8 The Near Detector

The NOvA near detector is located on site at Fermilab next to the MINOS Hall. Figure 3.12 is a diagram of the MINOS Hall area showing the MINOS Shaft, NuMI beam-line, MINOS Hall, NuMI Beam-line, 14.6 mrad off-axis beam and the NOvA Near Detector cavern. The near detector is 105 m underground and 1.015 km from the NuMI target. The near detector therefore sees a higher flux of NuMI neutrino events and a lower flux of cosmic rays than the far detector. The neutrino beam enters the detector travelling downwards at an angle of 3°.

A diagram of the near detector is shown in Figure 3.13. The Figure shows the NOvA Near Detector cavern, access catwalks, and the fully active detector and muon catcher detector sections. The detector is constructed in a similar fashion to the far detector with 20,192 cells arranged in 214 planes, each plane is comprised of 3 modules (except in the muon catcher). The detector has a width and height (except in the muon catcher) of 4.2 m

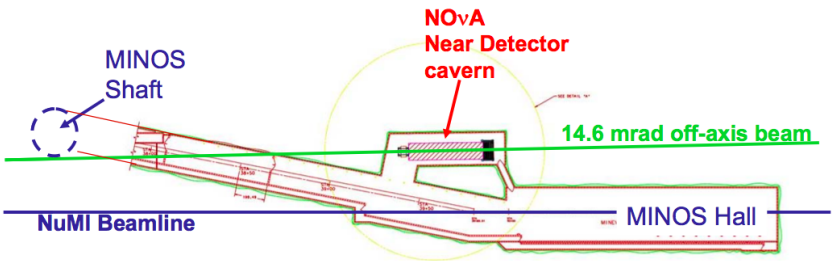

Figure 3.12: Bird's-eye view diagram of the NuMI Beam-line, MINOS Hall, MINOS shaft and the NOvA near detector cavern. Figure taken from [39].

and a length of 15.8 m. The near detector is functionally equivalent to the far detector with the exception of two distinguishing features.

First, a muon catcher is placed at the downstream end of the near detector in order to help range out muons from few GeV charged current ν_μ interactions which would not otherwise stop within the detector. The muon catcher is constructed from layers of steel and liquid scintillator planes. The steel planes are 10 cm thick and are separated by two (one horizontal and one vertically aligned) scintillator planes. The vertical planes consist of three modules while the horizontal planes are made from just two modules. Therefore, the sets of steel and scintillator planes are three modules wide (the same as the rest of the detector) but only two modules high. Ten of these steel and liquid scintillator plane sets are stacked to form the muon catcher. The downstream end of the muon catcher has an additional 3 liquid scintillator planes.

Second, the near detector electronics are setup to sample each channel (APD pixel) four times more frequently (every 125 ns) than in the far detector to help handle the data pileup. The near detector sees approximately 5-10 neutrino interactions per beam spill (10 μs window) while the far detector sees approximately 60-70 cosmic rays per 550 μs window spread out over approximately 17 times more channels. The faster sampling rate improves the timing resolution of hits in the detector. With better timing resolution, pileup events are more easily distinguished from one another.

3.3 Monte Carlo Simulation

The NOvA experiment is simulated using several Monte Carlo packages. The simulation involves several stages, each using information from the previous step. Simulations model the NuMI beam, subsequent neutrino interactions within the detectors, the propagation of particles through the detector geometry, and finally the modelling of the detector response

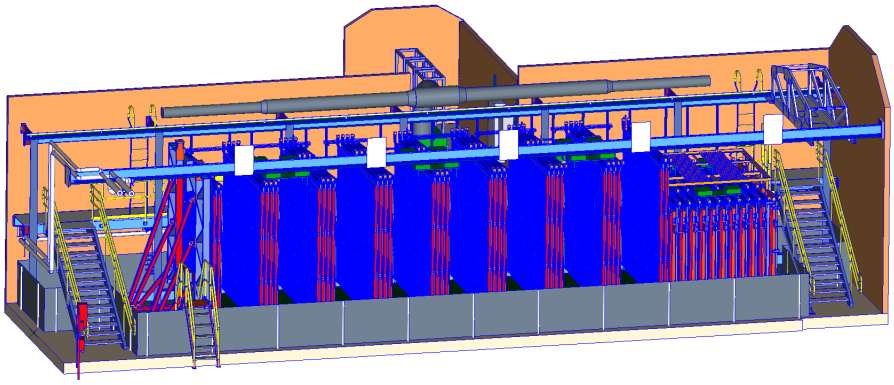

Figure 3.13: Technical drawing of the NOvA near detector and cavern. The NuMI beam enters from the left. The muon catcher planes are shown on the right hand side of the detector. Note that only some of the planes have been drawn to aid visualisation of the detector layout.

to those particles.

The creation and propapagation of the NuMI beam is simulated using FLUKA and Geant4 through the FLUGG interface [41, 42, 43]. The beam simulation produces flux files containing a beam of simulated neutrinos with given flavour, energy and direction. Details of each neutrino's parent are retained in the flux files.

Neutrino interactions within the detector are simulated using GENIE [44]. The flux files produced by the NuMI simulation provide GENIE with a beam of neutrinos. GENIE must decide whether each neutrino interacts within the detector, the type of interaction, the kinematics of the interaction and the location of the interaction vertex. GENIE uses information regarding interaction cross sections and detector geometry to probabilistically determine whether each neutrino interacts within the detector. Figure 3.14 shows the default ν_μ charged current cross section as a function of neutrino energy used in GENIE. The black data points show the results of experimental measurements, the black curve shows the fit of theory to the data and the green shaded band shows the estimated uncertainty. Note that there is no data below 700 MeV. After an initial simulated neutrino interaction the propagation of the resulting primary particles through the nucleus, including inter-nuclear scattering and absorption, is also simulated by GENIE. Cosmic ray generation well above the detector is simulated using CRY [45].

Genat4 is used to simulate the propagation and energy deposition within the detector of the particles produced by GENIE or CRY. Interactions of the primary particles within the detector and the resulting secondary particles are also simulated. The resulting energy depositions within the detectors liquid scintillator are recorded and are known as Fibre

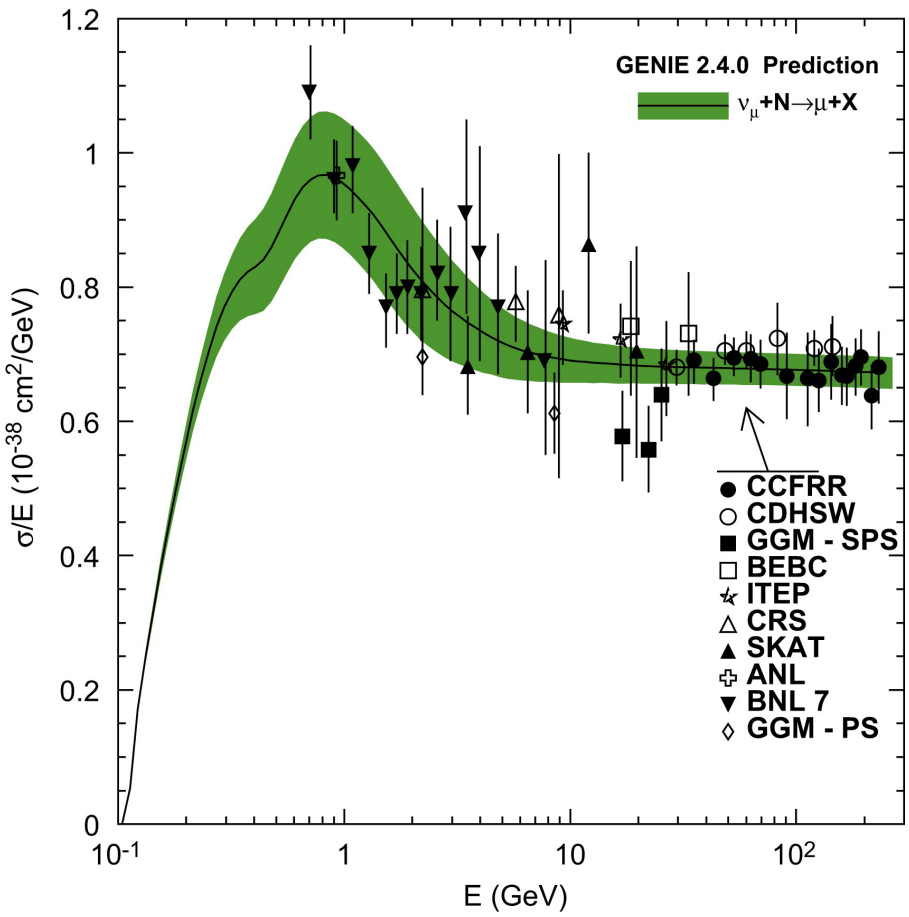

Figure 3.14: Default cross section in GENIE for ν_μ charged current scattering with an isoscalar target. The shaded green band shows the estimated uncertainty on the free nucleon cross section. [44]

Liquid Scintillator Hist (FLSHits).

Next two NOvA specific software modules are used to simulate the response of the NOvA detectors to energy depositions [46, 47]. The first module simulates the processes from FLSHit in a NOvA cell to photons arriving at the APD. The final APD signal is a combination of the photons arriving at the APD and the APDs modelled response to noise. The second module simulates the response of the FEBs to the APD signals.

Chapter 4

NOvA Analysis Methodology

This chapter presents an overview of the methodology of the second muon neutrino disappearance analysis. The methodology represents the chain starting with raw detector hits and ending with the sensitivity and result contours. Particular focus is given to components of the analysis chain for which the author made a significant contribution. The second disappearance analysis summary [48] and the second analysis disappearance paper [49] are both used as references throughout.

4.1 Event Reconstruction

The reconstruction begins with a collection of above threshold APD signals clustered in space and time [50, 51]. These collections of APD signals are used to reconstruct event candidates [50]. The trajectories of charged particles within an event are reconstructed using a technique based on the Kalman filter algorithm [52] [53]. An example far detector event with tracks found using the NOvA Kalman filter is shown in Figure 4.1. The top and bottom halves of the Figure show the x and y-view of the detector respectively. Histograms of the hit time and hit charge are shown at the bottom left and right respectively. The reconstructed tracks are each indicated by the different coloured lines.

The NOvA Kalman tracker is used to estimate the true trajectory of a particle within the detector given positions of cell hits within an event. Trackable particles are characterised by trajectories with long straight sections, dominated by small angle multiple scattering, and intermittent large scattering angles caused by electromagnetic or strong interactions [53]. The track finding process initially starts from the downstream end of the detector, where particles emerging from a NuMI interaction will (on average) be the most separated, and proceeds upstream. Track finding and fitting is performed separately

in each detector view since the trajectory in each view is independent. Later the views are matched to reconstruct three dimensional tracks [53].

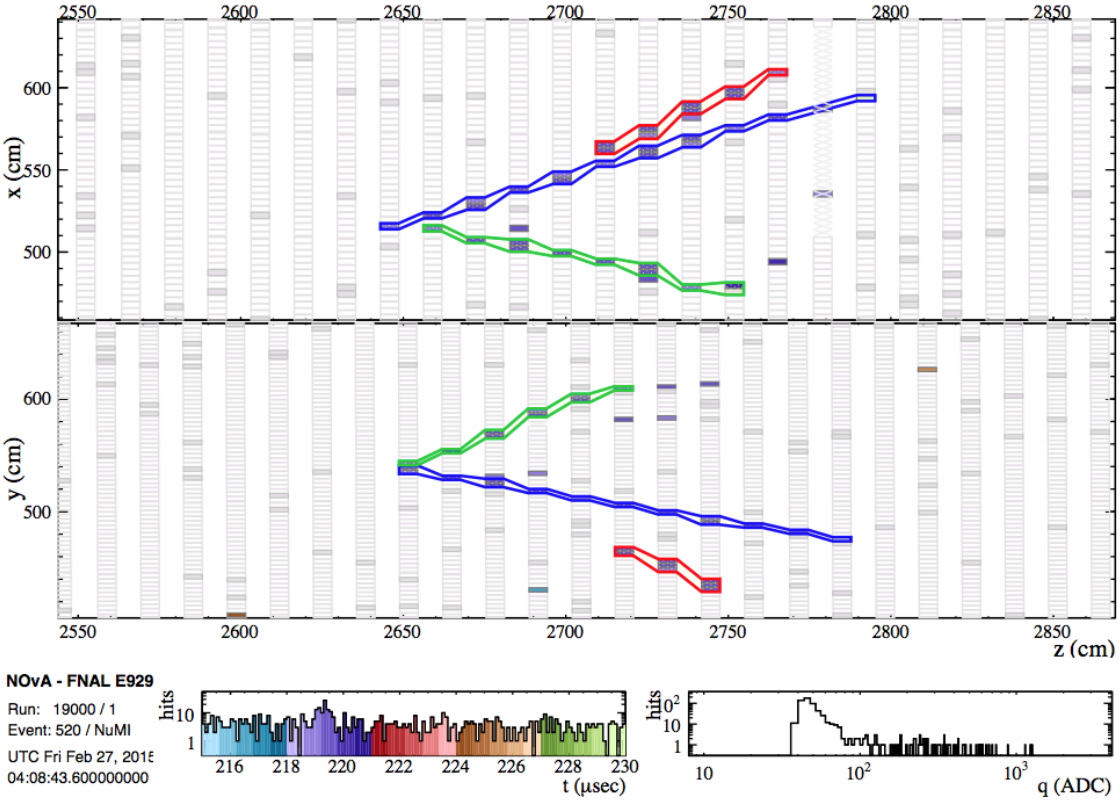

Figure 4.1: Example of reconstructed tracks found using the NOvA kalman tracker in the far detector simulation. Individual reconstructed tracks are shown by the red, blue and green lines. The x-position and y-position views are shown in the top and bottom half of the figure respectively. This figure taken was from the NOvA Kalman track technical note [53].

4.2 Selection and Background

A series of selection packages are used to identify charged-current muon neutrino events within the detector and also to reject background events. The two main sources of background to the muon neutrino disappearance analysis are cosmic ray muons and beam induced backgrounds including neutral current, ν_e charged current and ν_τ charged current events. The good spill, data quality, cosmic, containment and reconstructed particle identification selection packages are described in the following paragraph.

The beam background events are estimated using the simulation for each detector. Events passing the selection but failing a truth cut requiring a muon or anti-muon neutrino are deemed to be background. The cosmic background (mostly secondary cosmic ray

muons) is estimated using two samples of far detector data which occur outside of the beam spill window. The first sample is taken using the timing sidebands of the data collected with the NuMI trigger. This sample matches the exposure of the detector to the NuMI beam but the shape of the neutrino energy distribution is statistically limited. The second sample is taken using a cosmic trigger where data is collected for activity within the detector outside of the beam-spill window. This second sample contains more events and provides a better shape but does not match the far detector exposure. Figure 4.2 shows the estimated number of cosmic background and signal events after each successive selection is applied to the sample. As shown in Figure 4.2, selections are made for good spills, data quality, cosmic rejection, containment and neutral current rejection. The first selection, at the top of Figure 4.2, is the good spill selection which requires that the NuMI beam is produced within acceptable bounds of spill time ($< 0.5 \times 10^9$ seconds), spill POT ($> 2 \times 10^{12}$), horn current (-202 kA $< I < -198$ kA), proton beam position on NuMI target (-2 mm $< pos(x, y) < 2$ mm) and beam width (0.57 mm $< width(x, y) < 1.58$ mm) [54] [55].

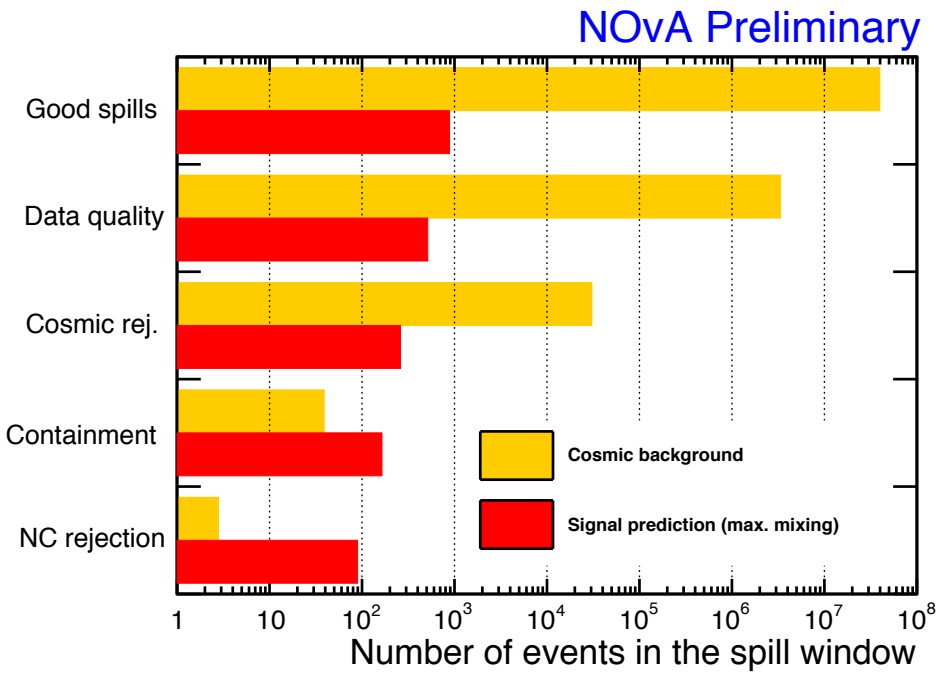

Figure 4.2: The number of signal events (red) and cosmic background events (yellow) surviving each successive analysis selection. The signal is estimated from the simulation and the cosmic background is estimated from the timing sidebands of the NuMI trigger. Figure taken from [56].

p

Next, the data quality selection removes events with problems in one or more data concentrator modules. The selection requires that: no data concentrator modules completely drop out during the spill, tracks do not all stop at DCM edge boundaries (this signals that the detector is out of sync and uses a DCM edge metric [57]), and fracdcm3hits < 0.45. Where is this defined? Is there a technote?.

The cosmic rejection selection utilises a boosted decision tree (BDT) to create a cosmic rejection particle identification variable [58]. The BDT is passed 11 variables including the angle of the track relative the NuMI beam direction, maximum height of activity within the detector, length of the track and the number of hits.

A selection is made to ensure the events used for the analysis are fully contained within the detector. This selection serves two purposes, it ensures all the energy from a muon neutrino charged current interaction is deposited within the detector. The selection also assists the rejection of cosmic rays in the far detector and rock muons (from interactions of neutrinos in the rock upstream of the detector) in the near detector. The containment selection uses both the kalman tracks reconstructed as described in Section 4.1 and the hits to select fully contained events. The hit component of the selection requires that there are no hits in the outer two cells in either view and also no hits in the first or last two planes of the detector. The track component of the selection requires that the forward or backward projection from the end or start of the kalman track passes through at least 10 cells before exiting the detector.

The near detector has a slightly different selection to account for the muon catcher and the relative absence of the cosmic ray muon background. As described in Section 3.2.8, the muon catcher at the downstream end of the near detector is 2/3 the height of the fully active detector. The differences with respect to the far detector containment selection are as follows. The projection cut is loosened to at least 4 planes projected forward and at least 8 planes projected backwards. The start position of the kalman track must occur in the fully active detector upstream of the muon catcher. The kalman track must either end within the fully active detector or the position of the track within the detector at transition from fully active to muon catcher must be below the height of the muon catcher. [48]

A k-nearest neighbours (kNN) classifier [59] known as Reconstructed Muon Identification (ReMId) is used to identify muon candidates among the particle trajectories within an event [60]. The Reconstructed Muon Identification algorithm uses the following four variables to distinguish muons from pions using the kNN classifier: dE/dx, scattering, track length and fraction of plains along the track consistent with additional hadronic

energy depositions. The kNN output is a score for each event, the distribution of ReMId scores is shown in Figure 4.3, the muon neutrino charged current signal events are shown by the black histogram which peaks close to 1 and the neutral current background events are shown by the red histogram. For each event passing the preceding cuts, the particle with the highest ReMId score is designated as the primary muon track. Events with ReMId > 0.75 are taken as muon neutrino charged current interactions, in the far detector this selection results in a signal efficiency and purity for contained events of 81% and 95% respectively. Where the impact of neutrino oscillations on the efficiency and purity is approximately accounted for by setting $\Delta m^2_{32} = 2.5 \times 10^{-3}\text{eV}^2$ and $\sin^2\theta_{23} = 0.5$ [60] [61].

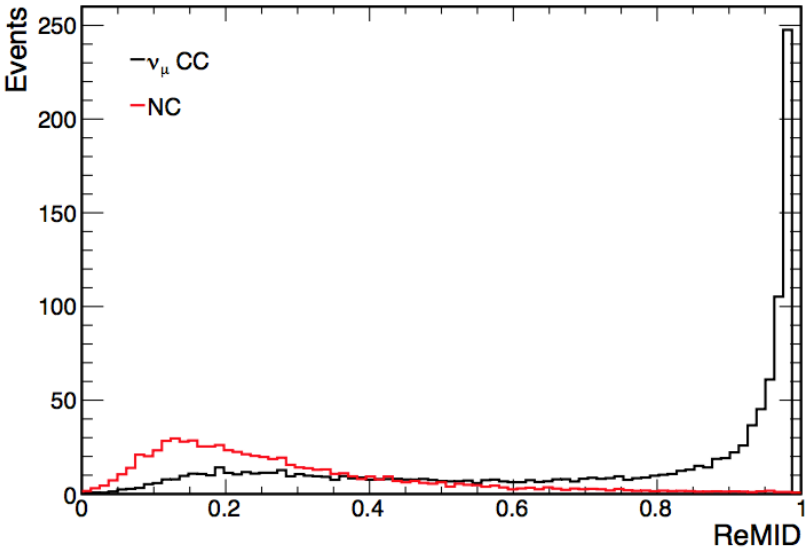

Figure 4.3: Reconstructed Muon Identification distribution for muon neutrino charged current events (black histogram) and neutral current events (red histogram). For the standard analysis events are required to have a ReMId score of 0.75 or greater. Figure taken from [61].

An alternative method called Convolutional Visual Network (CVN) for selecting muon neutrino charged current events has recently been developed. The CVN algorithm identifies muon neutrino charged current events based on the event topology and does not require detailed event reconstruction. The output from the muon neutrino charged current event classifier is shown in Figure 4.4. The signal events are shown by the blue histogram. The background neutral current, appearance ν_e and inherent beam ν_e events are shown by the blue, purple and pink histograms respectively. [62]

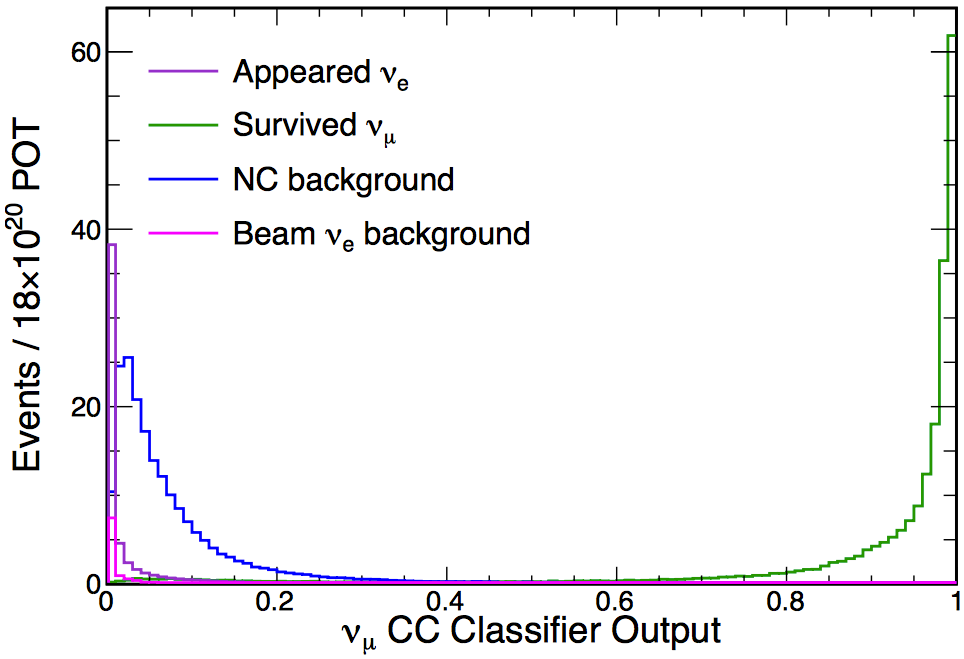

Figure 4.4: Output of the Convolutional Visual Network for muon neutrino charged current event identification. Muon neutrino charged current events are shown by the green histogram. The backgrounds of neutral current events are shown by the blue histogram, appearance ν_e events are shown by the purple histogram and the inherent beam ν_e events are shown by the pink histogram. Figure taken from [62].

4.3 Calibration

NOvA's energy calibration is performed in three stages. The attenuation calibration corrects the detector response along the NOvA cells using through going muons. The attenuation corrected response should be uniform across the detector. The absolute energy calibration uses muons that stop within the detector to find a constant to convert the attenuation correct response into physically meaningful units of GeVs. The drift calibration accounts and adjusts for the variation of the detector response with time caused by seasonal effects and instrument degradation.

4.3.1 Attenuation and Threshold Calibration

The attenuation calibration uses the energy depositions of through-going cosmic ray muons to produce constants and formulae such that such that the corrected detector response to energy depositions is uniform across the detector. Attenuation fits are performed on a channel by channel basis, in other words the detector response along the length of each NOvA cell is fitted to produce a calibration for that cell [63].

Before calibrating, the detector response is divided by the the path-length (through a cell) to reduce the impact of variations in path-length arising from reconstruction efficiencies of different track angles. To provide an accurate path length estimation only hits which have neighbouring hits from the same track in the two directly adjacent cells within the same plane are used for the calibration. Using this selection allows the path-length through a cell to be calculated from the cell width and the angle of the track.

Figure 4.5 shows the uncalibrated detector response along the length of a NOvA near detector cell, data and a fit to the data are shown by the black points and the blue curve respectively. The fit to the data is used to provide constants that correct the detector response within the cell such that the response is uniform across the detector. [63] [64]

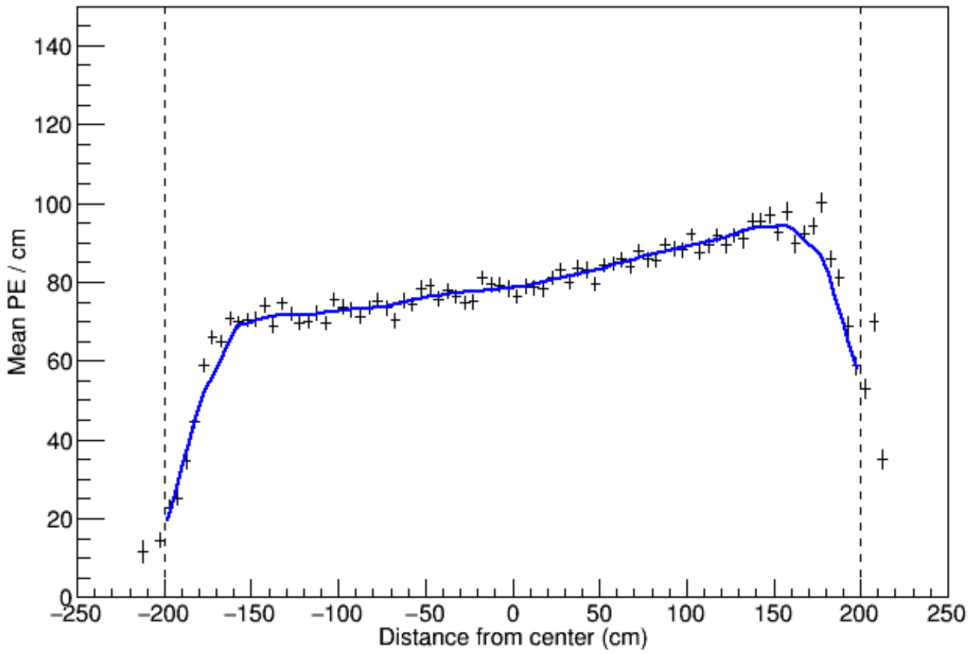

Figure 4.5: An example of a detector response (PE/cm) vs. distance from cell centre curve in the NOvA near detector. The data is shown by the black points with statistical errors. A fit to the data is shown by the blue curve. Figure taken from [63].

4.3.2 Absolute Calibration

The absolute calibration method is described in the first analysis absolute calibration technical note [65]. The results of the second analysis calibration and the differences compared to the first analysis are described in the second analysis absolute calibration technical note [66]. The NOvA absolute calibration uses the energy deposited by stopping muons as a standard candle. To reduce systematic uncertainties, only those energy deposits

in a 1-2 m window away from the muon track end point are used. The mean of the detector response distribution is found for data and MC in both near and far detectors. The mean of the distribution of true energy deposits in the track window is used to provide a conversion factor between the detector response and the true energy deposited in the scintillator for minimum ionising muons. Figure 4.6 shows the resulting calibrated dE/dx distribution of stopping muons in NOvA's far detector. [65]

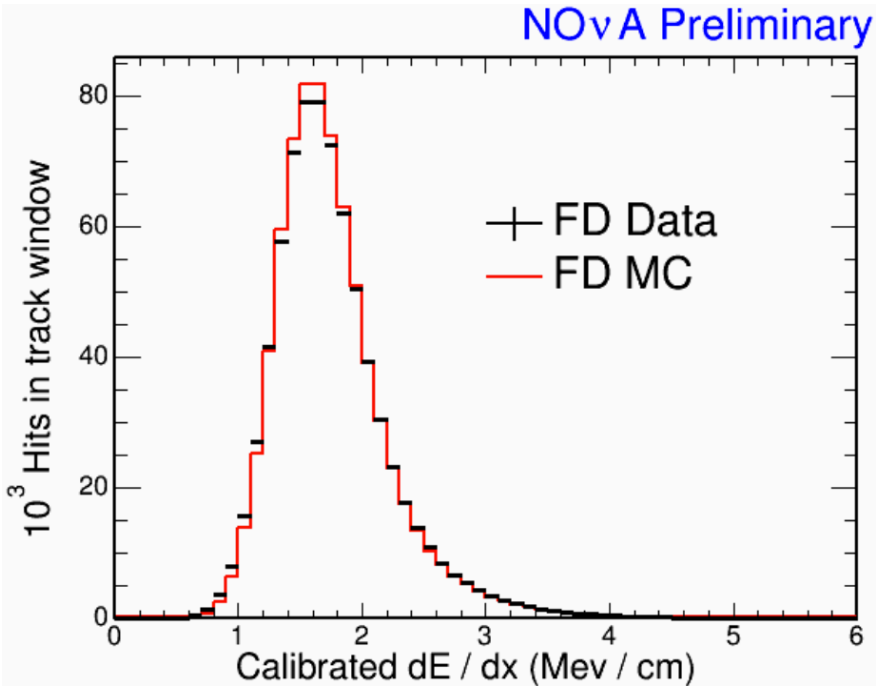

Figure 4.6: Calibrated dE/dx (MeV/cm) for hits within the 100 cm track window in the NOvA far detector. Data and simulation are shown by the black points and red histogram respectively. Figure taken from [65].

4.3.3 Drift Calibration

A drift calibration is being developed to account for variations in the detector response with time. At the point of writing this stage of the calibration is not yet implemented.

4.3.4 Timing Calibration

The aim of the timing calibration is to precisely synchronise each detector externally with the neutrino beam and internally among the electronic detector components. The internal timing calibration measures and accounts for timing offsets between data concentrator modules (see 3.2.5) using hit times from cosmic ray tracks crossing multiple data concentrator modules. [67]

4.4 Energy Reconstruction

The neutrino energy is estimated with a resolution of approximately 7% from the muon and hadronic energy. The muon energy is estimated with a resolution of 3.5% using the length of the track within the detector. As a consequence, the energy of muon's that do not stop within the detectors cannot be estimated with the same accuracy. The visible hadronic energy is estimated from the calibrated detector response (see Section 4.3) of hits not associated with the muon track. The simulation is used to create a conversion function from visible hadronic energy to total hadronic energy using a linear fit. The total hadronic energy is estimated, with a resolution of 25%, from the visible energy using the conversion function. [49]

4.5 Extrapolation

The NOvA near detector is used to compare distributions resulting from neutrino interactions in data and simulation. Any significant difference between the two means that a process exists that is not correctly modelled in the simulation. The differences in the near detector neutrino energy spectrum between data and simulation are extrapolated to predict the far detector neutrino energy spectrum. The extrapolation accounts for neutrino oscillations, acceptance differences and flux differences between the near and far detector.

The extrapolation proceeds in stages. First, simulation estimated background is subtracted from the the near detector data spectrum. A reconstructed to true neutrino energy matrix obtained from the near detector simulation is used to convert the background subtracted reconstructed neutrino energy into a true energy spectrum. A far-to-near detector event ratio is used to account for the effect of neutrino oscillations and the different acceptances of the two detectors. The true neutrino energy spectrum is multiplied by the far to near event ratio as a function of true neutrino energy to produce the far detector true neutrino energy spectrum. The far detector true neutrino energy is converted back to reconstructed neutrino energy using the far detector reconstructed to true neutrino energy matrix obtained from the far detector simulation. Finally, background events due to cosmic rays (from data) and beam backgrounds (from MC) are added to the extrapolated far detector reconstructed neutrino energy distribution to form a prediction that will later be compared to the far detector data. [49]

4.6 GENIE Tune

Recently other experiments have presented evidence suggesting an additional process contributing to the neutrino interaction event rate [68]. The distribution of hadronic energy in the NOvA near detector data provides supporting evidence for the additional process [69]. For the second analysis the simulation was adjusted to include a semi-empirical model of the so called two-particle two-hole (2p2h) process where neutrinos scatter from nucleon pairs within the nucleus via a meson exchange current (MEC) between the nucleons. The model is motivated by observations of a rate enhancement in electron on nucleus scattering where the discrepency is modelled via the additional 2p2h process including meson exchange currents [70].

Figure 4.7 shows the quasi-elastic cross section vs. reconstructed neutrino energy for data taken with the MiniBooNE (red circles) and the NOMAD (blue stars) experiments. The MiniBooNE and NOMAD experiments measured the cross section for neutrino interactions with reconstructed neutrino energy in the ranges $0.4 - 2$ GeV and $4 - 80$ GeV respectively. At low energy MiniBooNE data shows good agreement with the Fermi Gas model with an axial mass of 1.35 GeV. At higher energies NOMAD data [71] shows good agreement with the Fermi Gas model with an axial mass of 1.03 GeV (the free nucleon cross section). The NOMAD data indicates agreement with the free nucleon cross section, implying the multi-nucleon process is not present at higher energies. Therefore, the GENIE MEC cross section is set to vanish above 5 GeV where data indicates agreement with the free nucleon model. This suggests a cross section simply switching off, which is not expected for a physical process.

Several changes were made to fix the limitations of the semi-empirical model described above. Figures 4.8a, 4.9a and 4.10a show the effect of the adjustments made to the simulation on the agreement between data and MC in the near detector. Corresponding ratios of data over MC are shown in Figures 4.8b, 4.9b and 4.10b. First of all, weighting functions were used to correct the basic 2p2h-MEC cross section behaviour. The n-p initial state in GENIE is weighted up by a factor of four while the n-n initial state is weight down by a factor of four. The linear reduction of the cross section for 2p2h-MEC events is corrected producing a flat cross section above 1 GeV. The effect of these two adjustments on the energy distributions is shown by the dotted blue histogram (labelled "fixInitState&XSec") in the Figures. The dotted green curve (labelled "Tufts2p2hWgt") shows the MC distributions after the 2p2h cross section is reweighted as a function of q_0 and $\vec{q}$. This is done using comparisons between the stock GENIE MEC events and

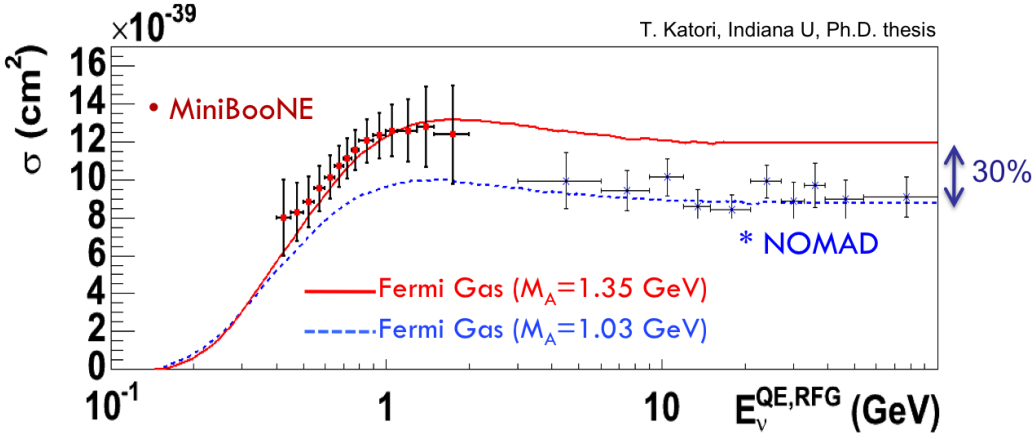

Figure 4.7: Charged current quasi-elastic cross section vs reconstructed neutrino energy for MiniBooNE (red circles) and NOMAD (blue stars). The solid red and dotted blue curves show the theory predictions based on modelling the nucleons as a fermi gas with an axial mass of 1.35 and 1.03 GeV respectively. Figure taken from [72].

the quasi-elastic events. Finally, the dotted magenta histogram (labelled "TuftsWeight") shows the MC distributions after all the above adjustments are made in combination with reweighting GENIE deep inelastic scattering with an invariant mass < 1.7 GeV down by 35%. [69]

As mentioned above, the dotted magenta histogram in Figures 4.8a, 4.8b, 4.9a, 4.9b, 4.10a and 4.10b shows the final MC distributions after the adjustments described above are applied. Figure 4.8b shows that the data/MC ratio for the hadronic energy distribution is improved after the inclusion of 2p2h events along with the combination of adjustments. However, there is still a large discrepency between the near detector data and MC in the range $1 - 2.5$ GeV. This means that the hadronic component of events will be worse resolved for higher values of hadronic energy. Figure 4.9b shows the data/MC ratio for muon energy. Before including MEC (red histogram) MC generally underestimates the event counts for each muon energy bin, particularly in the range $1 - 3$ GeV. After including the 2p2h events and making the adjustments (dotted magenta histogram) the MC underestimates the event count below about 1 GeV, close to matches the data between 1 and 1.5 GeV, and overestimates the event count per bin above 1.5 GeV. Figure 4.10b shows the data/MC ratio for neutrino energy. Compared to the simulation excluding 2p2h (red histogram), the addition of 2p2h along with the adjustments improves the data/MC ratio below 1.75 GeV and in the range $3.5 - 4$ GeV. However, the ratio worsens the in the range $2 - 3.5$ GeV.

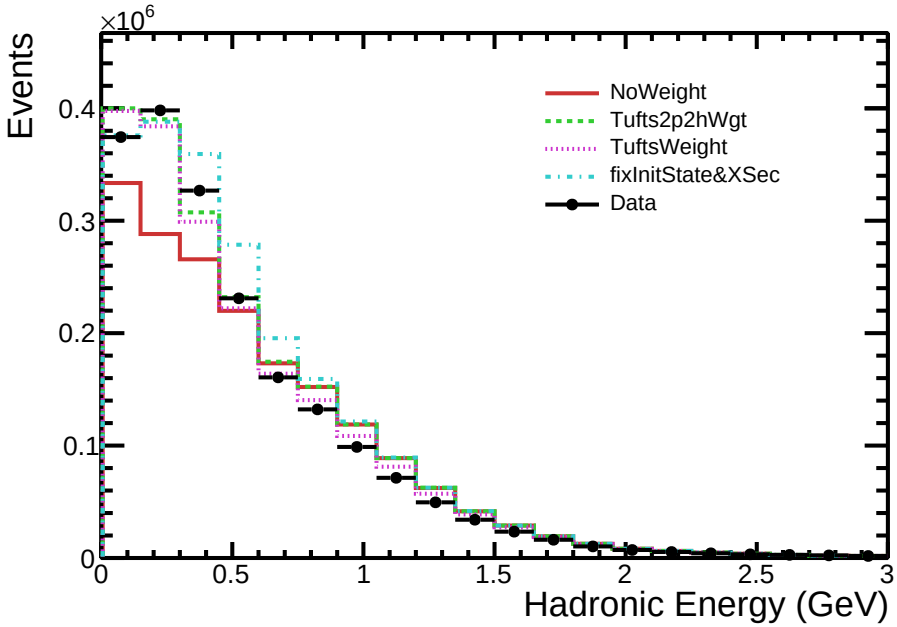

(a) Comparison of hadronic energy distributions.

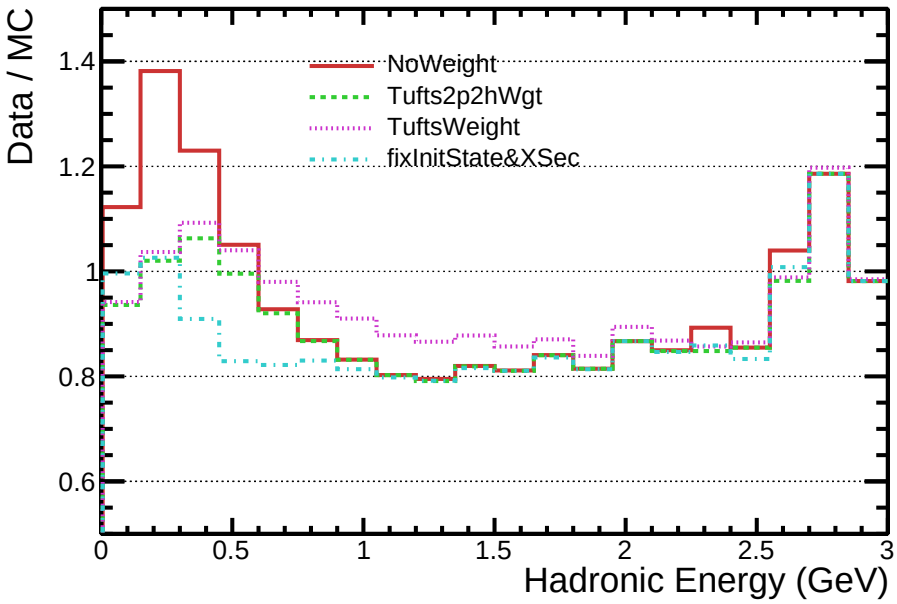

(b) Comparison of data/MC for each bin of hadronic energy for each 2p2h-MEC weight applied to the MC.

Figure 4.8: Comparison between data and MC hadronic energy distributions in the near detector. MC distributions are shown for each stage of the modifications made to the additional 2p2h-MEC process included in the GENIE for the second analysis. The case where 2p2h events are not included is shown by the red histogram.

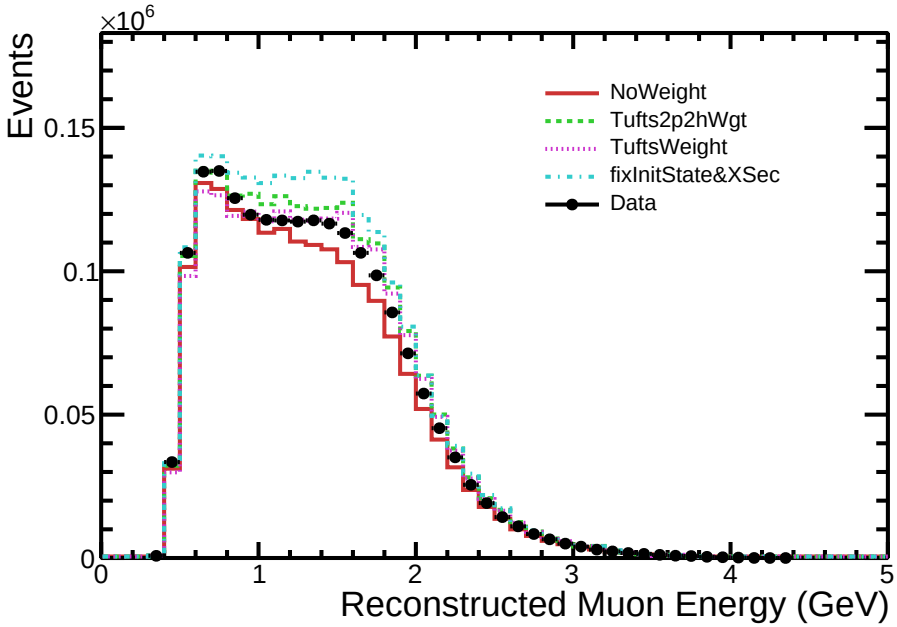

(a) Comparison of muon energy distributions.

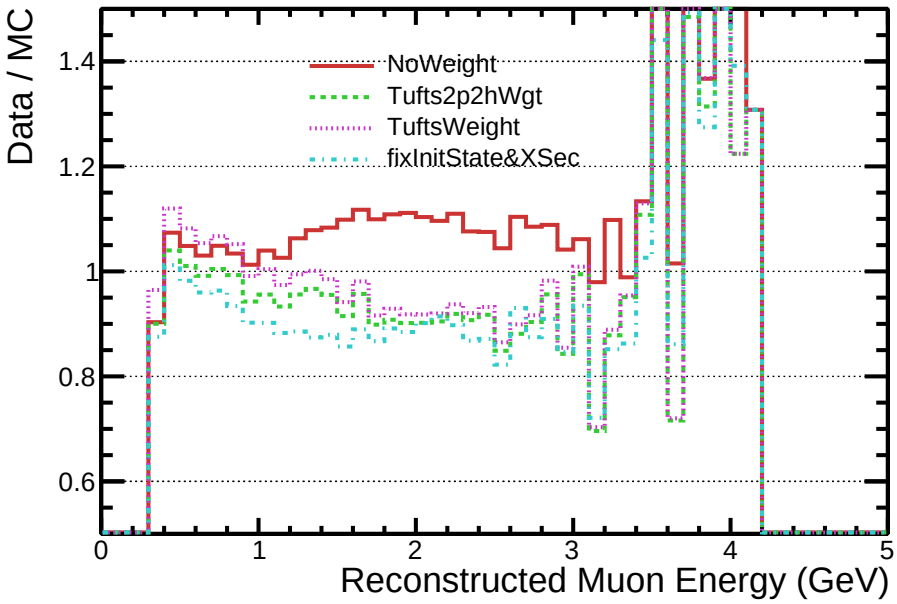

(b) Comparison of data/MC for each bin of muon energy for each 2p2h-MEC weight applied to the MC.

Figure 4.9: Comparison between data and MC muon energy distributions in the near detector. MC distributions are shown for each stage of the modifications made to the additional 2p2h-MEC process included in the GENIE for the second analysis. The case where 2p2h events are not included is shown by the red histogram.

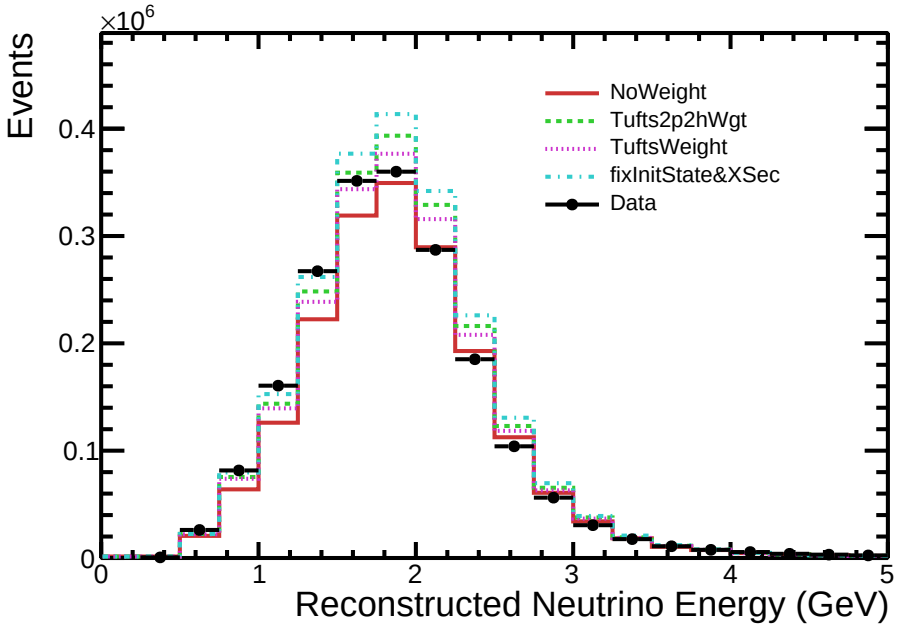

(a) Comparison of neutrino energy distributions.

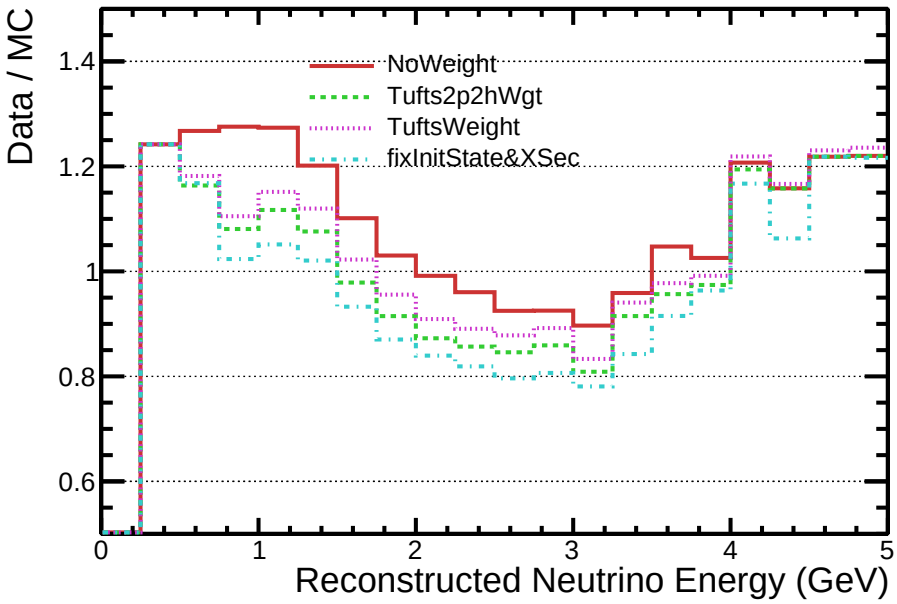

(b) Comparison of data/MC for each bin of neutrino energy for each 2p2h-MEC weight applied to the MC.

Figure 4.10: Comparison between data and MC neutrino energy distributions in the near detector. MC distributions are shown for each stage of the modifications made to the additional 2p2h-MEC process included in the GENIE for the second analysis. The case where 2p2h events are not included is shown by the red histogram.

4.7 Evaluation of Systematic Uncertainties

For the second muon neutrino disappearance analysis the effect of systematic uncertainties on the neutrino, muon and hadronic energy distributions were studied and quantified in terms of shifts to the mean and integral after applying the appropriate systematic shift to the simulation. Monte Carlo samples were created with systematic shifts or alternative physics models (such as noise modelling) applied before the reconstruction stage of the simulation production. A summary of the percentage shifts in hadronic energy, muon energy, neutrino energy and normalisation due to each of the systematic samples is shown in Table 4.1.

The impact of systematic uncertainties in the GENIE model and beam intensity effects were studied in [73] and [74] respectively. The intensity effect uncertainty is defined, by the uncertainty in the number of events per beam spill, as no more than a 0.7% normalisation shift in the near detector.

Later in the analysis when performing the fit, the systematic shifts to the hadron energy, muon energy, neutrino energy and normalisation will be used to account for each source of uncertainty. The systematic shifts to the energy variables and normalisation is accounted for in the oscillation analysis by creating additional muon neutrino energy histograms (for each detector) for each possible combination of systematic shifts in mean or normalisation applied to the variables before filling. When performing the fit the histogram formed from the combination of systematic shifts that produces the lowest χ^2, at each point in the oscillation parameter space, is used.

4.7.1 Calibration

The data/MC ratios of calibrated muon energy as a function of distance from the cell centres are used to define calibration shape systematics for the x and y-view cells independently. The y-view cells display the most extreme disagreement between data and MC in terms of calibrated response along the cells. In comparison the disagreement between data and MC in the x-view cells is negligible and is currently neglected in the analysis of systematics [66].

A comparison of proton energy in the data and MC is used to define an uncertainty of $\pm 5\%$ for the energy scale of hadronic showers [75]. The effect of the 5% calibration uncertainty is evaluated using MC samples generated with a $+5\%$ or -5% shift applied, these samples are referred to as the "XY" shifted samples. The effect of the calibration uncertainty along the length of the y-view cells was analysed using a MC sample generated

Systematic sample	Percentage shift in: Mean $E_{had.}$	Mean E_{μ}	Mean E_{ν}	Normalisation
ND XY neg. shift	-4.97	-0.34	-1.60	+1.16
ND XY pos. shift	+4.79	+0.82	+2.01	-1.76
ND Y-func. shift	-1.53	-0.10	-0.47	+0.49
FD XY neg. shift	-5.02	+0.65	-0.90	-4.02
FD XY pos. shift	+4.89	-0.15	+1.28	+1.12
FD Y-func. shift	-1.48	+0.16	-0.30	-0.91
ND Birks B	-3.92	-0.40	-1.37	+3.06
ND Birks C	-0.26	-0.34	-0.28	+2.51
FD Birks B	-5.02	+0.20	-1.25	+1.49
FD Birks C	-0.64	-0.19	-0.32	+1.28
FD new noise model	+1.29	-0.02	+0.36	+0.25

Table 4.1: Percentage shifts in the energy variables and normalisation when comparing a systematically shifted sample to the baseline simulation. The normalisation is found using the neutrino energy distribution in the range 0 to 5 GeV.

with a functional shift to the calibration of hits in the y-view cells, this sample is referred to as the "Y-func." shifted sample. The shift in hadron, muon and neutrino energy for each sample was analysed in [76].

Distributions of the hadronic energy, muon energy, neutrino energy and reconstructed minus true over true neutrino energy are shown for the near detector "XY", near detector "Y-func.", far detector "XY" and far detector "Y-func." shifted samples in Figures 4.11, 4.12, 4.13 and 4.14 respectively. For each plot shown in the Figures the standard baseline simulation is shown for comparison. In both detectors the "XY" shifted sample causes a larger shift (compared to the "Y-func." sample) to the mean hadronic, muon and neutrino energy and the normalisation as can be seen in Table 4.1. [76] The table shows that the shifts in the near and far detector normalisation due to the calibration uncertainty samples ("XY" and "Y-func.") are anti-correlated.

4.7.2 Birks

Generally, the observed light yield from a scintillant is proportional to the energy loss rate of the through going particle, dE/dx. However, at high energies the light yield is no longer proportional to the energy loss rate. At higher energies the light yield, L, is given by

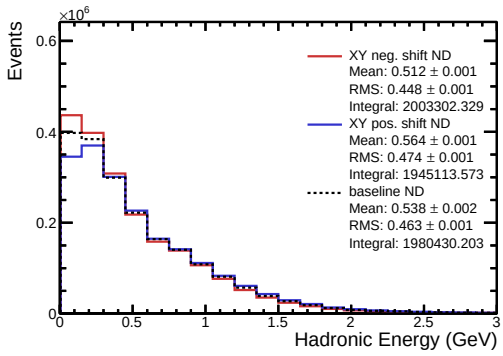

(a) Hadronic energy

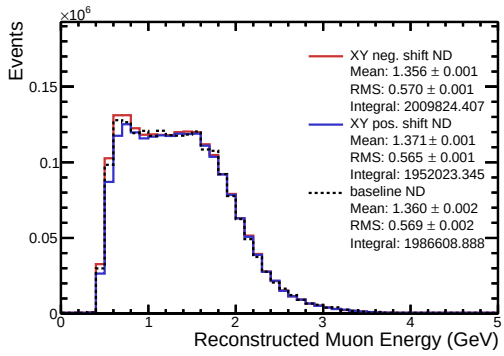

(b) Muon energy

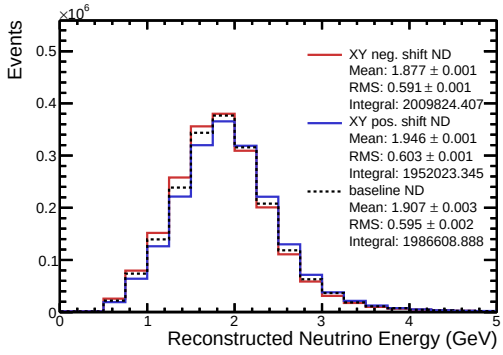

(c) Neutrino energy

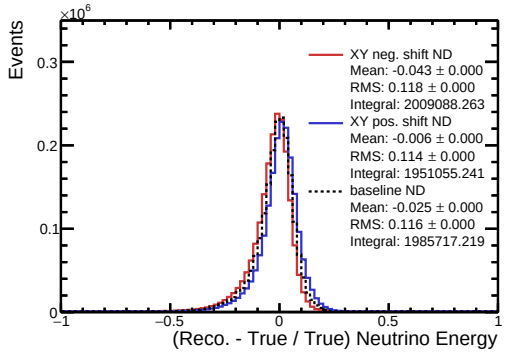

(d) (Reconstructed - true) / true neutrino energy

Figure 4.11: energy distributions for the baseline, xy negatively shifted and xy positively shifted near detector simulation shown by the dotted black, solid red and solid blue histograms respectively.

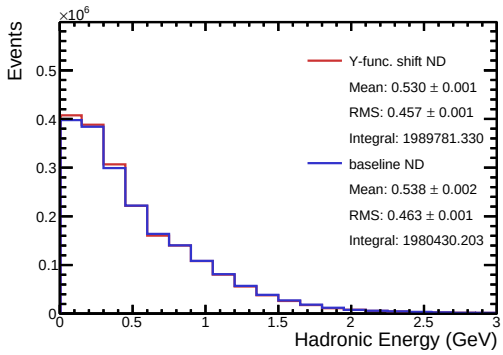

(a) Hadronic energy

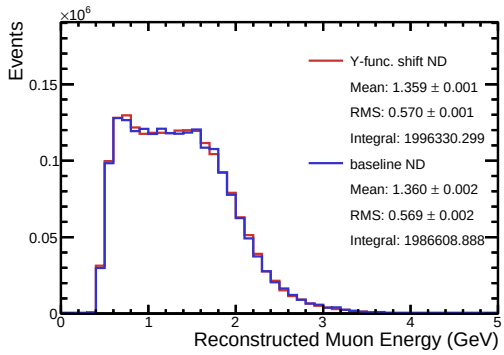

(b) Muon energy

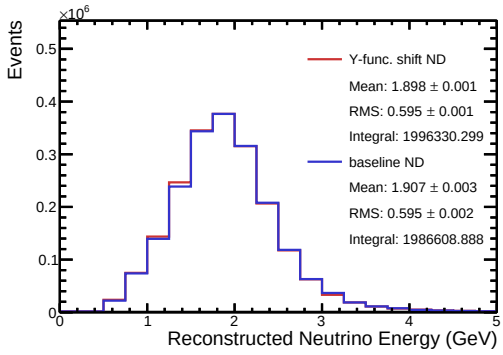

(c) Neutrino energy

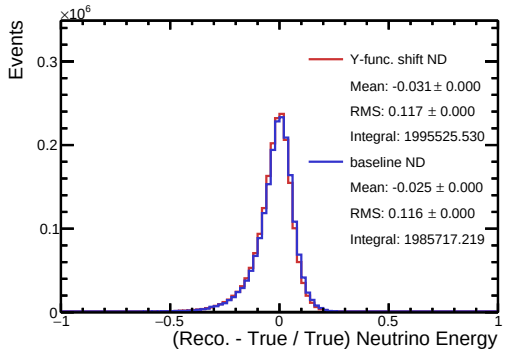

(d) (Reconstructed - true) / true neutrino energy

Figure 4.12: energy distributions for the baseline and y-functional shifted near detector simulation shown by the solid blue and solid red histograms respectively.

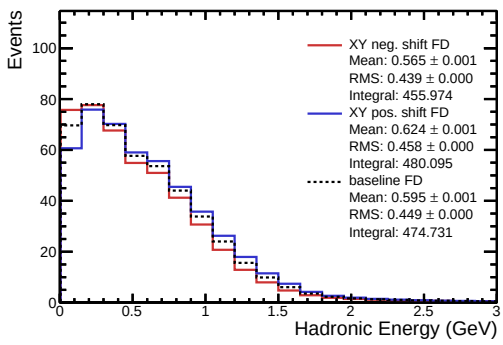

(a) Hadronic energy

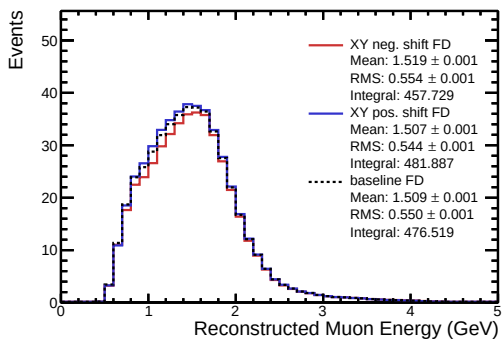

(b) Muon energy

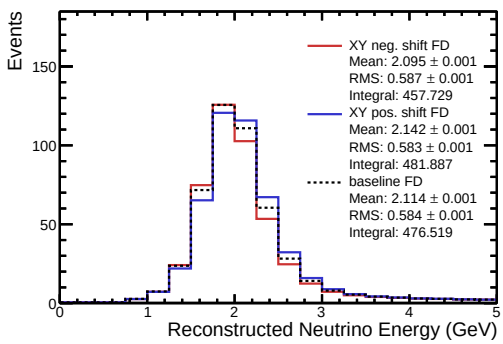

(c) Neutrino energy

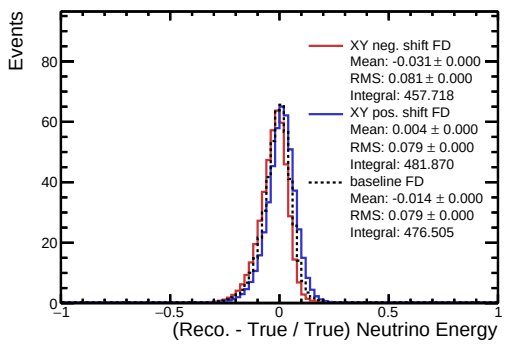

(d) (Reconstructed - true) / true neutrino energy

Figure 4.13: energy distributions for the baseline, xy negatively shifted and xy positively shifted far detector simulation shown by the dotted black, solid red and solid blue histograms respectively.

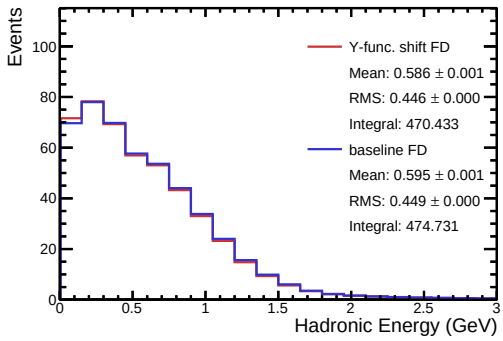

(a) Hadronic energy

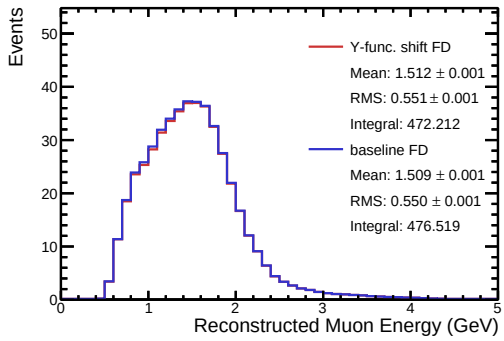

(b) Muon energy

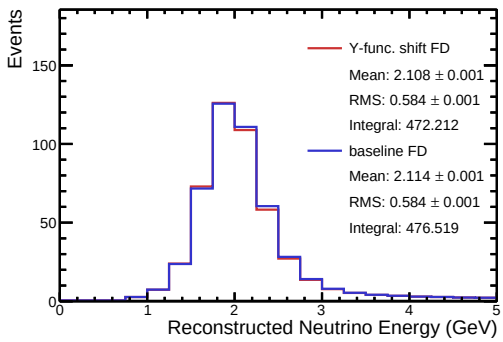

(c) Neutrino energy

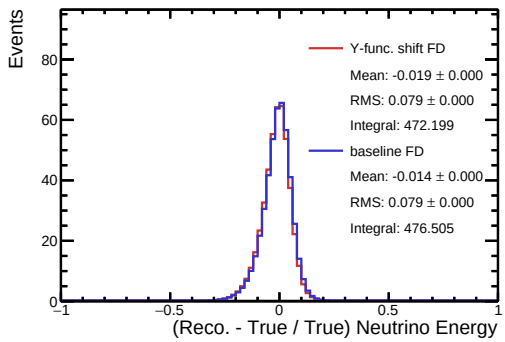

(d) (Reconstructed - true) / true neutrino energy

Figure 4.14: energy distributions for the baseline and y-functional shifted far detector simulation shown by the solid blue and solid red histograms respectively.

$$L \propto \frac{\frac{dE}{dx}}{1 + k_B \frac{dE}{dx} + k_C \left(\frac{dE}{dx}\right)^2}, \tag{4.1}$$

where k_B and k_C are Birks' constant and a higher order correction constant respectively [77].

A fit of Birks' formula to the near detector data defines the constants for the standard NOvA simulation. The fit to the data yielded $k_B = 0.04$ cm / MeV and $k_C = -0.0005$ cm^2/MeV^2 [78]. These values for the constants are not consistent with those often found in the literature and so two systematic samples (called Birks' B and Birks' C) were created with the constants set to alternative values to evaluate the effect of the uncertainty in the Birks parameters on the systematic uncertainty of the analyses.

The Birks' B sample files are created using values commonly found in the literature, $k_B = 0.01$ cm / MeV and $k_C = -0.0$ cm^2/MeV^2. The Birks' C sample files are created using values approximately halfway between the standard NOvA constants and the Birks' B constants, $k_B = 0.02$ cm / MeV and $k_C = -0.0$ cm^2/MeV^2.

Plots of hadronic energy, muon energy, neutrino energy and reconstructed minus true over true energy are shown in Figures 4.15 and 4.16 for the near detector and far detector respectively. For both detectors the shift due to the Birks' B sample is larger than than the shift for the Birks' C sample (see Table 4.1). This is to be expected as the Birks' C constants are halfway between Birks' B and the standard simulation. The shifts found using the Birks' B sample are used to define the systematic uncertainty due to the Birks' parameters for the second analysis.

The study of the shifts in the hadronic, muon and neutrino energy were carried out for the second muon neutrino disappearance analysis [79]. It was found that the Birks' B and C sample files were created without the inclusion of rock muons. Rock muons are muons created by beam muon neutrinos interacting with the rock upstream of the near detector. These rock muons can then travel through the detector where they will generally interact within at least one of the NOvA cells on the outer edge of the detector and fail the containment selection. Comparing the Birks' B and C samples to the nominal simulation (which included rock muons) showed that there were approximately 10% more events per POT (protons on target) in the Birks' B and C samples [79].

A study showed that the difference in events/POT was due to more events in the standard simulation failing containment [80]. The favoured hypothesis for the reduction in events/POT is that events including truly contained interactions are being over-layed

with rock muon energy deposits within the detector which causes the event to fail containment [48]. For the study of the systematic uncertainty due to the Birks' parameters a sample of the standard simulation was created that also neglected to include rock muons.

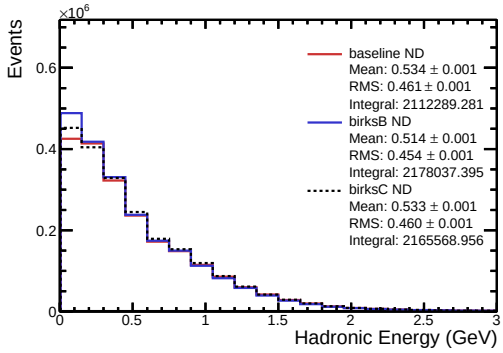

(a) Hadronic energy

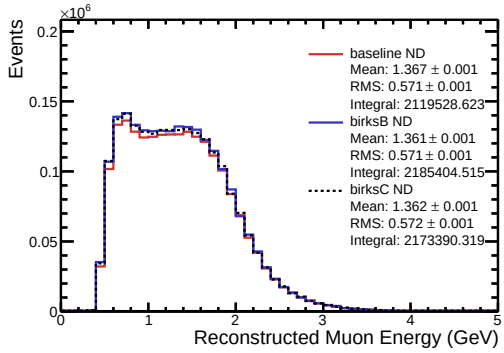

(b) Muon energy

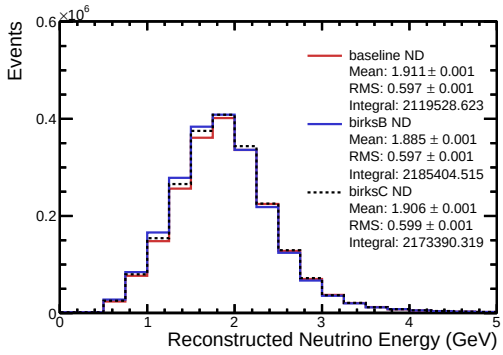

(c) Neutrino energy

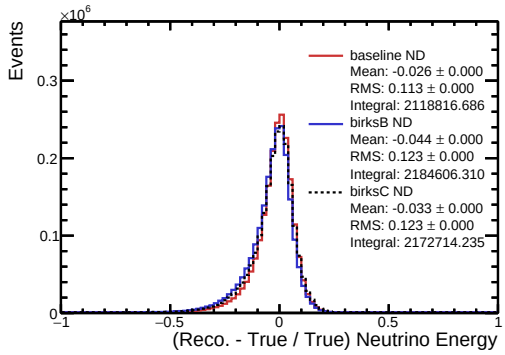

(d) (Reconstructed - true) / true neutrino energy

Figure 4.15: energy distributions for the baseline, Birks' B and Birks C near detector simulation are shown by the solid red, solid blue and dotted black histograms respectively.

4.7.3 Noise

The simulation of electronic noise within the NOvA avalanche photo diodes is described in the the NOvA simulation note [46]. The second disappearance analysis uses the initial noise model (version 1) [48]. A new optimised noise model has since been created (version 2). A sample of files were created with the new noise model and used to approximately measure the systematic uncertainty due to the noise model.

Plots of hadronic energy, muon energy, neutrino energy and reconstructed minus true over true are shown in Figure 4.17. The shifts in mean and normalisation are shown in Table 4.1. The largest shift due to the new noise model is in the mean hadronic energy (+1.3%). The shift in mean neutrino energy and normalisation are small compared to the other systematic samples analysed in this section. [81]

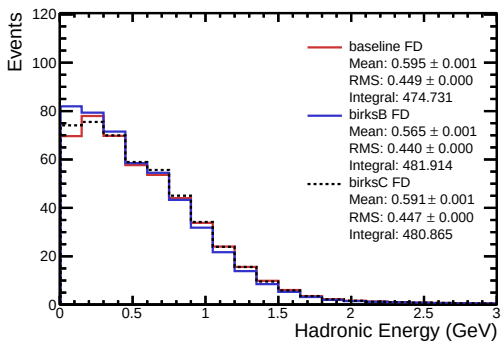

(a) Hadronic energy

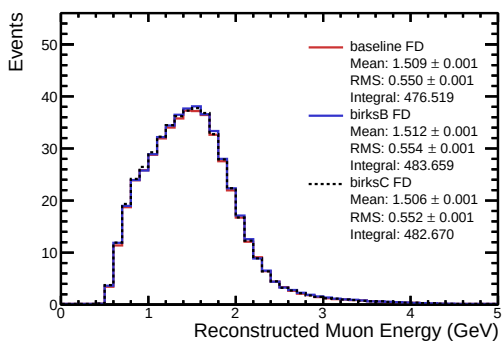

(b) Muon energy

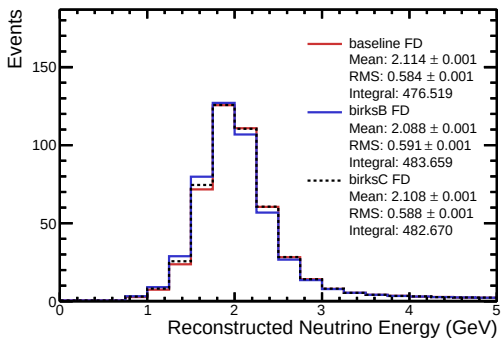

(c) Neutrino energy

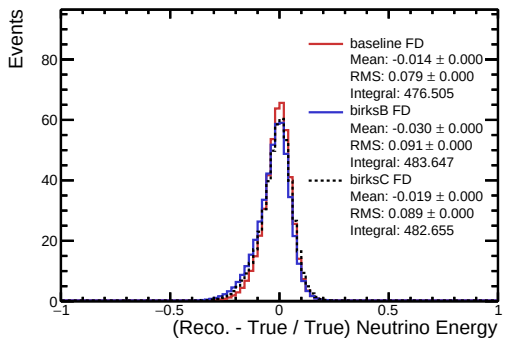

(d) (Reconstructed - true) / true neutrino energy

Figure 4.16: energy distributions for the baseline, Birks' B and Birks C far detector simulation are shown by the solid red, solid blue and dotted black histograms respectively.

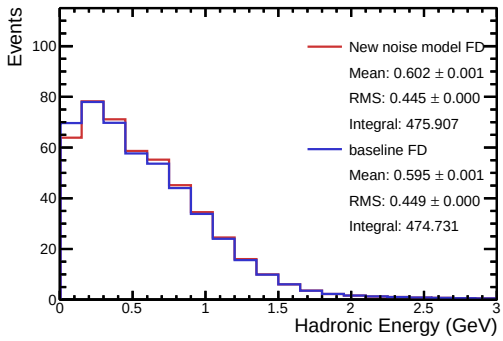

(a) Hadronic energy

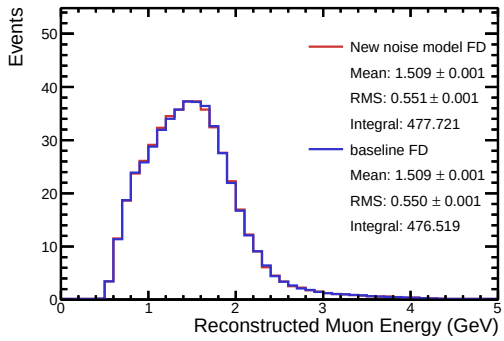

(b) Muon energy

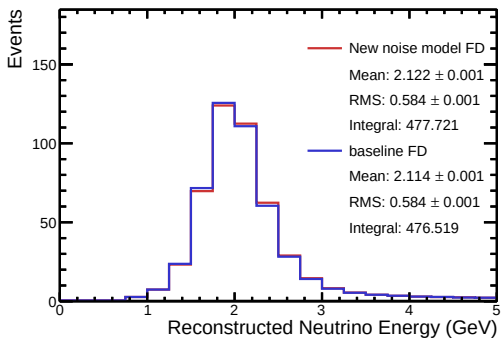

(c) Neutrino energy

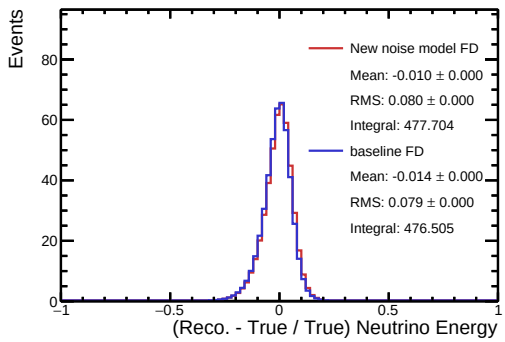

(d) (Reconstructed - true) / true neutrino energy

Figure 4.17: energy distributions for the baseline and new noise model far detector simulation are shown by the solid blue and solid red histograms respectively.

Chapter 5

Analysis Improvements

This Chapter discusses three methods that may improve the sensitivity of the muon neutrino disappearance analysis. The aim of each method is to decrease the size of the sensitivity contour (in the Δm^2 vs. $\sin^2\theta_{23}$ parameter space), if the size of the sensitivity contour is reduced then the oscillation parameters can typically be measured with greater precision.

The first improvement method involves separating neutrino events into bins of energy resolution such that well resolved events are not polluted by the less well resolved sample. In the second method the neutrino energy binning is altered to provide finer binning in the neutrino energy region of maximum oscillation. The third method utilises a hybrid of the ReMId (as used in NOvA's first and second muon neutrino disappearance analyses) and CVN selectors. This chapter consists of three main discussions. First, the individual optimisation of the above methods. Next, the combination of the individually optimised methods. Finally, the combined optimisation of all three methods.

This analysis was performed using NOvA's Common Analysis Format Analysis (CAFAna) software framework which provides a set of classes to enable easy plotting and fitting of oscillated neutrino energy spectra. To speed up analysis everything in CAFAna is histogram based, files are read once to produce the required histograms. All further analysis is done in terms of the histograms [82].

5.1 Best Fit Points

The sensitivity contour is obtained from fitting a simulated far detector spectrum to an oscillated fake data spectrum. The sensitivity of the experiment is tested at different settings for the oscillations applied to the fake data spectrum to sample the sensitivity at

a range of potential neutrino oscillation parameters.

The impact of each method will be measured using three metrics: the sensitivity to reject maximal mixing ($\sin^2\theta_{23} = 0.5$) for the NOvA second analysis ν_μ disappearance best fit, the sensitivity to reject maximal mixing for the most recent MINOS ν_μ disappearance best fit and finally the sensitivity to reject $\sin^2 2\theta_{23} = 0.6$ for the most recent T2K ν_μ disappearance best fit. All best fit points are taken assuming the Normal Ordering hypothesis.

The MINOS best fit is taken from the 2014 combined analysis paper [83]. This paper reported measurements of $|\Delta m^2_{32}| = [2.28 - 2.46] \times 10^{-3}$ eV^2 ($68\% C.L.$) and $\sin^2\theta_{23} =$ 0.35–0.65(90% C.L.). In the following analyses the best fit point used to make the sensitivity contours for comparisons is taken to be $|\Delta m^2_{32}| = 2.36 \times 10^{-3}$ eV^2 and $\sin^2\theta_{23} = 0.41$. The T2K best fit point is extracted from the results of the 2015 paper [84]. The reported measurements are $\sin^2\theta_{23} = 0.528^{+0.055}_{-0.038}$ and $|\Delta m^2_{32}| = (2.51 \pm 0.11) \times 10^{-3}$ eV^2) NOvA's second analysis best fit point, presented in the 2017 disappearance paper [49], is $\sin^2\theta_{23} = 0.404^{+0.030}_{-0.022}$ and $|\Delta m^2_{32}| = (2.67 \pm 0.11) \times 10^{-3}$ eV^2).

5.2 Impact of Cosmic Background on Sensitivity Contours

Figure 5.1 shows the sensitivity of the standard disappearance analysis to the mixing parameters Δm^2_{32} and $\sin^2\theta_{23}$. The sensitivity when accounting for the cosmic background (blue contour) is compared with the sensitivity neglecting the cosmic background (red contour). The contours show that the addition of the cosmic background significantly reduces the sensitivity of the experiment to reject maximal mixing.

The cosmic background will not initially be included for the following studies designed to optimise the sensitivity of the analysis. Instead, the impact of the cosmic background on the sensitivity with all the proposed analysis improvements included will be presented later in the chapter.

5.3 Note On Feldman-Cousins

The Feldman-Cousins correction is used when making the result contours for the official disappearance analysis. A comparison of the second analysis result contour with and without using the Feldman-Cousins technique is shown in Figure 5.2. The contours show that, at the second analysis best fit point, using the Feldman-Cousins technique causes the contours to shrink which enables the oscillation parameters to be measured with greater

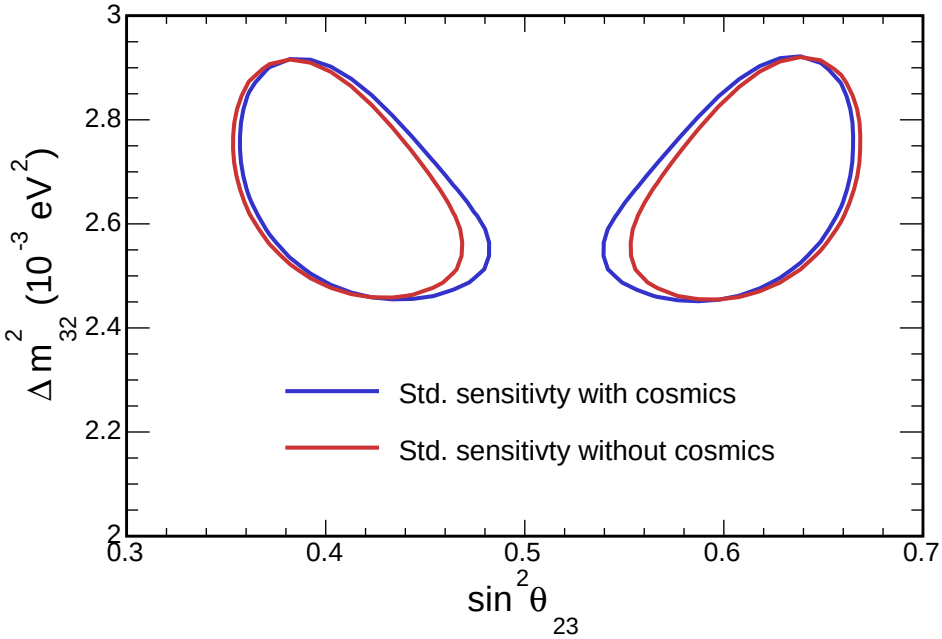

Figure 5.1: Comparison of sensitivity with (blue contour) and without (red contour) accounting for the cosmic background at NOvA's SA best fit point.

precision.

This thesis focuses on potential improvements to the muon neutrino disappearance analysis. At the current best fit point Figure 5.2 shows that the introduction of Feldman-Cousins only increases the sensitivity. For the rest of this thesis the Feldman-Cousins technique will not be implemented.

5.4 Hadronic Energy Fraction Binning

The first sensitivity improvement considered is to separate events by reconstructed neutrino energy resolution. Events with better energy resolution are less likely to migrate across neutrino energy bin boundaries. This is particularly important to the result of the analysis for events near the oscillation dip, events migrating into or out of the oscillation dip will alter the final measurement. The reconstructed neutrino energy is the sum of the reconstructed muon energy and the reconstructed hadronic shower energy. In the NOvA detectors, muon energy is estimated using the length of the muon track with a resolution of 2% while hadronic energy is estimated from the calorimetric response of the detector to a cluster of cell-hits with a resolution of about 25% [49]. Therefore, neutrino events with a larger proportion of hadronic activity will be less well resolved by the detector.

In the following Section hadronic energy fraction, $E_{had.}/E_{\nu}$, is used as a metric to

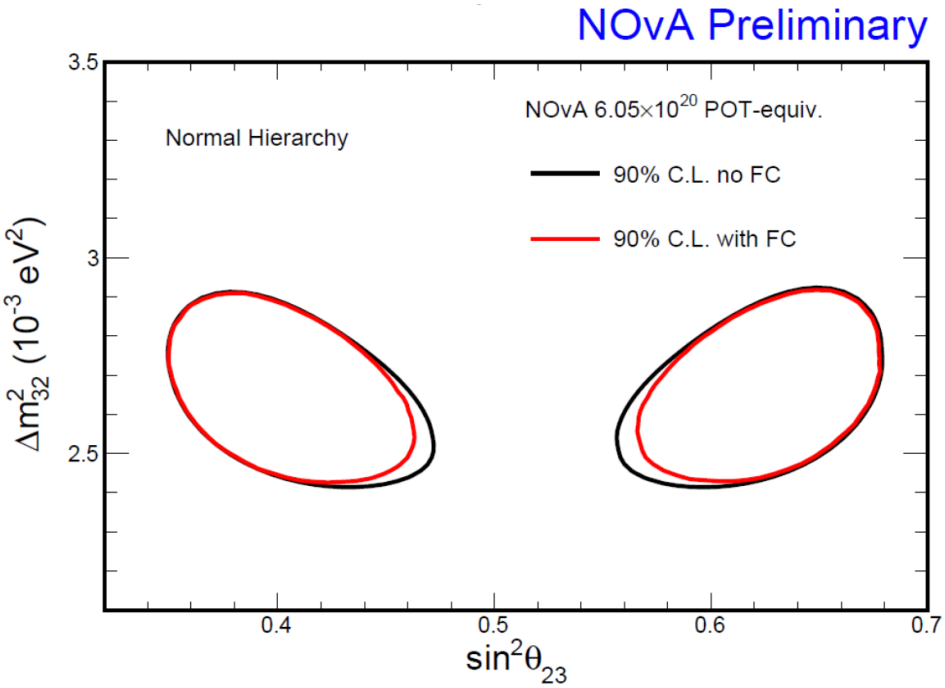

Figure 5.2: Comparison of the second analysis result contour with (black line) and without (red line) using the Feldman Cousins corrections. Taken from [85].

estimate the neutrino energy resolution. The $E_{had.}/E_{\nu}$ distribution is obtained for each bin of reconstructed neutrino energy and the quantiles of $E_{had.}/E_{\nu}$ are identified. These quantiles are then used as the boundaries of the $E_{had.}/E_{\nu}$ bins. In this analysis the number of $E_{had.}/E_{\nu}$ bins can be varied to optimise the sensitivity. Figures 5.3, 5.4, 5.5 and 5.6 show the distribution of hadronic energy fraction vs. reconstructed neutrino energy for each far detector running period used in this analysis. The quantile boundaries are formed on a period by period basis to incorporate any changes in the detector performance such as the introduction of a higher APD gain in the far detector since the 2015 summer shutdown (period 3). To provide an example, the quantile boundaries for a division into four hadronic energy fraction quantiles are shown by the black histograms overlaid on the colour plot. In this case, with four $E_{had.}/E_{\nu}$ bins, the lowest $E_{had.}/E_{\nu}$ quantile contains the 25% of the sample with the best neutrino energy resolution. On the other hand, the highest quantile contains the 25% of the sample with the worst neutrino energy resolution.

The sensitivity contours for scenarios where the far detector neutrino energy spectrum is split into 2, 3, 4, 5, 6, 7 and 8 quantiles of $E_{had.}/E_{\nu}$ are compared with the standard analysis at NOvA's second analysis best fit point in Figure 5.7, at MINOS's best fit point in Figure 5.9 and at T2K's latest best fit point in Figure 5.11. In addition, the significance of rejection of a point in oscillation parameter space (maximal mixing for the NOvA and

MINOS best fit and $\sin^2\theta_{23} = 0.6$ for the T2K best fit) is plotted against the number of $E_{had.}/E_\nu$ quantiles for the NOvA, MINOS and T2K best fit points in Figures 5.14, 5.18 and 5.16 respectively.

Both the improvement to the sensitivity and the increase in the memory footprint due to making the fit must be considered when deciding upon the number of $E_{had.}/E_\nu$ quantiles used for the analysis of the data. With each additional $E_{had.}/E_\nu$ bin the memory and time needed to produce the fit almost doubles. The largest gain in sensitivity at all three best-fit points comes from the initial introduction of splitting events into two $E_{had.}/E_\nu$ quantiles. Further improvements are seen when using three and four quantiles. After four quantiles the improvement seen with each additional $E_{had.}/E_\nu$ is substantially reduced. Considering both the improvements in sensitivity and also the increase in memory use the division of neutrino events into 4 quantiles of $E_{had.}/E_\nu$ is chosen.

The above described method involves separating events by $E_{had.}/E_\nu$. It is important that events are able to migrate across $E_{had.}/E_\nu$ bins if an appropriate systematic shift is applied. Without this ability, events will be artificially constrained to particular $E_{had.}/E_\nu$ bins and systematic shifts will be over constrained. A study [86] showed that events can migrate from one $E_{had.}/E_\nu$ bin to another when a systematic shift is applied to the hadronic energy.

5.5 Optimising Neutrino Energy Binning

The neutrino energy binning used for the muon neutrino disappearance analysis presented in the first and second papers consists of 0.25 GeV width bins from 0 to 5 GeV. Most of the neutrino oscillation information is gained between 1 and 3 GeV, in particular between 1 and 2 GeV. If it is wider than the neutrino energy resolution, the coarser binning may conceal information useful in distinguishing between predictions made with different sets of oscillation parameters [87]. Therefore, using finer binning could enhance the sensitivity of the disappearance analysis. The advantages of finer binning will diminish as the bin size approaches and goes beyond the neutrino energy resolution. Another point to consider when adjusting the neutrino energy binning is that the number of neutrino energy bins almost proportionally impacts the memory required for the fit. For this reason, the strategies presented below focus on increasing the number of bins in the region of maximum oscillation between 1 and 3 GeV.

To investigate possible enhancements to the sensitivity, three alternative neutrino energy binning strategies are compared with the standard analysis neutrino energy binning.

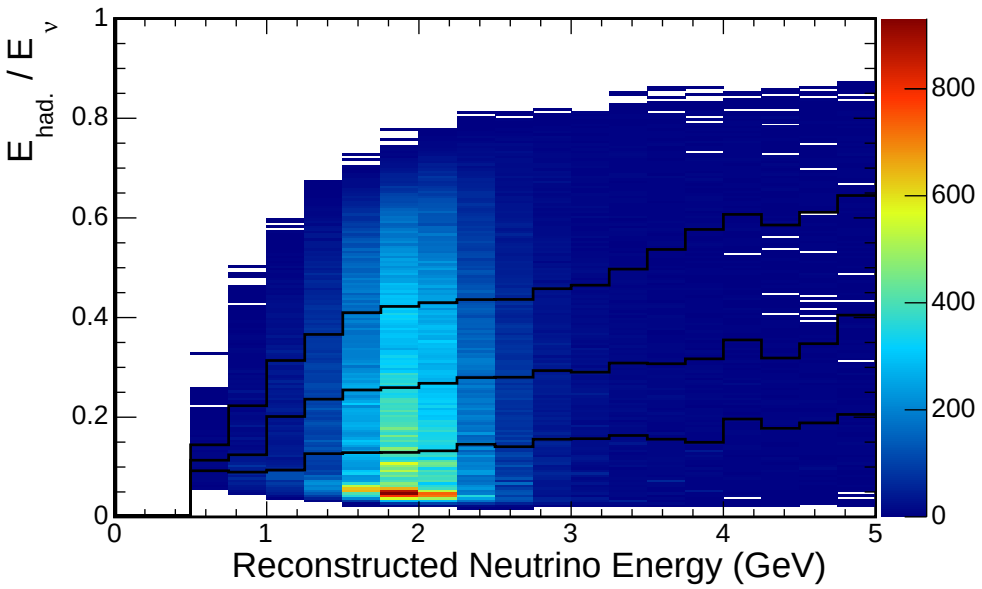

Figure 5.3: Hadronic energy fraction vs. reconstructed neutrino energy in the far detector MC during running period 1. The quantile boundaries are shown for each neutrino energy bin for the choice of 4 hadronic energy fraction bins.

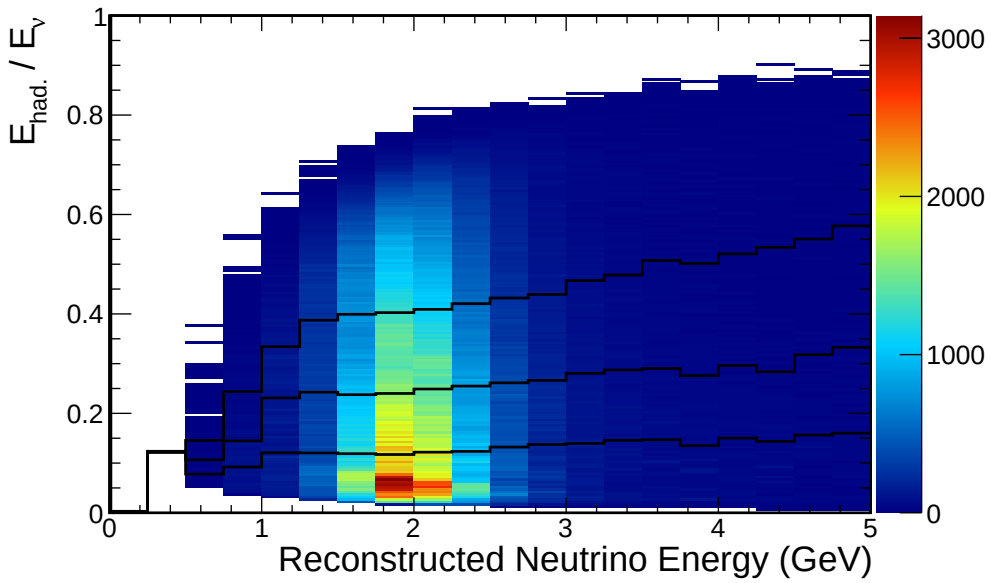

Figure 5.4: Hadronic energy fraction vs. reconstructed neutrino energy in the far detector MC during running period 2. The quantile boundaries are shown for each neutrino energy bin for the choice of 4 hadronic energy fraction bins.

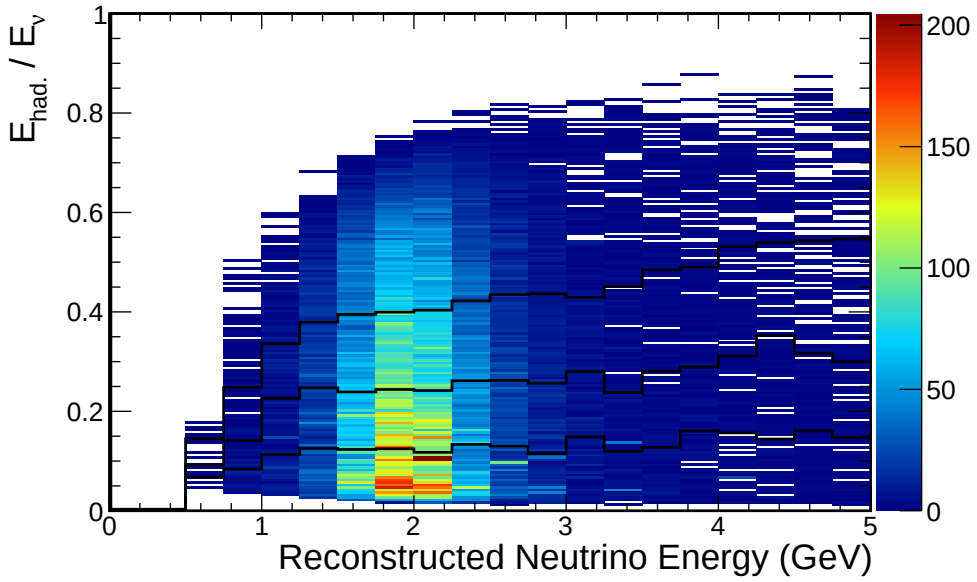

Figure 5.5: Hadronic energy fraction vs. reconstructed neutrino energy in the far detector MC during running epoch 3b. The quantile boundaries are shown for each neutrino energy bin for the choice of 4 hadronic energy fraction bins.

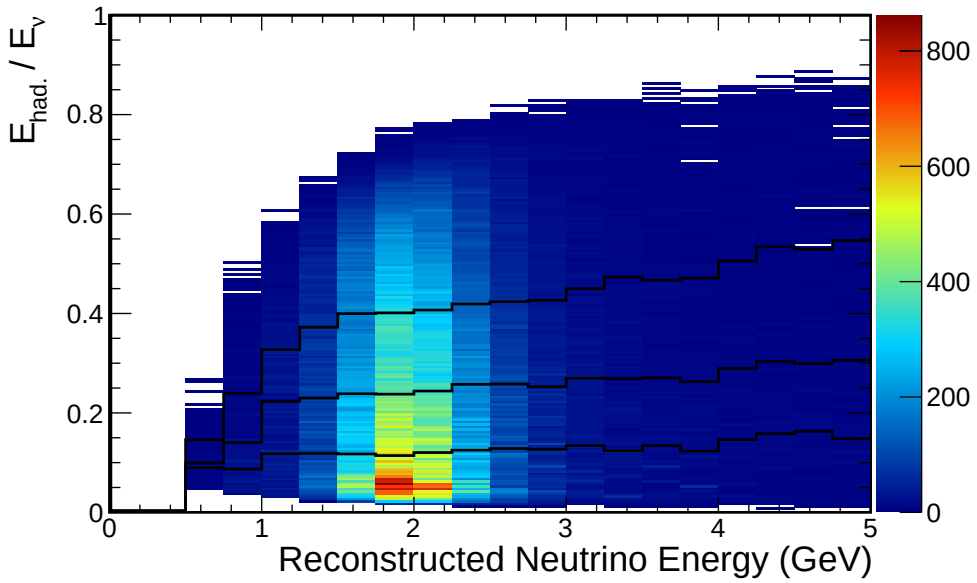

Figure 5.6: Hadronic energy fraction vs. reconstructed neutrino energy in the far detector MC during running epoch 3c. The quantile boundaries are shown for each neutrino energy bin for the choice of 4 hadronic energy fraction bins.

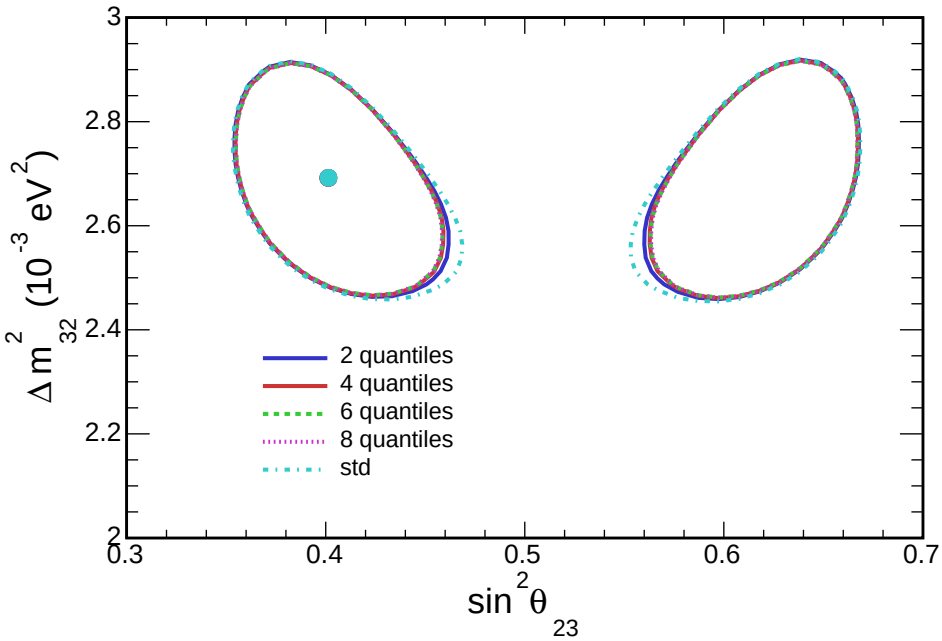

Figure 5.7: Sensitivity contours for the ν_μ disappearance analysis at NOvA's second analysis best-fit. The sensitivity of the standard analysis is shown by the dotted light-blue contour. A set of analysis where the events are split 2, 4, 6 and 8 quantiles of $E_{had.}/E_\nu$ are shown by the solid blue, solid red, dashed green and dotted purple contours respectively.

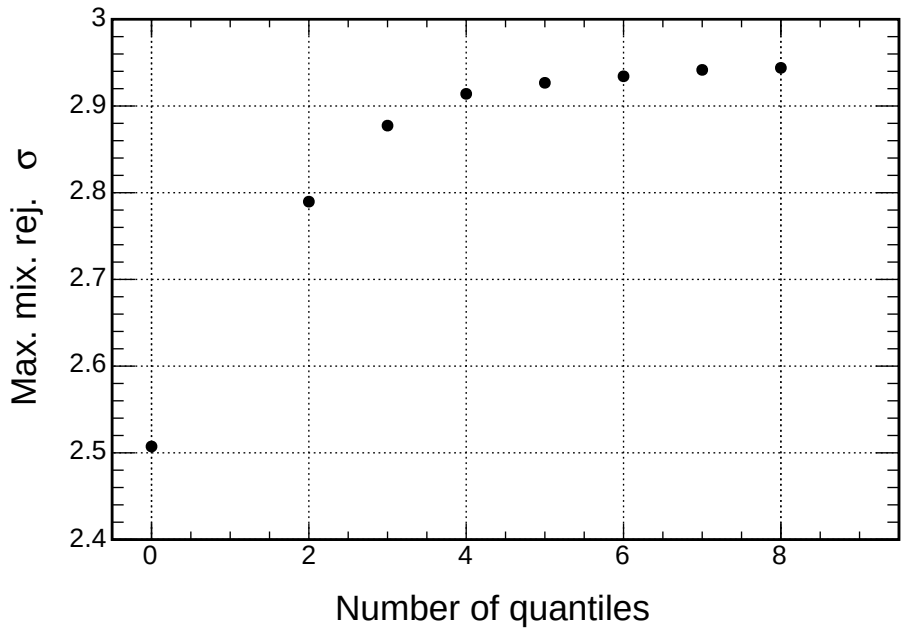

Figure 5.8: Significance of maximal mixing ($\sin^2\theta_{23} = 0.5$) rejection vs. the number of $E_{had.}/E_\nu$ quantiles used in the analysis. The standard sensitivity, where the events are not divided into quantiles of $E_{had.}/E_\nu$, is shown by the point where quantiles = 0.

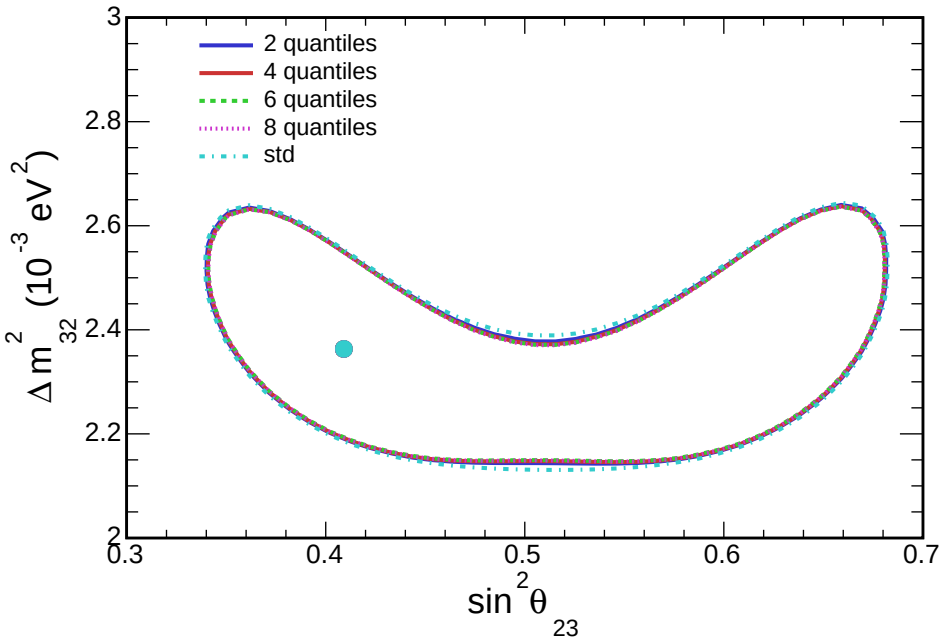

Figure 5.9: Sensitivity contours for the ν_μ disappearance analysis at MINOS's latest best-fit. The sensitivity of the standard analysis is shown by the dotted light-blue contour. A set of analysis where the events are split 2, 4, 6 and 8 quantiles of $E_{had.}/E_\nu$ are shown by the solid blue, solid red, dashed green and dotted purple contours respectively.

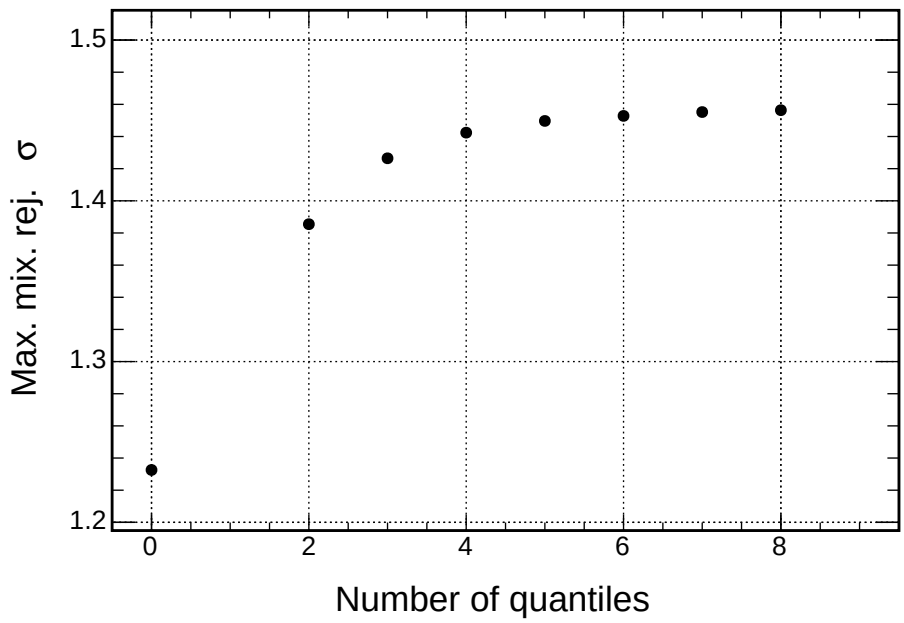

Figure 5.10: Significance of maximal mixing ($\sin^2\theta_{23} = 0.5$) rejection vs. the number of $E_{had.}/E_\nu$ quantiles used in the analysis. The standard sensitivity, where the events are not divided into quantiles of $E_{had.}/E_\nu$, is shown by the point where quantiles = 0.

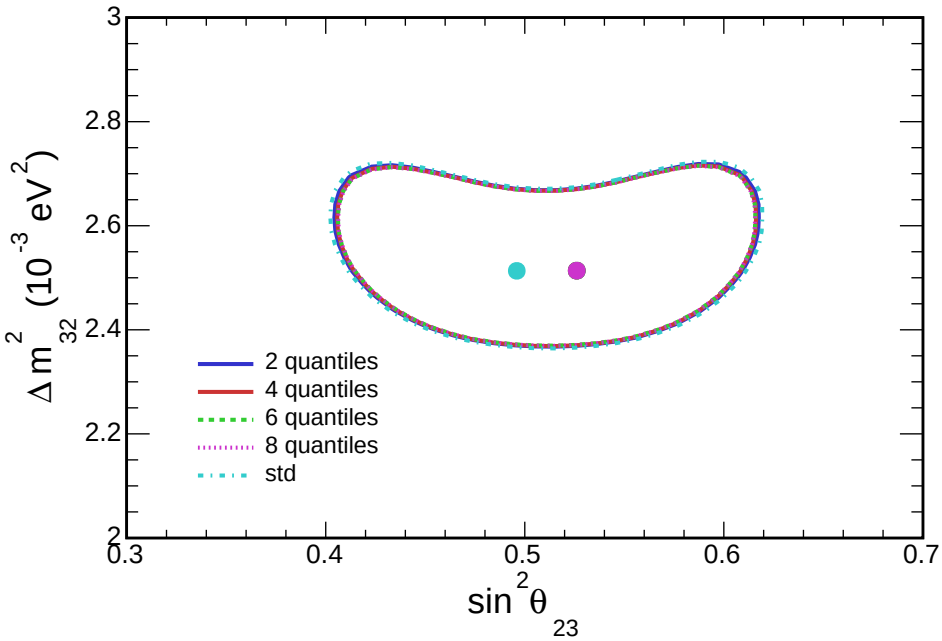

Figure 5.11: Sensitivity contours for the ν_μ disappearance analysis at T2K's latest best-fit. The sensitivity of the standard analysis is shown by the dotted light-blue contour. A set of analysis where the events are split 2, 4, 6 and 8 quantiles of $E_{had.}/E_\nu$ are shown by the solid blue, solid red, dashed green and dotted purple contours respectively.

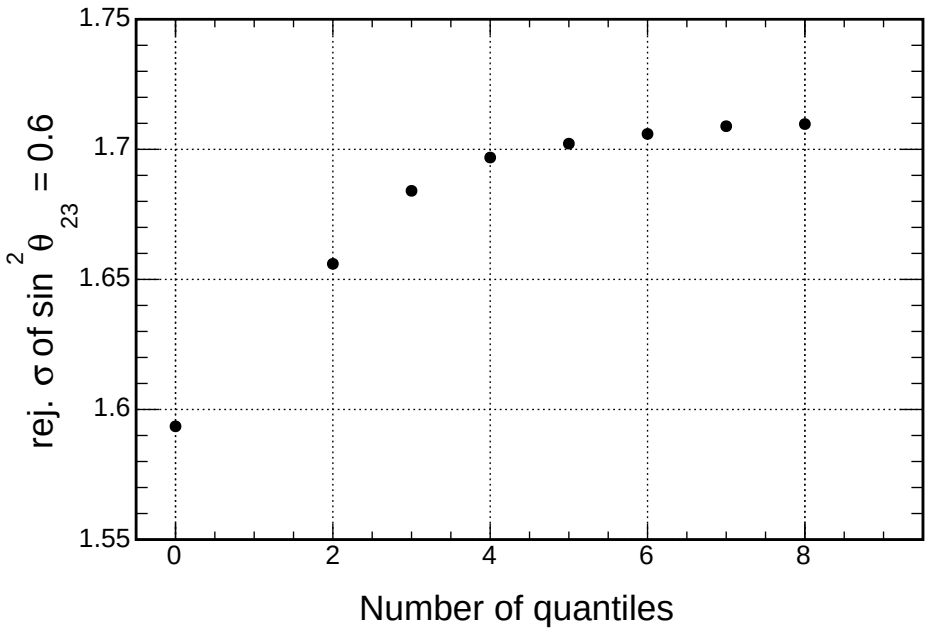

Figure 5.12: Significance of rejecting ($\sin^2\theta_{23} = 0.6$) vs. the number of $E_{had.}/E_\nu$ quantiles used in the analysis. The standard sensitivity where the events are not divided into quantiles is shown by the point where quantiles = 0.

An overview of the standard binning and the three alternative binning strategies is presented in Table 5.1. The table shows the general idea of the new binning strategies (scheme "A", "B" and "C") where finer bins are used in the region of maximum oscillation (1-2 GeV) and coarser bins are used in the region where there is less oscillation information (0-1 GeV and 3-5 GeV). As shown in the table, the new binning strategies share a common binning between 0 and 1 GeV of two bins, one from 0 to 0.75 GeV and the other from 0.75 to 1 GeV. They also share a common binning between 3 and 5 GeV, consisting of two 0.5 GeV bins from 3 to 4 GeV and a single 1 GeV bin from 4 to 5 GeV. The differences between the binning strategies occur between 1 and 3 GeV. Binning scheme "A" implements 80 0.025 GeV bins between 1 and 3 GeV. Binning scheme "B" implements 40 0.025 GeV bins between 1 and 2 GeV and 4 0.25 GeV between 2 and 3 GeV. Finally, binning scheme "C" implements 10 0.1 GeV bins between 1 and 2 GeV and 4 0.25 GeV between 2 and 3 GeV. Note that binning scheme "C" requires less bins in total than the standard binning whilst using finer binning in the region of interest.

Comparisons of the four binning strategies in terms of sensitivity to Δm^2_{32} and $\sin^2 2\theta_{23}$ and rejection of maximal mixing are shown for the NOvA, T2K and MINOS best fit points in Figures 5.13, 5.14, 5.15, 5.16, 5.17 and 5.18 respectively. The figures show that the sensitivity to reject maximal mixing increases when increasing the number of neutrino energy bins (going from std. through to "A" binning) for all three best fit points. The largest increase in the sensitivity to reject maximal mixing comes when going from the standard binning to the "C" binning. Increasing the number of bins by going from "C" to "B" binning shows a modest improvement but requires more than double the number of neutrino energy bins. Further, binning strategy "A" shows only marginal improvement over binning strategy "B" whilst almost doubling the number of neutrino energy bins again. Binning strategy "C" is chosen over the other strategies as it shows a significant improvement in sensitivity (only marginally beaten by "A" and "B") whilst reducing the number of neutrino energy bins compared to the standard binning.

5.6 Hybrid Selection Combining ReMId and CVN

The muon neutrino selection algorithms, CVN and ReMId, (see Section 4.2) may be used in unison to improve the sensitivity to muon neutrino disappearance. Currently the hybrid selection only selects events that have CVN$>$ 0.5 and ReMID$>$ 0.5. When reducing the cut threshold of either remid or CVN the neutral current background events will increase along with the signal.

	Neutrino Energy Binning Scheme			
Neutrino Energy Range (GeV)	Std.	scheme A	scheme B	scheme C
0 - 0.75	3	1	1	1
0.75 - 1	1	1	1	1
1 - 2	4	40	40	10
2 - 3	4	40	4	4
3 - 4	4	2	2	2
4 - 5	4	1	1	1
0 - 5	20	85	49	19

Table 5.1: The number of neutrino energy bins per energy range for each neutrino energy binning scheme. The total number of neutrino energy bins for each scheme is shown in the last row.

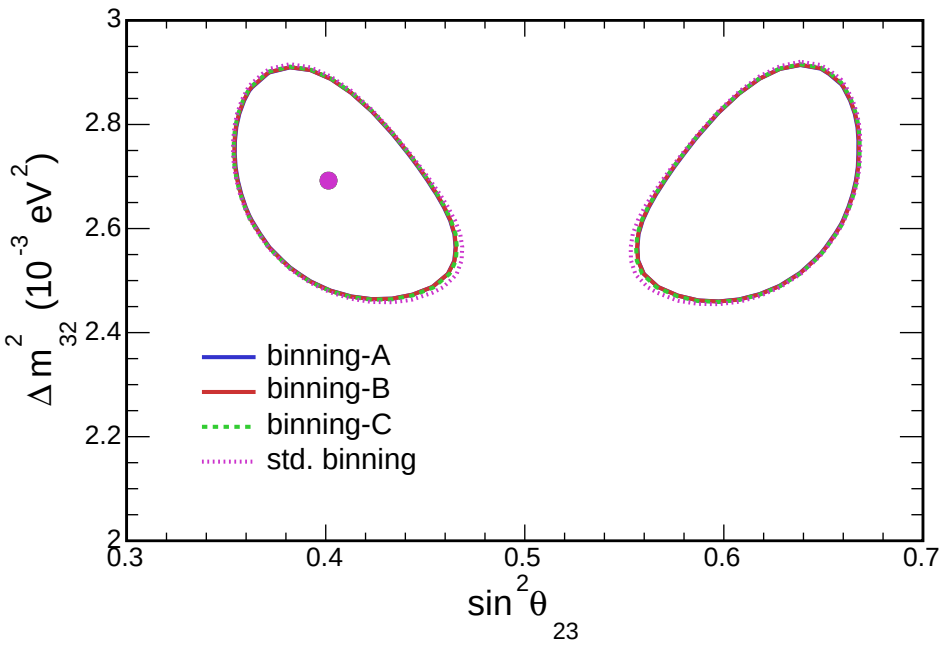

Figure 5.13: Sensitivity contours for the ν_μ disappearance analysis at NOvA's second analysis best-fit. The sensitivity of the standard analysis is shown by the dotted pink contour. A set of analysis where the the neutrino energy is binned according to scheme's A, B or C (see Table 5.1) are shown by the sold blue, solid red and dotted green contours respectively.

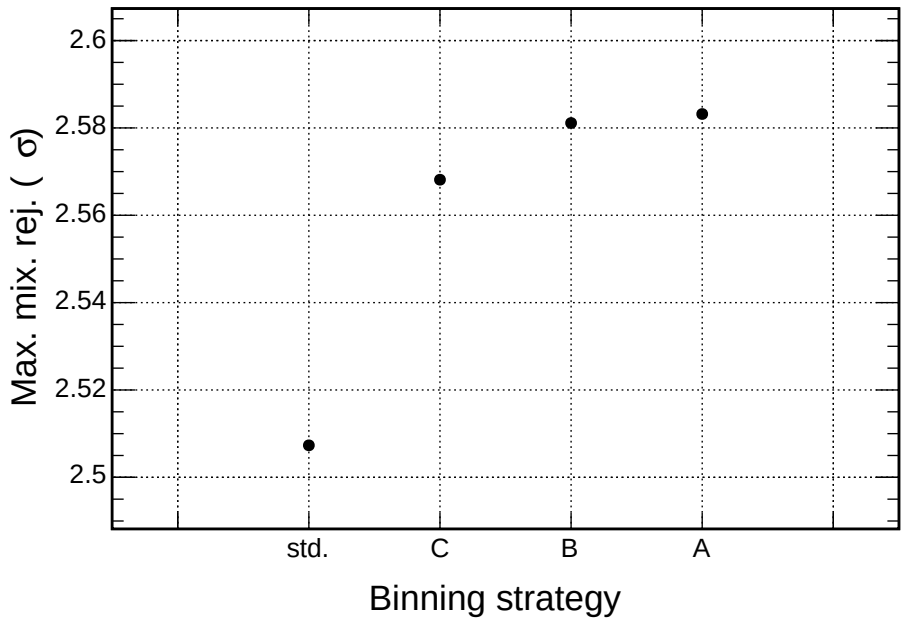

Figure 5.14: Significance of maximal mixing ($\sin^2\theta_{23} = 0.5$) rejection vs. the neutrino energy binning strategy used in the analysis. A breakdown of the each neutrino energy binning scheme is shown in Table 5.1.

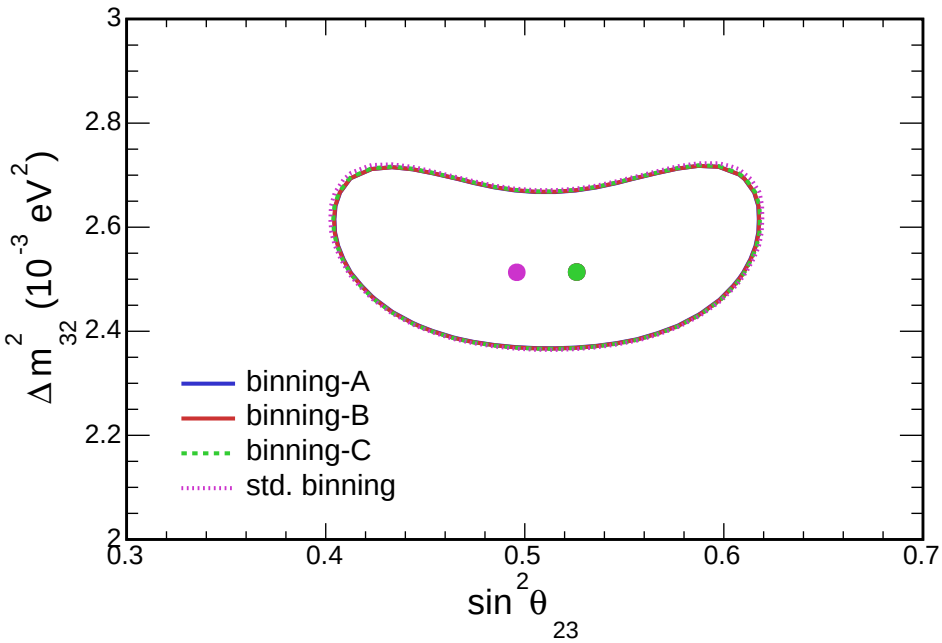

Figure 5.15: Sensitivity contours for the ν_μ disappearance analysis at T2K's latest best-fit. The sensitivity of the standard analysis is shown by the dotted pink contour. A set of analysis where the the neutrino energy is binned according to scheme's A, B or C (see Table 5.1) are shown by the sold blue, solid red and dotted green contours respectively.

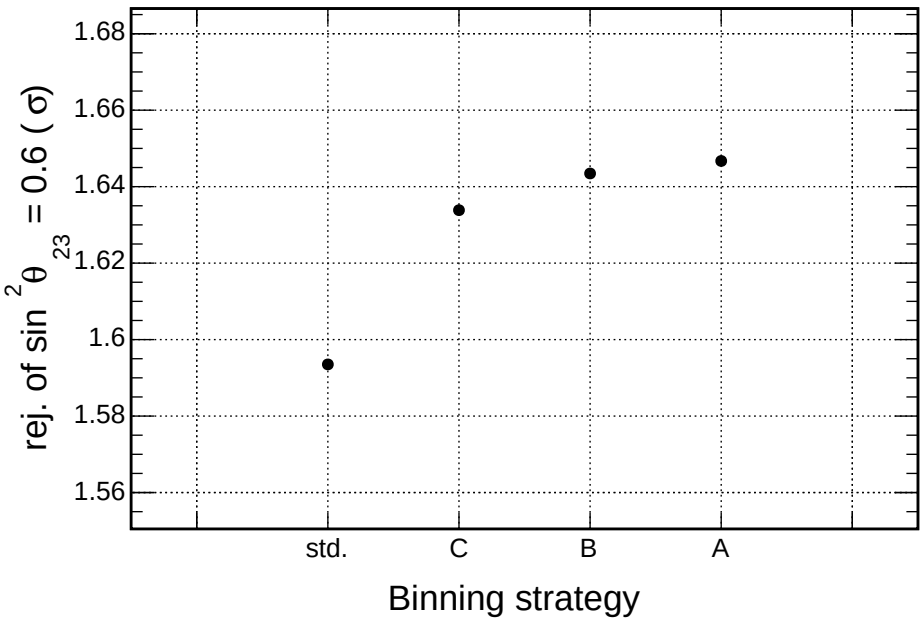

Figure 5.16: Significance of rejecting ($\sin^2\theta_{23} = 0.6$) vs. the neutrino energy binning strategy used in the analysis. A breakdown of the each neutrino energy binning scheme is shown in Table 5.1.

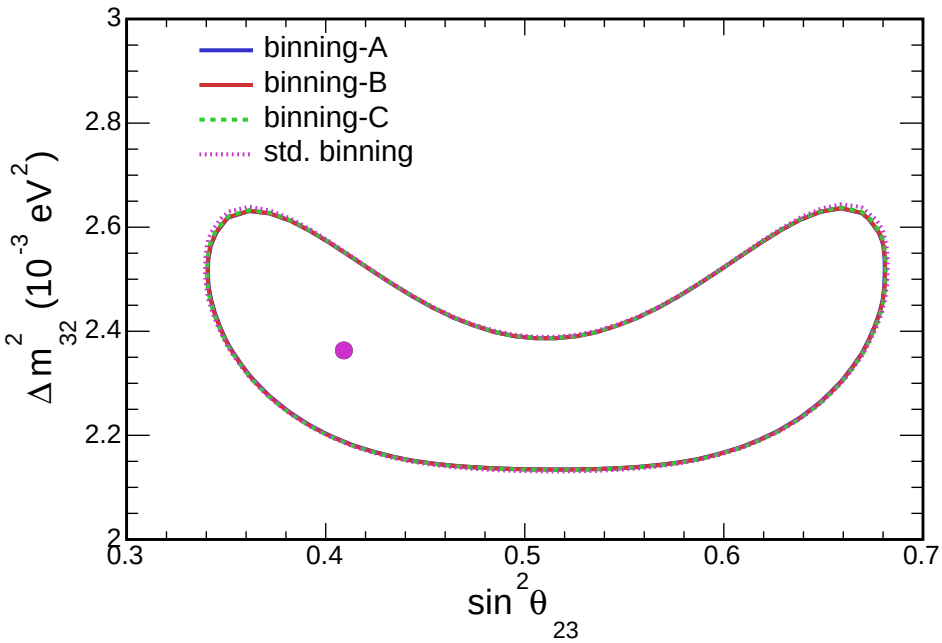

Figure 5.17: Sensitivity contours for the ν_μ disappearance analysis at MINOS's latest best-fit. The sensitivity of the standard analysis is shown by the dotted pink contour. A set of analysis where the the neutrino energy is binned according to scheme's A, B or C (see Table 5.1) are shown by the sold blue, solid red and dotted green contours respectively.

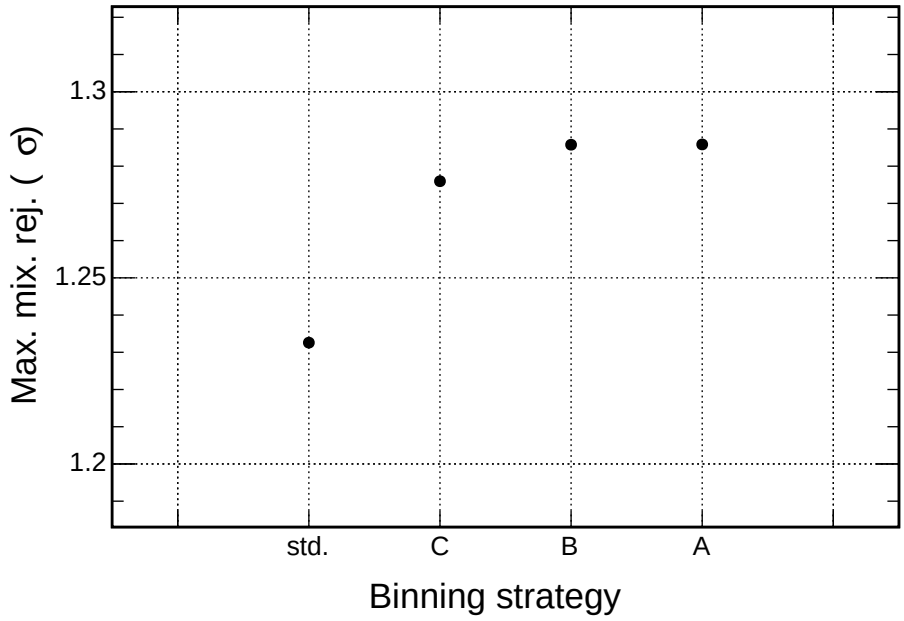

Figure 5.18: Significance of maximal mixing ($\sin^2\theta_{23} = 0.5$) rejection vs. the neutrino energy binning strategy used in the analysis. A breakdown of the each neutrino energy binning scheme is shown in Table 5.1.

Figures 5.19, 5.20 and 5.21 show a comparison of the sensitivity using the standard selection and using the hybrid selection the NOvA, MINOS and T2K best fit points respectively. The hybrid sensitivity contour is created with the standard analysis (standard neutrino energy binning and no quantiles of $E_{had.}/E_\nu$) except for using the hybrid selection requiring CVN > 0.5 and ReMID > 0.5.

The three sensitivity contours (Figures 5.19, 5.20 and 5.21) show that at all three best fit points the sensitivity is improved with the introduction of the hybrid selection. In particular the sensitivity at NOvA's second analysis best fit point is improved, the sensitivity to reject maximal mixing increases from 2.5 σ to 3.0 σ. Due to improving the sensitivity the hybrid selection will be used for the final analysis.

A study to optimise the hybrid selection was carried out and found that the size of the sensitivity contour and ability to reject maximal mixing was relatively flat across the ReMId vs. CVN parameter space [88]. There was a slight improvement when loosening both the ReMId and CVN cut level. However, the study did not account for cosmics which would reduce the sensitivity particularly for low values of ReMId and CVN. The decision for this thesis is to leave the hybrid selection at the standard setting as there is not much sensitivity to gain even when not accounting for the cosmic background.

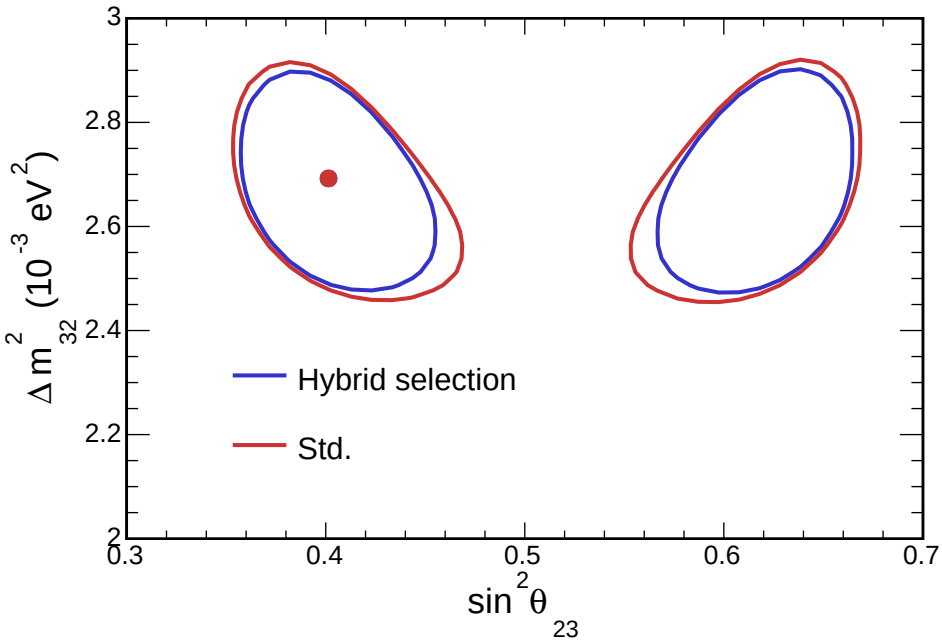

Figure 5.19: Sensitivity contours for the ν_μ disappearance analysis at NOvA's latest best-fit. The sensitivity of the standard analysis and an analysis using the hybrid selection are shown by the red and blue contours respectively. The rejection of maximal mixing increases from 2.5 σ to 3.0 σ when using the hybrid selection.

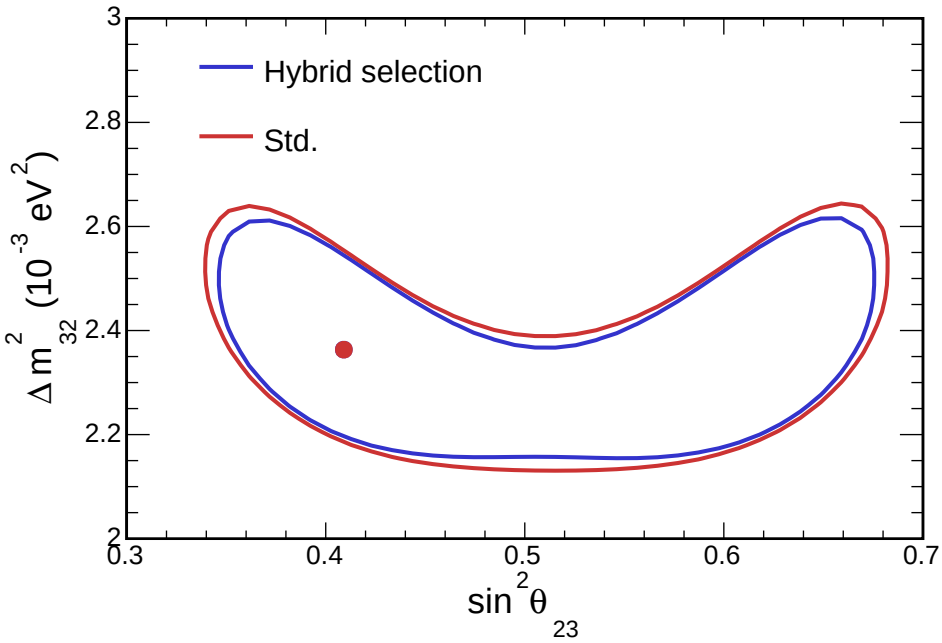

Figure 5.20: Sensitivity contours for the ν_μ disappearance analysis at MINOS's latest best-fit. The sensitivity of the standard analysis and an analysis using the hybrid selection are shown by the red and blue contours respectively. The rejection of maximal mixing increases from 1.2 σ to 1.5 σ when using the hybrid selection.

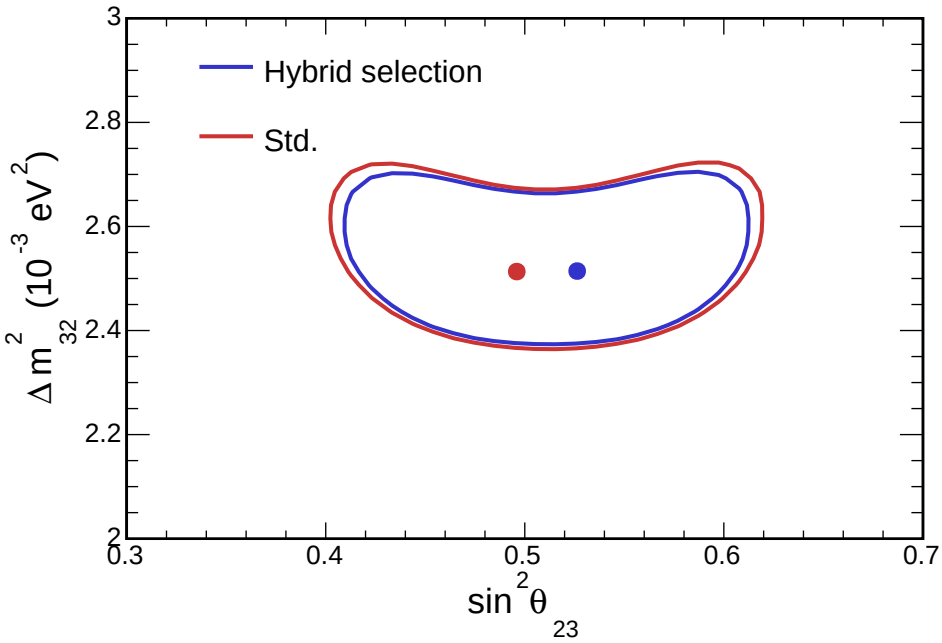

Figure 5.21: Sensitivity contours for the ν_μ disappearance analysis at T2K's latest best-fit. The sensitivity of the standard analysis and an analysis using the hybrid selection are shown by the red and blue contours respectively. The rejection of the point $\sin^2\theta_{23} = 0.6$ increases from 1.6 σ to 1.8 σ when using the hybrid selection.

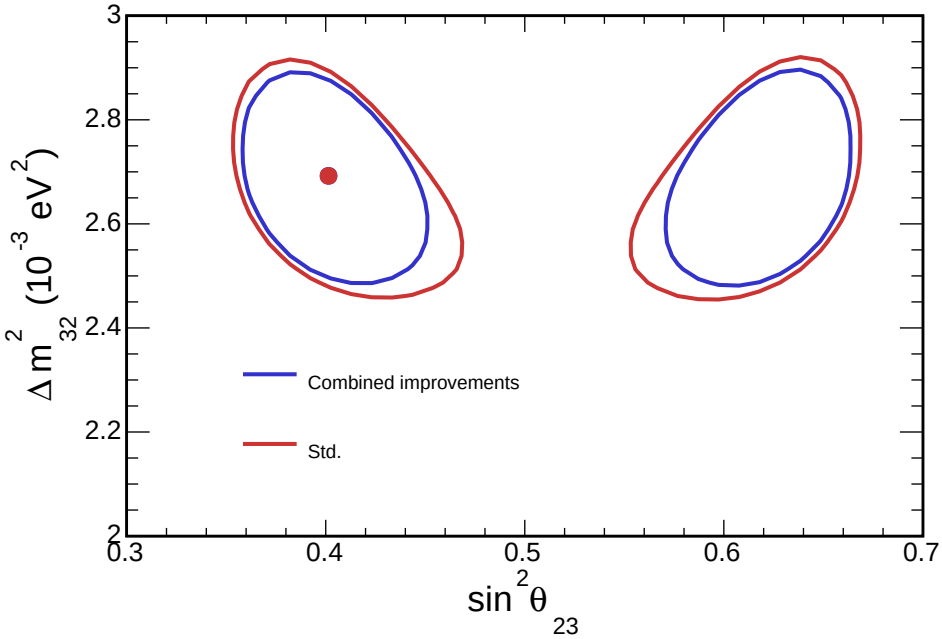

Figure 5.22: Sensitivity contours for the ν_μ disappearance analysis at NOvA's latest best-fit. The sensitivity of the standard analysis and an analysis using the individually optimised sensitivity improvements (with 4 $E_{had.}/E_\nu$ quantiles, neutrino energy binning scheme "C" and the hybrid selection) are shown by the red and blue contours respectively. The rejection of maximal mixing increases from 2.5 σ to 3.3 σ when using all three analysis improvements together.

5.7 All Analysis Improvements Combined

This section discusses the improvement to the sensitivity when the individually optimised analysis improvements discussed in Sections 5.4, 5.5 and 5.6 are combined. In particular, the combination uses the individually optimised settings for each improvement with 4 $E_{had.}/E_\nu$ quantiles, binning scheme "C" and the default ReMId-CVN hybrid selection.

Show comparison of the the standard sensitivity and the all improvements sensitivity (at the individually optimised level: 4 hadEFrac, binning C and hybrid selection).

Figures 5.22, 5.23 and 5.24 show the sensitivity when using all the analysis improvements in combination at the NOvA, MINOS and T2K best-fit points respectively. The sensitivity at each best fit point is significantly improved with the introduction of the analysis improvements.

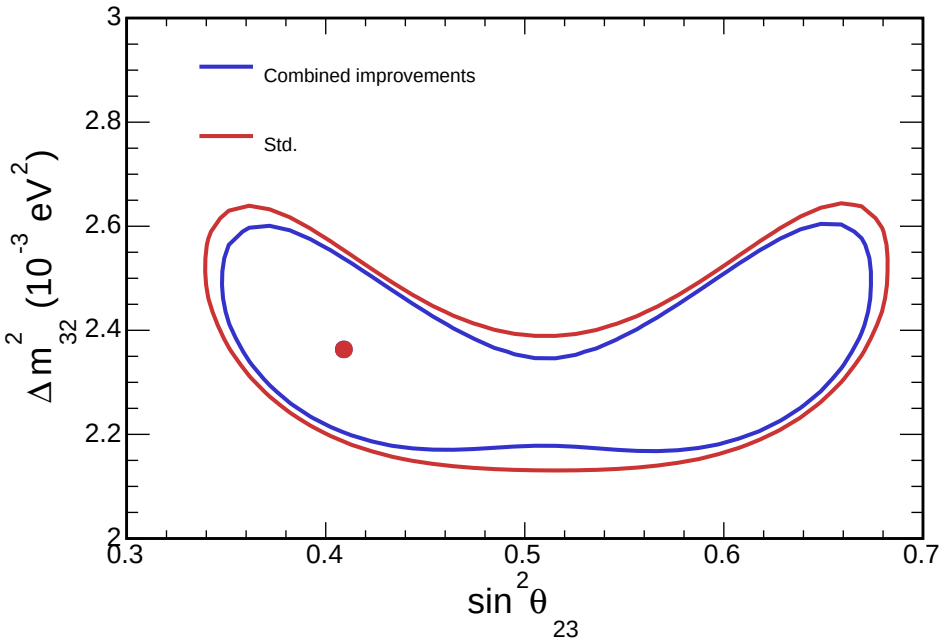

Figure 5.23: Sensitivity contours for the ν_μ disappearance analysis at MINOS's latest best-fit. The sensitivity of the standard analysis and an analysis using the individually optimised sensitivity improvements (with 4 $E_{had.}/E_\nu$ quantiles, neutrino energy binning scheme "C" and the hybrid selection) are shown by the red and blue contours respectively. The rejection of maximal mixing increases from 1.2 σ to 1.7 σ when using all three analysis improvements together.

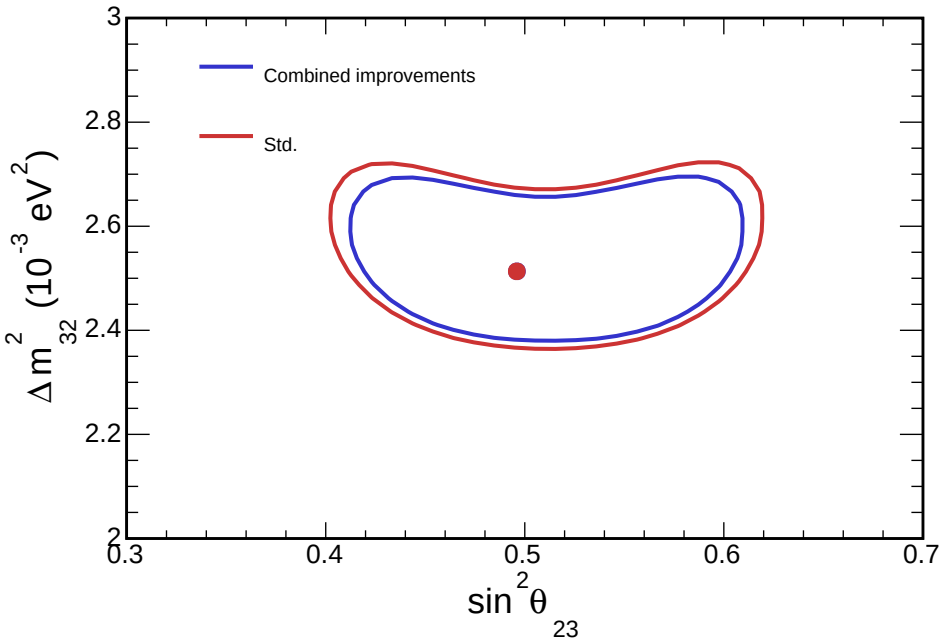

Figure 5.24: Sensitivity contours for the ν_μ disappearance analysis at T2K's latest best-fit. The sensitivity of the standard analysis and an analysis using the individually optimised sensitivity improvements (with 4 $E_{had.}/E_\nu$ quantiles, neutrino energy binning scheme "C" and the hybrid selection) are shown by the red and blue contours respectively. The rejection of the point $\sin^2\theta_{23} = 0.6$ increases from 1.6 σ to 1.9 σ when using all three analysis improvements together.

5.8 Combined Optimisation of Analysis Improvements

Then respin number of HadEFrac. bins again w/ energy bins.

This section discusses an iterative approach to optimising the number of $E_{had.}/E_{\nu}$ quantiles and neutrino energy binning. The individually optimised settings for the analysis improvement methods will be used as a starting point. One of the improvement methods (eg. neutrino energy binning) will then be varied to find new optimal setting. Afterwards, at the new optimal setting, the other improvement method (e.g. splitting the events into $E_{had.}/E_{\nu}$ quantiles) will be varied to find a new optimal setting. The process will continue until there is no significant gain in sensitivity.

We must account for limitation due to memory and time usage. Of course more $E_{had.}/E_{\nu}$ bins and finer neutrino energy binning will improve sensitivity but use judgement to strike a balance between sensitivity improvement and memory usage.

5.9 Systematic Uncertainty

Chapter 6

Results

ND, FD, Diff hadEFrac spectra (Enu, Emu, Ehad).

Contours, DelChiSqrd plots for sin and delM

6.1 Hadronic Energy Fractions In The Near Detector

Chapter 7

Conclusion

Bibliography

[1] J Chadwick. Distribution in intensity in the magnetic spectrum of the β-rays of radium. *Ver. Dtsch. Physik. Ges*, 16:383–391, 1914. 2

[2] Wolfgang Pauli. Letter to the physical society of tubingen. *Reproduced in [2]*, 1930. 2

[3] Enrico Fermi. Tentativo di una teoria dei raggi β. *Il Nuovo Cimento (1924-1942)*, 11(1):1–19, 1934. 2

[4] Frederick Reines and Clyde L. Cowan. The neutrino. *Nature*, 178:446–449, 1956. 2

[5] G. Danby et al. Observation of high-energy neutrino reactions and the existence of two kinds of neutrinos. *Phys. Rev. Lett.*, 9:36–44, Jul 1962. 2

[6] D. Decamp et al. Determination of the Number of Light Neutrino Species. *Phys. Lett.*, B231:519–529, 1989. 3

[7] S. Schael et al. Precision electroweak measurements on the Z resonance. *Phys. Rept.*, 427:257–454, 2006. 3

[8] K. Kodama et al. Observation of tau neutrino interactions. *Phys. Lett.*, B504:218–224, 2001. 3

[9] P. Anselmann et al. Solar neutrinos observed by GALLEX at Gran Sasso. *Phys. Lett.*, B285:376–389, 1992. 3

[10] Raymond Davis, Don S. Harmer, and Kenneth C. Hoffman. Search for neutrinos from the sun. *Phys. Rev. Lett.*, 20:1205–1209, May 1968. 3

[11] J.N. Bahcall, N.A. Bahcall, W.A. Fowler, and G. Shaviv. Solar neutrinos and low-energy nuclear cross sections. *Physics Letters B*, 26(6):359 – 361, 1968. 3

[12] K. S. Hirata et al. Observation of ^{8}B solar neutrinos in the kamiokande-ii detector. *Phys. Rev. Lett.*, 63:16–19, Jul 1989. 3

[13] A. I. Abazov et al. Search for neutrinos from the sun using the reaction ^{71}Ga(ν_e,e^-)^{71}ge. *Phys. Rev. Lett.*, 67:3332–3335, Dec 1991. 3

[14] B. Pontecorvo. Neutrino Experiments and the Problem of Conservation of Leptonic Charge. *Sov. Phys. JETP*, 26:984–988, 1968. [Zh. Eksp. Teor. Fiz.53,1717(1967)]. 3

[15] V. N. Gribov and B. Pontecorvo. Neutrino astronomy and lepton charge. *Phys. Lett.*, B28:493, 1969. 3

[16] Ziro Maki, Masami Nakagawa, and Shoichi Sakata. Remarks on the unified model of elementary particles. *Prog. Theor. Phys.*, 28:870–880, 1962. 3

[17] Y. Fukuda et al. Evidence for oscillation of atmospheric neutrinos. *Phys. Rev. Lett.*, 81:1562–1567, Aug 1998. 3

[18] B. Aharmim et al. Electron energy spectra, fluxes, and day-night asymmetries of ^{8}b solar neutrinos from measurements with nacl dissolved in the heavy-water detector at the sudbury neutrino observatory. *Phys. Rev. C*, 72:055502, Nov 2005. 4

[19] C. Patrignani et al. Chin. phys. c, 40, 100001. *Particle Data Group*, 2016. 4, 7, 8, 9, 10, 19

[20] R. N. Mohapatra et al. Theory of neutrinos: A White paper. *Rept. Prog. Phys.*, 70:1757–1867, 2007. 4

[21] K. Eguchi et al. First results from kamland: Evidence for reactor antineutrino disappearance. *Phys. Rev. Lett.*, 90:021802, Jan 2003. 4

[22] T. Araki et al. Measurement of neutrino oscillation with kamland: Evidence of spectral distortion. *Phys. Rev. Lett.*, 94:081801, Mar 2005. 4

[23] S. Abe et al. Precision measurement of neutrino oscillation parameters with kamland. *Phys. Rev. Lett.*, 100:221803, Jun 2008. 4

[24] B. Aharmim et al. Low-energy-threshold analysis of the phase i and phase ii data sets of the sudbury neutrino observatory. *Phys. Rev. C*, 81:055504, May 2010. 5

[25] B. Aharmim et al. Combined analysis of all three phases of solar neutrino data from the sudbury neutrino observatory. *Phys. Rev. C*, 88:025501, Aug 2013. 5

[26] J. Hosaka et al. Solar neutrino measurements in super-kamiokande-i. *Phys. Rev. D*, 73:112001, Jun 2006. 5

[27] K. Abe et al. Solar neutrino results in super-kamiokande-iii. *Phys. Rev. D*, 83:052010, Mar 2011. 5

[28] F. P. An et al. New measurement of antineutrino oscillation with the full detector configuration at daya bay. *Phys. Rev. Lett.*, 115:111802, Sep 2015. 5

[29] F. P. An et al. Observation of electron-antineutrino disappearance at Daya Bay. *Phys. Rev. Lett.*, 108:171803, 2012. 5

[30] J. H. Choi et al. Observation of Energy and Baseline Dependent Reactor Antineutrino Disappearance in the RENO Experiment. *Phys. Rev. Lett.*, 116(21):211801, 2016. 5

[31] J. K. Ahn et al. Observation of reactor electron antineutrinos disappearance in the reno experiment. *Phys. Rev. Lett.*, 108:191802, May 2012. 5

[32] Y. Abe et al. Improved measurements of the neutrino mixing angle θ_{13} with the Double Chooz detector. *JHEP*, 10:086, 2014. [Erratum: JHEP02,074(2015)]. 5

[33] D. G. Michael et al. Observation of muon neutrino disappearance with the minos detectors in the numi neutrino beam. *Phys. Rev. Lett.*, 97:191801, Nov 2006. 6

[34] P. Adamson et al. Combined analysis of ν_μ disappearance and $\nu_\mu \to \nu_e$ appearance in minos using accelerator and atmospheric neutrinos. *Phys. Rev. Lett.*, 112:191801, May 2014. 6

[35] Hiroshi Nunokawa, Stephen Parke, and Jose W. F. Valle. Cp violation and neutrino oscillations. *Prog. Part. Nucl. Phys*, 2007. 7

[36] P. Adamson et al. First measurement of electron neutrino appearance in NOvA. *Phys. Rev. Lett.*, 116(15):151806, 2016. 9

[37] D. S. Ayres et al. The NOvA Technical Design Report. *Fermilab Publication*, 2007. 11, 14, 18, 19, 23, 24

[38] NOvA authors. Nova official plots and figures. `http://www-nova.fnal.gov/plots_and_figures/plots_and_figures.html`. 13

[39] P. Adamson et al. The NuMI Neutrino Beam. *Nucl. Instrum. Meth.*, A806:279–306, 2016. 14, 15, 16, 26

[40] Stuart L. Mufson. Scintillator update. *Internal NOvA document, DocDB-8541*, 2013. 21

[41] T. T. Böhlen, F. Cerutti, M. P. W. Chin, A. Fassò, A. Ferrari, P. G. Ortega, A. Mairani, P. R. Sala, G. Smirnov, and V. Vlachoudis. The FLUKA Code: Developments and Challenges for High Energy and Medical Applications. *Nuclear Data Sheets*, 120:211–214, June 2014. 27

[42] Alfredo Ferrari, Paola R Sala, Alberto Fasso, and Johannes Ranft. Fluka: A multi-particle transport code (program version 2005), 2005. 27

[43] Sea Agostinelli, John Allison, K al Amako, J Apostolakis, H Araujo, P Arce, M Asai, D Axen, S Banerjee, G Barrand, et al. Geant4—a simulation toolkit. *Nuclear instruments and methods in physics research section A: Accelerators, Spectrometers, Detectors and Associated Equipment*, 506(3):250–303, 2003. 27

[44] Costas Andreopoulos, A Bell, D Bhattacharya, F Cavanna, J Dobson, S Dytman, H Gallagher, P Guzowski, R Hatcher, P Kehayias, et al. The genie neutrino monte carlo generator. *Nuclear Instruments and Methods in Physics Research Section A: Accelerators, Spectrometers, Detectors and Associated Equipment*, 614(1):87–104, 2010. 27, 28

[45] Chris Hagmann, David Lange, and Douglas Wright. Cosmic-ray shower generator (cry) for monte carlo transport codes. In *2007 IEEE Nuclear Science Symposium Conference Record*, volume 2, pages 1143–1146. IEEE, 2007. 27

[46] Adam Aurisano. The nova detector simulation, nova internal document, docdb 13577, June 2015. 29, 52

[47] A Aurisano et al. Chep2015 proceeding: The nova simulation chain, a. aurisano, nova internal document, docdb 13370, May 2015. 29

[48] Jeff Hartnell and Greg Pawloski. Summary of the 2016 (second analysis) ν_μ disappearance analysis. NOvA Internal Document, DocDB-15232, May 2016. 30, 33, 51, 52

[49] NOvA authors. Place holder for sa nova numu paper. arXiv:1701.05891. 30, 38, 56, 57

[50] Michael David Baird. An analysis of muon neutrino disappearance from the numi beam using an optimal track fitter, 2015. 30

[51] Martin Ester, Hans-Peter Kriegel, Jörg Sander, Xiaowei Xu, et al. A density-based algorithm for discovering clusters in large spatial databases with noise. In *Kdd*, volume 96, pages 226–231, 1996. 30

[52] Rudolph Emil Kalman et al. A new approach to linear filtering and prediction problems. *Journal of basic Engineering*, 82(1):35–45, 1960. 30

[53] Nicholas Raddatz. Kalmantrack technical note. NOvA Internal Document, DocDB-13545. 30, 31

[54] Louise Suter and James Musser. Sa data quality updates. NOvA Internal Document, DocDB-15307, April 2016. 32

[55] Sarah R Phan-Budd and Lisa Goodenough. Technical note on the nova beam monitoring for 2015 summer analysis. NOvA Internal Document, DocDB-13572, July 2015. 32

[56] NOvA authors. Nova numu blessed plots. `http://nusoft.fnal.gov/nova/blessedplots/Numu_SA.html`, February 2017. 32

[57] Susan Lein. Dcm edge metric. NOvA Internal Document, DocDB-13527, June 2015. 33

[58] Kirk Bays. Nova cosmic rejection package and algorithms technical note. NOvA Internal Document, DocDB-11205. 33

[59] Naomi S Altman. An introduction to kernel and nearest-neighbor nonparametric regression. *The American Statistician*, 46(3):175–185, 1992. 33

[60] Nick Raddatz. *Measurement of Muon Neutrino Disappearance with Non-Fiducial Interactions in the NOvA Experiment*. PhD thesis, University of Minnesota, 2016. 33, 34

[61] Nicholas Raddatz. Remid technical note. NOvA Internal Document, DocDB-11206. 34

[62] A Aurisano, A Radovic, D Rocco, A Himmel, MD Messier, E Niner, G Pawloski, F Psihas, A Sousa, and P Vahle. A convolutional neural network neutrino event classifier. *Journal of Instrumentation*, 11(09):P09001, 2016. 34, 35

[63] Christopher Backhouse and Alexander Radovic. The attenuation and threhold correction of the nova detectors. NOvA Internal Document, DocDB-13579, 2015. 35, 36

[64] Christopher Backhouse, Alexander Radovic, and Prabhjot Singh. The attenuation and threhold correction of the nova detectors. NOvA Internal Document, DocDB-13579, 2016. 36

[65] Luke Vinton. Calorimetric energy scale calibration of the nova detectors. NOvA Internal Document, DocDB-13579, 2015. 36, 37

[66] Diana Patricia Mendez. Second analysis calorimetric energy scale calibration of the nova detectors. NOvA Internal Document, DocDB-13579, 2016. 36, 44

[67] Evan Niner. Timing calibration technical note. NOvA Internal Document, DocDB-13579, 2015. 37

[68] PA Rodrigues, J Demgen, E Miltenberger, L Aliaga, O Altinok, L Bellantoni, A Bercellie, M Betancourt, A Bodek, A Bravar, et al. Identification of nuclear effects in neutrino-carbon interactions at low three-momentum transfer. *Physical review letters*, 116(7):071802, 2016. 39

[69] Jeremy Wolcott. Genie tune and uncertainty band for second analysis. NOvA Internal Document, DocDB-15214, 2016. 39, 40

[70] Omar Benhar, Donal Day, and Ingo Sick. Inclusive quasielastic electron-nucleus scattering. *Reviews of Modern Physics*, 80(1):189, 2008. 39

[71] V Lyubushkin, B Popov, JJ Kim, L Camilleri, J-M Levy, M Mezzetto, D Naumov, S Alekhin, P Astier, D Autiero, et al. A study of quasi-elastic muon neutrino and antineutrino scattering in the nomad experiment. *The European Physical Journal C-Particles and Fields*, 63(3):355–381, 2009. 39

[72] Teppei Katori. *A Measurement of the muon neutrino charged current quasielastic interaction and a test of Lorentz violation with the MiniBooNE experiment.* PhD thesis, Indiana U., 2008. 40

[73] Vladimir Bychkov. Technote for genie systematics. NOvA Internal Document, DocDB-15234, 2016. 44

[74] Zamorano. Intensity-related systematic uncertainty for the second analysis. NOvA Internal Document, DocDB-15217, 2016. 44

[75] Susan Lein. Summary of de/dx plots for muons/protons. NOvA Internal Document, DocDB-15028, 2016. 44

[76] Luke Vinton. Tech note on the calibration systematics for the muon neutrino disappearance analysis. NOvA Internal Document, DocDB-15215, 2016. 45

[77] CN Chou. The nature of the saturation effect of fluorescent scintillators. *Physical Review*, 87(5):904, 1952. 50

[78] Daniel Pershey. Birks-chou post tuning. NOvA Internal Document, DocDB-13233, 2015. 50

[79] Luke Vinton. Birks' systematic uncertainties for the second muon neutrino disappearance analysis. NOvA Internal Document, DocDB-15347, 2016. 50

[80] Luke Vinton. Nd normalisation with rock muons. NOvA Internal Document, DocDB-15292, 2016. 50

[81] Luke Vinton. Noise systematics for the second muon neutrino disappearance analysis. NOvA Internal Document, DocDB-15216, 2016. 52

[82] Christopher Backhouse. The cafana framework - technote. NOvA Internal Document, DocDB-9222, 2014. 55

[83] P Adamson, I Anghel, A Aurisano, G Barr, M Bishai, A Blake, GJ Bock, D Bogert, SV Cao, CM Castromonte, et al. Combined analysis of ν_μ disappearance and $\nu_\mu \rightarrow \nu_e$ appearance in minos using accelerator and atmospheric neutrinos. *Physical review letters*, 112(19):191801, 2014. 56

[84] Kou Abe, J Adam, H Aihara, T Akiri, C Andreopoulos, S Aoki, A Ariga, S Assylbekov, D Autiero, M Barbi, et al. Measurements of neutrino oscillation in appearance and disappearance channels by the t2k experiment with 6.6× 1 0 20 protons on target. *Physical Review D*, 91(7):072010, 2015. 56

[85] Kirk Bays. Numu sa fc nh result. NOvA Internal Document, DocDB-15814, 2016. 58

[86] Luke Vinton. Effect of systematics on hadefrac bin values. NOvA Internal Document, DocDB-17854, 2017. 59

[87] John Stuart Marshall. *A study of muon neutrino disappearance with the MINOS detectors and the NuMI neutrino beam.* PhD thesis, Cambridge U., 2008. 59

[88] Luke Vinton. Sensitivity studies. hybrid selection and number of neutrino energy bins. NOvA Internal Document, DocDB-16292, 2016. 69